



UNIVERSIDADE ESTADUAL DE CAMPINAS
SISTEMA DE BIBLIOTECAS DA UNICAMP
REPOSITÓRIO DA PRODUÇÃO CIENTÍFICA E INTELLECTUAL DA UNICAMP

Versão do arquivo anexado / Version of attached file:

Versão do Editor / Published Version

Mais informações no site da editora / Further information on publisher's website:

<https://link.springer.com/article/10.1007%2FJHEP05%282014%29104>

DOI: 10.1007/JHEP05(2014)104

Direitos autorais / Publisher's copyright statement:

©2014 by Societa Italiana di Fisica. All rights reserved.

DIRETORIA DE TRATAMENTO DA INFORMAÇÃO

Cidade Universitária Zeferino Vaz Barão Geraldo

CEP 13083-970 – Campinas SP

Fone: (19) 3521-6493

<http://www.repositorio.unicamp.br>

RECEIVED: January 20, 2014

REVISED: April 13, 2014

ACCEPTED: April 13, 2014

PUBLISHED: May 22, 2014

Evidence for the 125 GeV Higgs boson decaying to a pair of τ leptons



The CMS collaboration

E-mail: cms-publication-committee-chair@cern.ch

ABSTRACT: A search for a standard model Higgs boson decaying into a pair of τ leptons is performed using events recorded by the CMS experiment at the LHC in 2011 and 2012. The dataset corresponds to an integrated luminosity of 4.9 fb^{-1} at a centre-of-mass energy of 7 TeV and 19.7 fb^{-1} at 8 TeV. Each τ lepton decays hadronically or leptonically to an electron or a muon, leading to six different final states for the τ -lepton pair, all considered in this analysis. An excess of events is observed over the expected background contributions, with a local significance larger than 3 standard deviations for m_H values between 115 and 130 GeV. The best fit of the observed $H \rightarrow \tau\tau$ signal cross section times branching fraction for $m_H = 125 \text{ GeV}$ is 0.78 ± 0.27 times the standard model expectation. These observations constitute evidence for the 125 GeV Higgs boson decaying to a pair of τ leptons.

KEYWORDS: Hadron-Hadron Scattering, Higgs physics

ARXIV EPRINT: [1401.5041](https://arxiv.org/abs/1401.5041)

Contents

1	Introduction	1
2	Analysis overview	2
3	The CMS experiment	4
4	Baseline event selection	7
5	The tau-pair invariant-mass reconstruction	9
6	Event categories	11
7	Background estimation	15
8	Systematic uncertainties	19
9	Results	21
10	Summary	33
A	Post-fit distributions	35
B	Event yields	46
	The CMS collaboration	54

1 Introduction

Elucidating the mechanism of electroweak symmetry breaking, through which the W and Z bosons become massive, is an important goal of the Large Hadron Collider (LHC) physics programme. In the standard model (SM) [1, 2], electroweak symmetry breaking is achieved via the Brout-Englert-Higgs mechanism [3–8], which also predicts the existence of a scalar Higgs boson. On July 4, 2012, the discovery of a new boson with a mass around 125 GeV was announced at CERN by the ATLAS and CMS Collaborations [9–11]. The excess was most significant in the ZZ, $\gamma\gamma$, and WW decay modes. The spin and CP properties of the new boson are compatible with those of the SM Higgs boson [12, 13]. In the SM, the masses of the fermions are generated via the Yukawa couplings between the Higgs field and the fermionic fields. The measurement of these couplings is essential for identifying this boson as the SM Higgs boson. The $\tau\tau$ decay mode is the most promising because of the large event rate expected in the SM compared to the other leptonic decay modes and the smaller contribution from background events with respect to the $b\bar{b}$ decay mode.

Searches for SM Higgs bosons decaying to a τ -lepton pair have been performed at the LEP, Tevatron, and LHC colliders. The collaborations at LEP have searched for associated ZH production and found no significant excess of events over the background expectation [14–17]. Dedicated searches in the $\tau\tau$ final state have been carried out at the Tevatron and at the LHC, placing upper limits on the Higgs boson production cross section times branching fraction, denoted as $\sigma \times B$, at the 95% confidence level (CL). Using $p\bar{p}$ collisions at $\sqrt{s} = 1.96$ TeV, the CDF Collaboration excluded values larger than 16 times $(\sigma \times B)_{\text{SM}}^{125 \text{ GeV}}$ [18], with $(\sigma \times B)_{\text{SM}}^{125 \text{ GeV}}$ denoting the SM prediction for $\sigma \times B$ with $m_{\text{H}} = 125$ GeV, and the D0 Collaboration excluded values larger than 14 times $(\sigma \times B)_{\text{SM}}^{125 \text{ GeV}}$ [19]. With pp collisions at $\sqrt{s} = 7$ TeV, the ATLAS Collaboration found an observed (expected) upper limit of 3.7 (3.5) times $(\sigma \times B)_{\text{SM}}^{125 \text{ GeV}}$ [20], whereas the CMS Collaboration placed an observed (expected) upper limit of 4.2 (3.1) times $(\sigma \times B)_{\text{SM}}^{125 \text{ GeV}}$ [21].

This paper reports on the results of a search for a SM Higgs boson using final states with a pair of τ leptons in proton-proton collisions at $\sqrt{s} = 7$ and 8 TeV at the LHC. We use the entire dataset collected in 2011 and 2012 by the CMS experiment corresponding to an integrated luminosity of 4.9 fb^{-1} at a centre-of-mass energy of 7 TeV and 19.7 fb^{-1} at 8 TeV.

The paper is organized as follows. An overview of the analysis strategy is given in section 2, while the CMS detector, the event reconstruction, and the Monte Carlo (MC) simulation are described in section 3. The event selection is summarized in section 4, followed by the description of the reconstruction of the τ -lepton pair invariant mass in section 5 and the categorization of events in section 6. The background estimation is based on data control regions whenever possible and is explained in section 7. Finally, systematic uncertainties are summarized in section 8 and the results are presented in section 9.

2 Analysis overview

Throughout this paper, the symbol τ_{h} denotes the reconstructed hadronic decay of a τ lepton. The τ_{h} candidates are reconstructed in decay modes with one or three charged particles (see section 3). The symbol ℓ refers to an electron or a muon, and the symbol L to any kind of reconstructed charged lepton, namely electron, muon, or τ_{h} .

The main Higgs boson production mechanisms, shown in figure 1, lead to final states with a different number of charged leptons. For Higgs boson production through gluon-gluon fusion and vector boson fusion (VBF), final states with $\text{H} \rightarrow \tau\tau$ decays contain only two charged leptons, defining the LL' channels. All six τ -pair final states are studied: $LL' = \mu\tau_{\text{h}}, e\tau_{\text{h}}, \tau_{\text{h}}\tau_{\text{h}}, e\mu, \mu\mu,$ and ee .

Sensitivity to the associated production with a W or a Z boson is achieved by requiring one or two additional electrons or muons compatible with leptonic decays of the W or Z boson. The four most sensitive final states are retained in the $\ell + L\tau_{\text{h}}$ channels aiming at the associated production with a W boson, $\ell + L\tau_{\text{h}} = \mu + \mu\tau_{\text{h}}, e + \mu\tau_{\text{h}}/\mu + e\tau_{\text{h}}, \mu + \tau_{\text{h}}\tau_{\text{h}},$ and $e + \tau_{\text{h}}\tau_{\text{h}}$. In the $\ell\ell + LL'$ channels that target the associated production with a Z boson decaying to $\ell\ell$, the τ -pair final states $\mu\tau_{\text{h}}, e\tau_{\text{h}}, e\mu,$ and $\tau_{\text{h}}\tau_{\text{h}}$ are considered, leading to eight

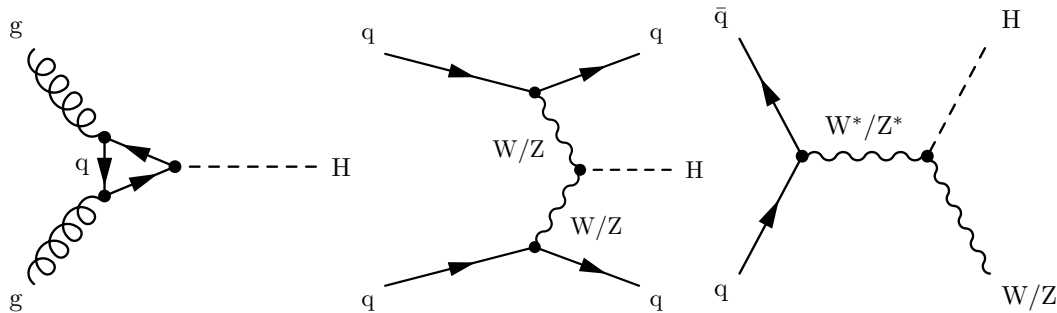


Figure 1. Leading-order Feynman diagrams for Higgs boson production through gluon-gluon fusion (left), vector boson fusion (middle), and the associated production with a W or a Z boson (right).

channels in total. The ee and $\mu\mu$ τ -pair final states are excluded because the corresponding events are already used in the search for $H \rightarrow ZZ \rightarrow 4\ell$ [11].

To maximize the sensitivity of the analysis in the LL' channels, events are classified in categories according to the number of jets in the final state, excluding the jets corresponding to the L and L' leptons. The events are further classified according to a number of kinematic quantities that exhibit different distributions for signal and background events (see section 6). In particular, the contribution of the VBF production process is enhanced for events with two or more jets by requiring a large rapidity gap between the two jets with the highest transverse momentum. For the remaining events with at least one jet, requiring a large p_T of the reconstructed Higgs boson candidate increases the sensitivity to Higgs boson production through gluon fusion. A complete listing of all lepton final states and event categories is given in appendix B.

With the exception of the $\ell + L\tau_h$, ee , and $\mu\mu$ channels, the signal is extracted from the distribution of the invariant mass of the τ -lepton pair, $m_{\tau\tau}$, calculated from the L and L' four-momenta and the missing transverse energy vector. In the $\ell + L\tau_h$ channels, the signal extraction is instead based on the invariant mass, m_{vis} , of the visible $L\tau_h$ decay products because the missing transverse energy does not entirely arise from the neutrinos produced in the decay of the two τ leptons. In the ee and $\mu\mu$ channels, a discriminating variable combining a number of kinematic quantities and other observables, including $m_{\tau\tau}$, is used.

The background composition depends on the channel and, in particular, on the number of electrons and muons in the final state. The Drell-Yan production of a Z boson decaying into a pair of τ leptons constitutes the main irreducible background in all LL' channels. Another source of background with the same leptonic final state is the production of top-quark pairs ($t\bar{t}$), which is most important in the $e\mu$ channel. Reducible background contributions include QCD multijet production that is particularly relevant in the $\tau_h\tau_h$ channel and $W(\rightarrow \ell\nu) + \text{jets}$ production with a jet misidentified as a τ_h in the $\ell\tau_h$ channels. In the $\ell + L\tau_h$ and $\ell\ell + LL'$ channels, diboson production is the largest irreducible background.

While the signal contribution is expected to be a pure sample of $H \rightarrow \tau\tau$ decays in many channels considered, there is a significant contribution from $H \rightarrow WW$ decays in the $\ell + \ell'\tau_h$ and the $\ell\ell + LL'$ channels, and, most importantly, in the two-jet event samples of the $e\mu$,

ee , and $\mu\mu$ channels. The contribution from $H \rightarrow WW$ decays is treated as a background in the search for $H \rightarrow \tau\tau$ decays. Given the discovery of a SM-like Higgs boson with the mass near 125 GeV, this contribution is taken from the expectation for a SM Higgs boson with $m_H = 125$ GeV. On the other hand, the presence of a $H \rightarrow WW$ contribution provides additional sensitivity to the coupling of the Higgs boson to vector bosons. Therefore, the $H \rightarrow WW$ contribution is treated as a signal process for the measurement of the fermionic and the bosonic couplings of the Higgs boson.

3 The CMS experiment

The central feature of the CMS apparatus is a superconducting solenoid of 6 m internal diameter, providing a magnetic field of 3.8 T. Within the volume of the superconducting solenoid are a silicon pixel and strip tracker, a lead tungstate crystal electromagnetic calorimeter, and a brass/scintillator hadron calorimeter. The coverage of these calorimeters is complemented by extensive forward calorimetry. Muons are detected in gas-ionization chambers embedded in the steel flux return yoke outside the solenoid. The first level of the CMS trigger system (L1), composed of custom hardware processors, uses information from the calorimeters and muon detectors to select the most interesting events in a fixed time interval of less than 4 μ s. The high-level trigger (HLT) processor farm further decreases the event rate from around 100 kHz to around 300 Hz, before data storage. A more detailed description of the CMS detector can be found in ref. [22].

The CMS experiment uses a right-handed coordinate system, with the origin at the nominal interaction point, the x axis pointing to the centre of the LHC, the y axis pointing up (perpendicular to the LHC plane), and the z axis along the anticlockwise-beam direction. The polar angle θ is measured from the positive z axis and the azimuthal angle ϕ is measured in the transverse (x, y) plane. The pseudorapidity is defined as $\eta \equiv -\ln[\tan(\theta/2)]$.

The number of inelastic proton-proton collisions occurring per LHC bunch crossing was, on average, 9 in 2011 and 21 in 2012. The tracking system is able to separate collision vertices as close as 0.5 mm along the beam direction [23]. For each vertex, the sum of the squared transverse momenta of all associated tracks is computed. The vertex for which this quantity is the largest is assumed to correspond to the hard-scattering process and is referred to as the primary vertex. The additional proton-proton collisions happening in the same bunch crossing are termed pileup (PU).

A particle-flow (PF) algorithm [24–26] combines the information from the CMS sub-detectors to identify and reconstruct the particles emerging from proton-proton collisions: charged hadrons, neutral hadrons, photons, muons, and electrons. These particles are then used to reconstruct the missing transverse energy vector \vec{E}_T^{miss} , the jets, the τ_h candidates, and to quantify the lepton isolation. Jets are reconstructed from all particles using the anti- k_T jet clustering algorithm implemented in FASTJET [27, 28], with a distance parameter of 0.5. The jet energy scale is calibrated through correction factors that depend on the p_T and η of the jet [29]. Jets originating from the hadronization of b quarks are identified using the combined secondary vertex (CSV) algorithm [30] which exploits observables related to the long lifetime of b hadrons. The b-tagging efficiencies in simulation are corrected for

differences between simulated and recorded events. Jets originating from PU are identified and rejected based on both vertex information and jet shape information [31]. All particles reconstructed in the event are used to determine the \vec{E}_T^{miss} (and its magnitude, E_T^{miss}) with a high, PU-independent, resolution [32] using a multivariate regression technique based on a boosted decision tree (BDT) [33].

Muons are identified with additional requirements on the quality of the track reconstruction and on the number of measurements in the tracker and the muon systems [34]. Electrons are identified with a multivariate discriminant combining several quantities describing the track quality, the shape of the energy deposits in the electromagnetic calorimeter, and the compatibility of the measurements from the tracker and the electromagnetic calorimeter [35]. The τ_h are reconstructed and identified using the “hadron-plus-strips” algorithm [36] which uses charged hadrons and photons to reconstruct the main decay modes of the τ lepton: one charged hadron, one charged hadron + photons, and three charged hadrons. Electrons and muons misidentified as τ_h are suppressed using dedicated criteria based on the consistency between the measurements in the tracker, the calorimeters, and the muon detectors. Figure 2 shows the resulting τ_h mass distribution reconstructed from the visible decay products, $m_{\text{vis}}^{\tau_h}$, in the $\mu\tau_h$ channel after the baseline selection described in section 4, illustrating the different decay modes.

To reject non-prompt or misidentified leptons, the absolute lepton isolation is defined as

$$I^L \equiv \sum_{\text{charged}} p_T + \max \left(0, \sum_{\text{neutral}} p_T + \sum_{\gamma} p_T - \frac{1}{2} \sum_{\text{charged, PU}} p_T \right). \quad (3.1)$$

In this expression, $\sum_{\text{charged}} p_T$ is the scalar sum of the transverse momenta of the charged hadrons, electrons, and muons originating from the primary vertex and located in a cone of size $\Delta R = \sqrt{(\Delta\eta)^2 + (\Delta\phi)^2} = 0.4$ centred on the lepton direction. The sums $\sum_{\text{neutral}} p_T$ and $\sum_{\gamma} p_T$ represent the same quantity for neutral hadrons and photons, respectively. In the case of τ_h , the particles used in the reconstruction of the τ_h are excluded from the sums. The contribution of pileup photons and neutral hadrons is estimated from the scalar sum of the transverse momenta of charged hadrons from pileup vertices in the cone, $\sum_{\text{charged, PU}} p_T$. This sum is multiplied by a factor of 1/2 which corresponds approximately to the ratio of neutral to charged hadron production in the hadronization process of inelastic proton-proton collisions, as estimated from simulation. The relative lepton isolation is defined as $R^L \equiv I^L/p_T^L$, where p_T^L is the lepton transverse momentum.

The signal event samples with a SM Higgs boson produced through gluon-gluon fusion or VBF are generated with POWHEG 1.0 [37–41], while PYTHIA 6.4 [42] is used for the production of a SM Higgs boson in association with a W or Z boson, or with a $t\bar{t}$ pair. The MADGRAPH 5.1 [43] generator is used for Z + jets, W + jets, $t\bar{t}$ + jets, and diboson production, and POWHEG for single-top-quark production. The POWHEG and MADGRAPH generators are interfaced with PYTHIA for parton shower and fragmentation. The PYTHIA parameters affecting the description of the underlying event are set to the Z2 tune for the 7 TeV samples and to the Z2* tune for the 8 TeV samples [44]. All generators are interfaced with TAUOLA [45] for the simulation of the τ -lepton decays. The Higgs boson p_T spectrum

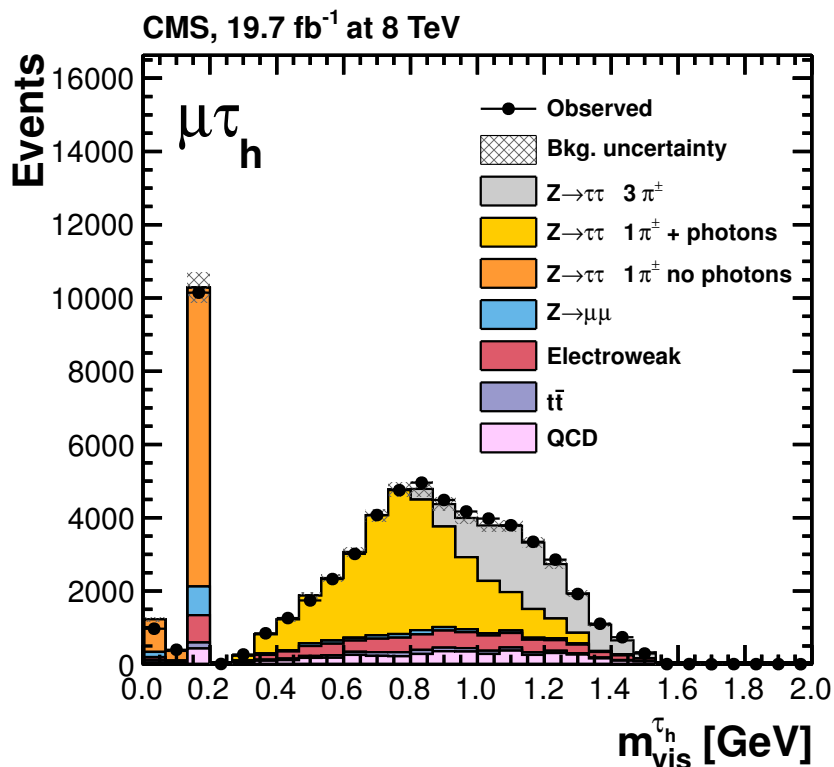


Figure 2. Observed and predicted distributions for the visible τ_h mass, $m_{\text{vis}}^{\tau_h}$, in the $\mu\tau_h$ channel after the baseline selection described in section 4. The yields predicted for the $Z \rightarrow \tau\tau$, $Z \rightarrow \mu\mu$, electroweak, $t\bar{t}$, and QCD multijet background contributions correspond to the result of the final fit presented in section 9. The $Z \rightarrow \tau\tau$ contribution is then split according to the decay mode reconstructed by the hadron-plus-strips algorithm as shown in the legend. The mass distribution of the τ_h built from one charged hadron and photons peaks near the mass of the intermediate $\rho(770)$ resonance; the mass distribution of the τ_h built from three charged hadrons peaks around the mass of the intermediate $a_1(1260)$ resonance. The τ_h built from one charged hadron and no photons are reconstructed with the π^\pm mass, assigned to all charged hadrons by the PF algorithm, and constitute the main contribution to the third bin of this histogram. The first two bins correspond to τ^\pm leptons decaying into $e^\pm\nu\nu$ and $\mu^\pm\nu\nu$, respectively, and for which the electron or muon is misidentified as a τ_h . The electroweak background contribution is dominated by W +jets production. In most selected W + jets, $t\bar{t}$, and QCD multijet events, a jet is misidentified as a τ_h . The “bkg. uncertainty” band represents the combined statistical and systematic uncertainty in the background yield in each bin. The expected contribution from the SM Higgs signal is negligible.

from POWHEG is reweighted to the spectrum obtained from a next-to-next-to-leading-order (NNLO) calculation using HRES [46]. The reweighting increases by about 3% the fraction of gluon-gluon fusion signal events with a Higgs boson mass of 125 GeV and $p_T > 100$ GeV. The various production cross sections and branching fractions for SM processes and their corresponding uncertainties are taken from references [47–73].

The presence of pileup interactions is incorporated by simulating additional proton-proton collisions with PYTHIA. All generated events are processed through a detailed simulation of the CMS detector based on GEANT4 [74] and are reconstructed with the same

algorithms as for data. Simulated and recorded $Z + \text{jets}$ events are compared to extract event weighting factors and energy correction factors for the various physics objects. These are then applied to all simulated events in order to minimize the remaining discrepancies with data. In particular, (i) a recoil correction is applied to the response and resolution of the components of the \vec{E}_T^{miss} [32], (ii) energy correction factors are applied to the leptons, and (iii) simulated events are weighted by the ratio between the observed and expected lepton selection efficiencies, which can differ by a few percent.

4 Baseline event selection

Events are selected and classified in the various channels according to the number of selected electrons, muons, and τ_h candidates. The resulting event samples are independent. Using simulated event samples, the trigger and offline selection criteria have been optimized for each channel to maximize the sensitivity to a SM Higgs boson signal. These criteria are summarized in table 1 for the LL' and $\ell + L\tau_h$ channels, and in table 2 for the $\ell\ell + LL'$ channels.

The HLT requires a combination of electron, muon, and τ_h trigger objects [34, 35, 75]. A specific version of the PF algorithm is used in the HLT to quantify the isolation of τ_h trigger objects as done in the offline reconstruction. Channels with two ℓ are based on a di- ℓ trigger. Channels with a single ℓ are based on a $\ell\tau_h$ trigger except for the $\mu + \tau_h\tau_h$ channel which uses a single-muon trigger. The fully hadronic $\tau_h\tau_h$ channel relies on di- τ_h and di- $\tau_h + \text{jet}$ triggers, implemented for the 8 TeV data taking period. For these triggers, the reconstruction of the two τ_h trigger objects is seeded by objects from the L1 trigger system. These objects can either be two calorimeter jets with $p_T > 64 \text{ GeV}$ and $|\eta| < 3.0$ or two narrow calorimeter jets with $p_T > 44 \text{ GeV}$ and $|\eta| < 2.17$. The offline isolation requirements range within the values given in table 1 depending on the lepton flavour, p_T , and η . For the channels considered in this analysis, the efficiency to reconstruct and select offline a τ decaying hadronically ranges from 60 to 70%, with a jet misidentification probability around 1%. For τ_h candidates selected offline, the efficiency of the HLT selection plateaus at 90%. For the $\mu\tau_h$ channel, the muon p_T threshold was raised in 2012 to 20 GeV to cope with the increased instantaneous luminosity. For the same reason, the electron p_T threshold was raised to 24 GeV in the $e\tau_h$ channel. For the $\ell\ell + LL'$ channels, the selection proceeds by first identifying a Z boson candidate ($Z \rightarrow \ell\ell$) with mass between 60 and 120 GeV from opposite-charge electron or muon pairs, and then a Higgs boson candidate ($H \rightarrow LL'$) from the remaining leptons. With some variations among the channels, all leptons meet the minimum requirement that the distance of closest approach to the primary vertex satisfies $d_z < 0.2 \text{ cm}$ along the beam direction, and $d_{xy} < 0.045 \text{ cm}$ in the transverse plane. The two leptons assigned to the Higgs boson decay are required to be of opposite charge.

In the $\ell\tau_h$ channels, the large $W + \text{jets}$ background is reduced by requiring

$$m_T \equiv \sqrt{2p_T^\ell E_T^{\text{miss}}(1 - \cos(\Delta\phi))} < 30 \text{ GeV}, \tag{4.1}$$

where p_T^ℓ is the ℓ transverse momentum and $\Delta\phi$ is the difference in azimuthal angle between the ℓ direction and the \vec{E}_T^{miss} . In the $e\mu$ channel, the $t\bar{t}$ background is reduced using a BDT

Channel	HLT requirement	Lepton selection		
$\mu\tau_h$	$\mu(12-18) \& \tau_h(10-20)$	$p_T^\mu > 17-20$ $p_T^{\tau_h} > 30$	$ \eta^\mu < 2.1$ $ \eta^{\tau_h} < 2.4$	$R^\mu < 0.1$ $I^{\tau_h} < 1.5$
$e\tau_h$	$e(15-22) \& \tau_h(15-20)$	$p_T^e > 20-24$ $p_T^{\tau_h} > 30$	$ \eta^e < 2.1$ $ \eta^{\tau_h} < 2.4$	$R^e < 0.1$ $I^{\tau_h} < 1.5$
$\tau_h\tau_h$ (2012 only)	$\tau_h(35) \& \tau_h(35)$ $\tau_h(30) \& \tau_h(30) \& \text{jet}(30)$	$p_T^{\tau_h} > 45$	$ \eta^{\tau_h} < 2.1$	$I^{\tau_h} < 1$
$e\mu$	$e(17) \& \mu(8)$ $e(8) \& \mu(17)$	$p_T^{\ell_1} > 20$ $p_T^{\ell_2} > 10$	$ \eta^\mu < 2.1$ $ \eta^e < 2.3$	$R^\ell < 0.1-0.15$
$\mu\mu$	$\mu(17) \& \mu(8)$	$p_T^{\mu_1} > 20$ $p_T^{\mu_2} > 10$	$ \eta^{\mu_1} < 2.1$ $ \eta^{\mu_2} < 2.4$	$R^\mu < 0.1$
ee	$e(17) \& e(8)$	$p_T^{e_1} > 20$ $p_T^{e_2} > 10$	$ \eta^e < 2.3$	$R^e < 0.1-0.15$
$\mu + \mu\tau_h$	$\mu(17) \& \mu(8)$	$p_T^{\mu_1} > 20$ $p_T^{\mu_2} > 10$ $p_T^{\tau_h} > 20$	$ \eta^\mu < 2.4$ $ \eta^{\tau_h} < 2.3$	$R^\mu < 0.1-0.2$ $I^{\tau_h} < 2$
$e + \mu\tau_h /$ $\mu + e\tau_h$	$e(17) \& \mu(8)$ $e(8) \& \mu(17)$	$p_T^{\ell_1} > 20$ $p_T^{\ell_2} > 10$ $p_T^{\tau_h} > 20$	$ \eta^e < 2.5$ $ \eta^\mu < 2.4$ $ \eta^{\tau_h} < 2.3$	$R^\ell < 0.1-0.2$ $I^{\tau_h} < 2$
$\mu + \tau_h\tau_h$	$\mu(24)$	$p_T^\mu > 24$ $p_T^{\tau_{h,1}} > 25$ $p_T^{\tau_{h,2}} > 20$	$ \eta^\mu < 2.1$ $ \eta^{\tau_h} < 2.3$	$R^\mu < 0.1$ $I^{\tau_h} < 2-3$
$e + \tau_h\tau_h$	$e(20) \& \tau_h(20)$ $e(22) \& \tau_h(20)$	$p_T^e > 24$ $p_T^{\tau_{h,1}} > 25$ $p_T^{\tau_{h,2}} > 20$	$ \eta^e < 2.1$ $ \eta^{\tau_h} < 2.3$	$R^e < 0.1-0.15$ $I^{\tau_h} < 2$

Table 1. Lepton selection for the LL' and $\ell + L\tau_h$ channels. The HLT requirement is defined by a combination of trigger objects with p_T over a given threshold. The p_T and I^{τ_h} thresholds are given in GeV. The indices 1 and 2 denote, respectively, the leptons with the highest and next-to-highest p_T . The definitions of the lepton isolation, R and I , are given in the text. For a number of channels, the isolation requirements depend on the lepton flavour, p_T , and η . Similarly, a range of p_T thresholds is given when the HLT requirements change with the data-taking period.

discriminant that makes use of kinematic variables related to the $e\mu$ system and the \vec{E}_T^{miss} , the distance of closest approach between the leptons and the primary vertex, and the value of the CSV b-tagging discriminator for the leading jet with $p_T > 20$ GeV, if any.

In the $\ell + \tau_h\tau_h$ channels, the background from QCD multijet, $W + \text{jets}$, and $Z + \text{jets}$ production is suppressed using a BDT discriminant based on the E_T^{miss} and on kinematic

Resonance	HLT requirement	Lepton selection
$Z \rightarrow \mu\mu$	$\mu(17) \& \mu(8)$	$p_T^{\mu 1} > 20$ $ \eta^\mu < 2.4$ $R^\mu < 0.3$ $p_T^{\mu 2} > 10$
$Z \rightarrow ee$	$e(17) \& e(8)$	$p_T^{e 1} > 20$ $ \eta^e < 2.5$ $R^e < 0.3$ $p_T^{e 2} > 10$
$H \rightarrow \mu\tau_h$		$p_T^\mu > 10$ $ \eta^\mu < 2.4$ $R^\mu < 0.3$ $p_T^{\tau_h} > 15$ $ \eta^{\tau_h} < 2.3$ $I^{\tau_h} < 2$
$H \rightarrow e\tau_h$		$p_T^e > 10$ $ \eta^e < 2.5$ $R^e < 0.2$ $p_T^{\tau_h} > 15$ $ \eta^{\tau_h} < 2.3$ $I^{\tau_h} < 2$
$H \rightarrow \tau_h\tau_h$		$p_T^{\tau_h} > 15$ $ \eta^{\tau_h} < 2.3$ $I^{\tau_h} < 1$
$H \rightarrow e\mu$		$p_T^\ell > 10$ $ \eta^e < 2.5$ $R^\ell < 0.3$ $ \eta^\mu < 2.4$

Table 2. Lepton selection for the $\ell\ell + LL'$ channels. The HLT requirement is defined by a combination of trigger objects over a p_T threshold indicated in GeV. The p_T and I^{τ_h} thresholds are given in GeV. The indices 1 and 2 denote, respectively, the leptons with the highest and next-to-highest p_T .

variables related to the $\tau_h\tau_h$ system. With $\tau_{h,1}$ and $\tau_{h,2}$ denoting the τ_h with highest and second-highest p_T , respectively, these variables are $p_T^{\tau_{h,1}}$, $p_T^{\tau_{h,2}}$, $\Delta R(\tau_{h,1}, \tau_{h,2})$, and $p_T^{\tau_{h,1}, \tau_{h,2}} / (p_T^{\tau_{h,1}} + p_T^{\tau_{h,2}})$. For the chosen threshold on the BDT score, the signal efficiency is $\sim 60\%$ whereas the efficiency for the reducible background components is $\sim 13\%$.

In the $\ell + \ell'\tau_h$ channels, the large background from Z and $t\bar{t}$ production is strongly reduced by requiring the ℓ and ℓ' leptons to have the same charge. For the 7 TeV dataset, the requirement $L_T \equiv p_T^\ell + p_T^{\ell'} + p_T^{\tau_h} > 80$ GeV is imposed to further suppress the reducible background components. For the 8 TeV dataset, the L_T variable is instead used to divide the data into two event categories, one with high L_T (≥ 130 GeV) and one with low L_T (< 130 GeV). The $Z + \text{jets}$ background in the $\ell\ell + LL'$ channels is reduced by selecting events with high $L_T^{LL'} \equiv p_T^L + p_T^{L'}$. The requirements are $L_T^{\mu\tau_h} > 45$ GeV for $\ell\ell + \mu\tau_h$, $L_T^{e\tau_h} > 30$ GeV for $\ell\ell + e\tau_h$, $L_T^{\tau_h\tau_h} > 70$ GeV for $\ell\ell + \tau_h\tau_h$, and $L_T^{e\mu} > 25$ GeV for $\ell\ell + e\mu$.

5 The τ -pair invariant-mass reconstruction

The visible mass, m_{vis} , of the LL' system could be used to separate the $H \rightarrow \tau\tau$ signal events from the $Z \rightarrow \tau\tau$ events, which constitute an important irreducible background. However, the neutrinos from the τ -lepton decay can take away a large amount of energy, thereby limiting the separation power of the m_{vis} variable. In $Z \rightarrow \tau\tau$ events and in $H \rightarrow \tau\tau$ events where the Higgs boson is produced through gluon-gluon fusion, VBF, or in association with a Z boson, the τ -lepton decay is the only source of neutrinos. The SVFIT

algorithm described below combines the E_T^{miss} with the L and L' momenta to calculate a more precise estimator of the mass of the parent boson, the τ -pair invariant mass $m_{\tau\tau}$.

Six parameters are needed to specify a hadronic τ -lepton decay: the polar and azimuthal angles of the visible decay product system in the τ -lepton rest frame, the three boost parameters from the τ -lepton rest frame to the laboratory frame, and the invariant mass m_{vis} of the visible decay products. In the case of a leptonic τ decay two neutrinos are produced and the invariant mass of the two-neutrino system is the seventh parameter. The unknown parameters are constrained by four observables that are the components of the four-momentum of the system formed by the visible decay products of the τ lepton, measured in the laboratory frame. For each hadronic (leptonic) τ -lepton decay, 2 (3) parameters are thus left unconstrained. These parameters are chosen to be:

- x , the fraction of the τ -lepton energy in the laboratory frame carried by the visible decay products;
- ϕ , the azimuthal angle of the τ -lepton direction in the laboratory frame;
- $m_{\nu\nu}$, the invariant mass of the two-neutrino system in leptonic τ decays; for hadronic τ -lepton decays, we take $m_{\nu\nu} \equiv 0$ in the fit described below.

The two components E_x^{miss} and E_y^{miss} of the \vec{E}_T^{miss} provide two further constraints, albeit each with an experimental resolution of 10–15 GeV [32, 76].

The fact that the reconstruction of the τ -pair decay kinematics is underconstrained by the measured observables is addressed by a maximum likelihood fit method. The mass, $m_{\tau\tau}$, is reconstructed by combining the measured observables E_x^{miss} and E_y^{miss} with a likelihood model that includes terms for the τ -lepton decay kinematics and the E_T^{miss} resolution. The likelihood function $f(\vec{z}, \vec{y}, \vec{a}_1, \vec{a}_2)$ of the parameters $\vec{z} = (E_x^{\text{miss}}, E_y^{\text{miss}})$ in an event is constructed, given that the unknown parameters specifying the kinematics of the two τ -lepton decays have values $\vec{a}_1 = (x_1, \phi_1, m_{\nu\nu,1})$ and $\vec{a}_2 = (x_2, \phi_2, m_{\nu\nu,2})$, and that the four-momenta of the visible decay products have the measured values $\vec{y} = (p_1^{\text{vis}}, p_2^{\text{vis}})$. This likelihood model is used to compute the probability

$$P(m_{\tau\tau}^i) = \int \delta(m_{\tau\tau}^i - m_{\tau\tau}(\vec{y}, \vec{a}_1, \vec{a}_2)) f(\vec{z}, \vec{y}, \vec{a}_1, \vec{a}_2) d\vec{a}_1 d\vec{a}_2, \quad (5.1)$$

as a function of the mass hypothesis $m_{\tau\tau}^i$. The best estimate, $\hat{m}_{\tau\tau}$, for $m_{\tau\tau}$ is taken to be the value of $m_{\tau\tau}^i$ that maximizes $P(m_{\tau\tau}^i)$.

The likelihood $f(\vec{z}, \vec{y}, \vec{a}_1, \vec{a}_2)$ is the product of three likelihood functions: the first two functions model the decay parameters \vec{a}_1 and \vec{a}_2 of the two τ leptons, and the last one quantifies the compatibility of a τ -pair decay hypothesis with the measured \vec{E}_T^{miss} . The likelihood functions modelling the τ -lepton decay kinematics are different for leptonic and hadronic τ -lepton decays. Matrix elements for unpolarized τ -lepton decays from ref. [77] are used to model the differential distributions in the leptonic decays,

$$\mathcal{L}_{\tau,1} = \frac{d\Gamma}{dx dm_{\nu\nu} d\phi} \propto \frac{m_{\nu\nu}}{4m_\tau^2} [(m_\tau^2 + 2m_{\nu\nu}^2)(m_\tau^2 - m_{\nu\nu}^2)], \quad (5.2)$$

within the physically allowed region $0 \leq x \leq 1$ and $0 \leq m_{\nu\nu} \leq m_\tau \sqrt{1-x}$. For hadronic τ -lepton decays, a model based on the two-body phase space [78] is used, treating all the visible decay products of the τ lepton as a single system,

$$\mathcal{L}_{\tau,h} = \frac{d\Gamma}{dx d\phi} \propto \frac{1}{1 - m_{\text{vis}}^2/m_\tau^2}, \quad (5.3)$$

within the physically allowed region $m_{\text{vis}}^2/m_\tau^2 \leq x \leq 1$. It has been verified that the two-body phase space model is adequate for representing hadronic τ -lepton decays by comparing distributions generated by a parameterized MC simulation based on the two-body phase space model with results from the detailed simulation implemented in TAUOLA. The likelihood functions for hadronic (leptonic) τ -lepton decays do not depend on the parameters x , ϕ , and $m_{\nu\nu}$ (x and ϕ). The dependence on x enters via the integration boundaries. The dependence on ϕ comes from the likelihood function \mathcal{L}_ν , which quantifies the compatibility of a τ -lepton decay hypothesis with the reconstructed \vec{E}_T^{miss} in an event, assuming the neutrinos from the τ -lepton decays to be the only source of missing transverse energy. This likelihood function is defined as

$$\mathcal{L}_\nu(E_x^{\text{miss}}, E_y^{\text{miss}}) = \frac{1}{2\pi\sqrt{|V|}} \exp \left[-\frac{1}{2} \begin{pmatrix} E_x^{\text{miss}} - \sum p_x^\nu \\ E_y^{\text{miss}} - \sum p_y^\nu \end{pmatrix}^T V^{-1} \begin{pmatrix} E_x^{\text{miss}} - \sum p_x^\nu \\ E_y^{\text{miss}} - \sum p_y^\nu \end{pmatrix} \right]. \quad (5.4)$$

In this expression, the expected \vec{E}_T^{miss} resolution is represented by the covariance matrix V , estimated on an event-by-event basis using a \vec{E}_T^{miss} significance algorithm [76]; $|V|$ is the determinant of this matrix.

The relative $m_{\tau\tau}$ resolution achieved by the SVFIT algorithm is estimated from simulation and found to be about 10% in the $\tau_h\tau_h$ decay channel, 15% in the $\ell\tau_h$ channels, and 20% in the $\ell\ell'$ channels. The resolution varies at the level of a few percent between the different event categories defined in section 6 because in some categories events with a boosted (i.e. high- p_T) Higgs boson candidate and thus a better \vec{E}_T^{miss} resolution are selected. The $m_{\tau\tau}$ resolution for each channel and each category is listed in table 4 of appendix B. Figure 3 shows the normalized distributions of m_{vis} and $m_{\tau\tau}$ in the $\mu\tau_h$ channel after the baseline selection for simulated $Z \rightarrow \tau\tau$ events and simulated SM Higgs boson events with $m_H = 125$ GeV. The SVFIT mass reconstruction allows for a better separation between signal and background than m_{vis} alone, yielding an improvement in the final expected significance of $\sim 40\%$.

In the case of Higgs boson production in association with a W boson, the neutrino from the W-boson decay is an additional source of E_T^{miss} . Therefore, in the $\ell + L\tau_h$ channels, the signal is extracted from the distribution of the visible mass, m_{vis} , of the $L\tau_h$ system. In the $\ell + \ell'\tau_h$ channels, the visible mass is calculated from the τ_h and the electron or muon with smaller p_T .

6 Event categories

The event sample is split into mutually exclusive categories, defined to maximize the sensitivity of the analysis to the presence of a SM Higgs boson with a mass, m_H , between 110

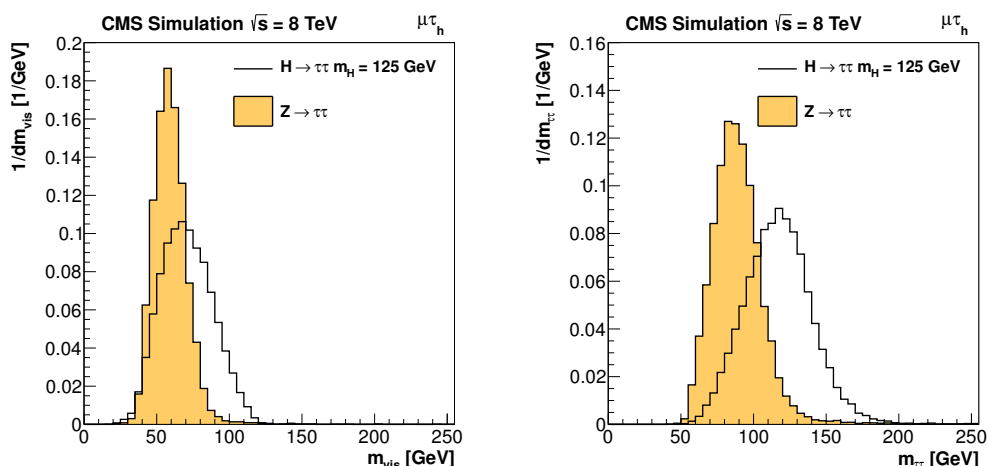


Figure 3. Normalized distributions obtained in the $\mu\tau_h$ channel after the baseline selection for (left) the invariant mass, m_{vis} , of the visible decay products of the two τ leptons, and (right) the SVFIT mass, $m_{\tau\tau}$. The distribution obtained for a simulated sample of $Z \rightarrow \tau\tau$ events (shaded histogram) is compared to the one obtained for a signal sample with a SM Higgs boson of mass $m_H = 125$ GeV (open histogram).

and 145 GeV. The categories for the LL' channels are schematically represented in figure 4 and described below.

In each channel, events are first classified according to the number of reconstructed jets with transverse momentum and pseudorapidity $p_T^j > 30$ GeV and $|\eta^j| < 4.7$, and a separation in (η, ϕ) space between the jet and all selected leptons of $\Delta R^{jL} > 0.5$. In all categories, events containing at least one b-tagged jet with $p_T^j > 20$ GeV are rejected to reduce the $t\bar{t}$ background.

In the $\mu\tau_h$, $e\tau_h$, $\tau_h\tau_h$ and $e\mu$ channels, events with at least two jets are further required to pass a set of criteria targeting signal events where the Higgs boson is produced via VBF, i.e. in association with two jets separated by a large pseudorapidity gap. This “VBF tag” strongly suppresses the background, in particular the irreducible $Z \rightarrow \tau\tau$ background. This background is suppressed for two main reasons: first, because the requirement of two high- p_T jets is effective in rejecting the gluon-initiated jets from initial state radiation in the Drell-Yan production process; second, because such jets are typically produced in the central region of the detector. The VBF-tagged category consists of events for which the two highest- p_T jets have a large invariant mass, m_{jj} , and a large separation in pseudorapidity, $|\Delta\eta_{jj}|$. A central-jet veto is applied by not allowing any additional jet in the pseudorapidity region delimited by the two highest- p_T jets. For the analysis of the 8 TeV data, the VBF-tagged category is further split into tight and loose sub-categories. In the ee and $\mu\mu$ channels, events with two jets or more are not required to fulfil any additional selection criteria, except for the central-jet veto. Instead, a multivariate discriminant involving m_{jj} and $|\Delta\eta_{jj}|$ is used to extract the signal, as described in section 9.

Events failing the VBF tag requirements, or the 2-jet category selection in the case of the ee and $\mu\mu$ channels, are collected in the 1-jet category if they contain at least one

		0-jet	1-jet		2-jet	
$\mu\tau_h$	$p_T^{\text{th}} > 45 \text{ GeV}$	high- p_T^{th}	high- p_T^{th}	$p_T^{\tau\tau} > 100 \text{ GeV}$ high- p_T^{th} boosted	loose VBF tag	tight VBF tag (2012 only)
	baseline	low- p_T^{th}	low- p_T^{th}			
$e\tau_h$	$p_T^{\text{th}} > 45 \text{ GeV}$	high- p_T^{th}	high- p_T^{th}	high- p_T^{th} boosted	loose VBF tag	tight VBF tag (2012 only)
	baseline	low- p_T^{th}	low- p_T^{th}			
$e\mu$	$p_T^\mu > 35 \text{ GeV}$	high- p_T^μ	high- p_T^μ		loose VBF tag	tight VBF tag (2012 only)
	baseline	low- p_T^μ	low- p_T^μ			
$ee, \mu\mu$	$p_T^l > 35 \text{ GeV}$	high- p_T^l	high- p_T^l		2-jet	
	baseline	low- p_T^l	low- p_T^l			
$\tau_h\tau_h$ (8 TeV only)	baseline		boosted	highly boosted	VBF tag	
			$p_T^{\tau\tau} > 100 \text{ GeV}$	$p_T^{\tau\tau} > 170 \text{ GeV}$		

Figure 4. Event categories for the LL' channels. The $p_T^{\tau\tau}$ variable is the transverse momentum of the Higgs boson candidate. In the definition of the VBF-tagged categories, $|\Delta\eta_{jj}|$ is the difference in pseudorapidity between the two highest- p_T jets, and m_{jj} their invariant mass. In the $\mu\mu$ and ee channels, events with two or more jets are not required to fulfil any additional VBF tagging criteria. For the analysis of the 7 TeV $e\tau_h$ and $\mu\tau_h$ data, the loose and tight VBF-tagged categories are merged into a single VBF-tagged category. In the $e\tau_h$ channel, the E_T^{miss} is required to be larger than 30 GeV in the 1-jet category. Therefore, the high- p_T^{th} category is not used and is accordingly crossed out. The term “baseline” refers to the baseline selection described in section 4.

jet, and in the 0-jet category otherwise. The latter has low sensitivity to the presence of a SM Higgs boson and is mainly used to constrain the $Z \rightarrow \tau\tau$ background for the more sensitive categories. The $\tau_h\tau_h$ channel does not feature a 0-jet category because of the large background from QCD multijet events.

The 1-jet and 2-jet categories are further split according to the transverse momentum of the Higgs boson candidate, defined as

$$p_T^{\tau\tau} = |\vec{p}_T^L + \vec{p}_T^{L'} + \vec{E}_T^{\text{miss}}|, \quad (6.1)$$

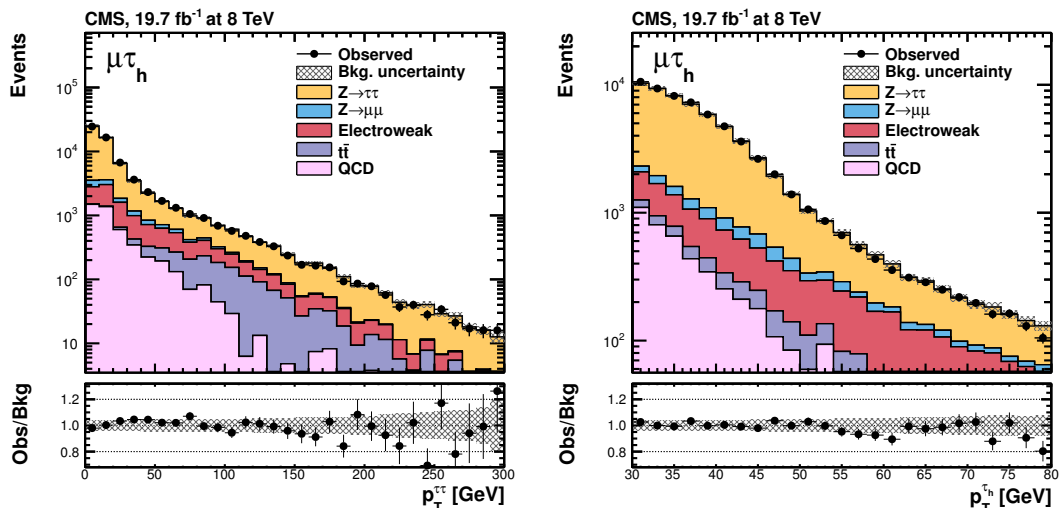


Figure 5. Observed and predicted distributions in the $\mu\tau_h$ channel after the baseline selection, for (left) the transverse momentum of the Higgs boson candidates and (right) the transverse momentum of the τ_h . The yields predicted for the various background contributions correspond to the result of the final fit presented in section 9. The electroweak background contribution includes events from $W + \text{jets}$, diboson, and single-top-quark production. The “bkg. uncertainty” band represents the combined statistical and systematic uncertainty in the background yield in each bin. In each plot, the bottom inset shows the ratio of the observed and predicted numbers of events. The expected contribution from the SM Higgs signal is negligible.

where \vec{p}_T^L and $\vec{p}_T^{L'}$ denote the transverse momenta of the two leptons. The $p_T^{\tau\tau}$ variable is used to select sub-categories in which the Higgs boson candidate is boosted in the transverse plane. The $m_{\tau\tau}$ resolution is improved for such events and a better separation between the $H \rightarrow \tau\tau$ signal and the $Z \rightarrow \tau\tau$ background is achieved. This selection also has the advantage of reducing the QCD multijet background which is especially large in the $\tau_h\tau_h$ channel.

The 0-jet and 1-jet categories are further divided into low and high p_T^L categories, where (i) $L = \tau_h$ in the $\ell\tau_h$ channels, (ii) $L = \mu$ in the $e\mu$ channel, and (iii) L is the highest- p_T lepton in the ee and $\mu\mu$ channels. For $m_H > m_Z$, higher- p_T leptons are produced in the $H \rightarrow \tau\tau$ process than in the $Z \rightarrow \tau\tau$ process. Selecting high- p_T leptons also reduces the contribution of background events in which a jet is misidentified as a lepton. Figure 5 demonstrates a good modelling of the $p_T^{\tau\tau}$ and $p_T^{\tau_h}$ distributions for the $\mu\tau_h$ channel, after the baseline selection.

In the 1-jet category of the $e\tau_h$ channel, the background from $Z \rightarrow ee$ events in which an electron is misidentified as a τ_h is reduced by requiring $E_T^{\text{miss}} > 30 \text{ GeV}$. This extra requirement makes it difficult to predict the $m_{\tau\tau}$ distribution for the $Z \rightarrow \tau\tau$ background events in the 1-jet high- $p_T^{\tau_h}$ category. This category, which has relatively low sensitivity, is therefore ignored in the $e\tau_h$ channel.

For the 8 TeV dataset, events in the $\ell + \ell'\tau_h$ channels are categorized according to L_T with a threshold at 130 GeV. The $\ell + \tau_h\tau_h$ and $\ell\ell + LL'$ samples are not split into categories.

7 Background estimation

The estimation of the shape and yield of the major backgrounds in each channel is based on the observed data. The experimental systematic uncertainties affecting the background shapes and yields are thus directly related to the background estimation techniques and are also discussed in this section.

In the $\mu\tau_h$, $e\tau_h$, $\tau_h\tau_h$, and $e\mu$ channels, the largest source of background is the Drell-Yan production of $Z \rightarrow \tau\tau$. This contribution is greatly reduced by the 1-jet and VBF tag selection criteria as the jet-multiplicity distribution in Drell-Yan production falls off steeply. It is modelled using “embedded” event samples recorded in each data-taking period under a loose $Z \rightarrow \mu\mu$ selection. In each event, the PF muons are replaced by the PF particles reconstructed from the visible decay products of the τ leptons in simulated $Z \rightarrow \tau\tau$ events, before reconstructing the \vec{E}_T^{miss} , the jets, the τ_h candidates, and the lepton isolation. The Drell-Yan event yield is rescaled to the observed yield using the inclusive sample of $Z \rightarrow \mu\mu$ events; thus, for this dominant background, the systematic uncertainties in the jet energy scale, the missing transverse energy, and the luminosity measurement are negligible. Additional uncertainties arise due to the extrapolation to the different event categories. These include uncertainties in the event reconstruction and acceptance of the “embedded” event samples that are estimated in simulated events as well as statistical uncertainties due to the limited number of events in these samples. In the $e\tau_h$ and $\mu\tau_h$ channels, the largest remaining systematic uncertainty affecting the $Z \rightarrow \tau\tau$ background yield is due to the τ_h selection efficiency. This uncertainty, which includes the uncertainty in the efficiency to trigger on a τ_h , is estimated to be 8% in an independent study based on a tag-and-probe method [79] and, in addition, a $\mu\tau_h$ event sample recorded with single-muon triggers.

The Drell-Yan production of $Z \rightarrow \ell\ell$ is the largest background in the $\ell\ell$ channels. The $Z \rightarrow \ell\ell$ event yield is normalized to the data in each category after subtracting all backgrounds. In the $e\tau_h$ channel, $Z \rightarrow \ell\ell$ production is also an important source of background because of the 2–3% probability for electrons to be misidentified as a τ_h [36] and the fact that the reconstructed $m_{\tau\tau}$ distribution peaks in the Higgs boson mass search range. Because of the lower $\mu \rightarrow \tau_h$ misidentification rate, the $Z \rightarrow \ell\ell$ contribution in the $\mu\tau_h$ channel is small. The contribution of this background is estimated from simulation in both channels, after rescaling the simulated Drell-Yan yield to the one derived from $Z \rightarrow \mu\mu$ data. The dominant systematic uncertainty in the $Z \rightarrow \ell\ell$ background yields arises from the $\ell \rightarrow \tau_h$ misidentification rate. This uncertainty is estimated using the tag-and-probe method with $Z \rightarrow \ell\ell$ event samples, and is found to be 20% for electrons and 30% for muons. The small contribution from $Z \rightarrow \ell\ell$ events in the $\mu\tau_h$, $e\tau_h$, and $\tau_h\tau_h$ channels where a lepton is lost and a jet is misidentified as a τ_h candidate is also estimated from simulation. Depending on the event category, the uncertainties range from 20% to 80%, including uncertainties in the jet $\rightarrow \tau_h$ misidentification rate and statistical uncertainties due to the limited number of simulated events.

The background from W + jets production contributes significantly to the $e\tau_h$ and $\mu\tau_h$ channels when the W boson decays leptonically and a jet is misidentified as a τ_h . The

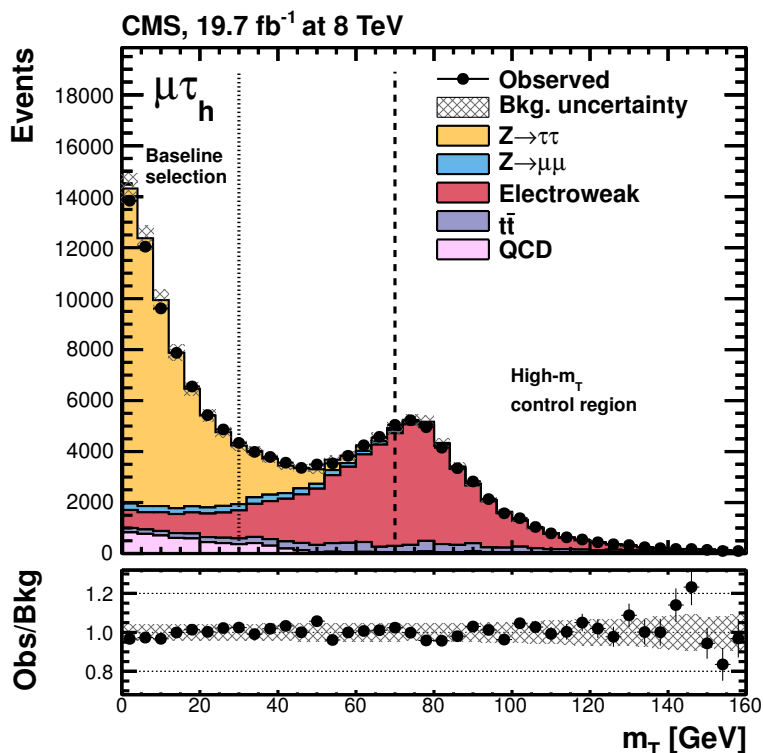


Figure 6. Observed and predicted m_T distribution in the 8 TeV $\mu\tau_h$ analysis after the baseline selection but before applying the $m_T < 30$ GeV requirement, illustrated as a dotted vertical line. The dashed line delimits the high- m_T control region that is used to normalize the yield of the W+jets contribution in the analysis as described in the text. The yields predicted for the various background contributions correspond to the result of the final fit presented in section 9. The electroweak background contribution includes events from W + jets, diboson, and single-top-quark production. The “bkg. uncertainty” band represents the combined statistical and systematic uncertainty in the background yield in each bin. The bottom inset shows the ratio of the observed and predicted numbers of events. The expected contribution from a SM Higgs signal is negligible.

background shape for these channels is modelled using the simulation. Figure 6 shows the observed and predicted m_T distribution obtained in the 8 TeV $\mu\tau_h$ channel after the baseline selection but without the $m_T < 30$ GeV requirement. In each category, the W+jets background yield in a high- m_T control region is normalized to the observed yield. The extrapolation factor to the low- m_T signal region is obtained from the simulation and has an estimated systematic uncertainty of 10% to 25%, depending on the event category. The uncertainty is estimated by comparing the m_T distribution in simulated and recorded $Z(\rightarrow \mu\mu) + \text{jets}$ events in which a reconstructed muon is removed from the event to emulate W + jets events. In the high- m_T region of figure 6 the observed and predicted yields match by construction, and the agreement in shape indicates good modelling of the \vec{E}_T^{miss} in the simulation. In the VBF-tagged categories, where the number of simulated W + jets events is small, smooth $m_{\tau\tau}$ templates are obtained by loosening the VBF selection criteria. The $m_{\tau\tau}$ bias introduced in doing so was found to be negligible in a much larger sample of events obtained by relaxing the m_T selection. For the $\tau_h\tau_h$ channel, a $\mu\tau_h$ control sample

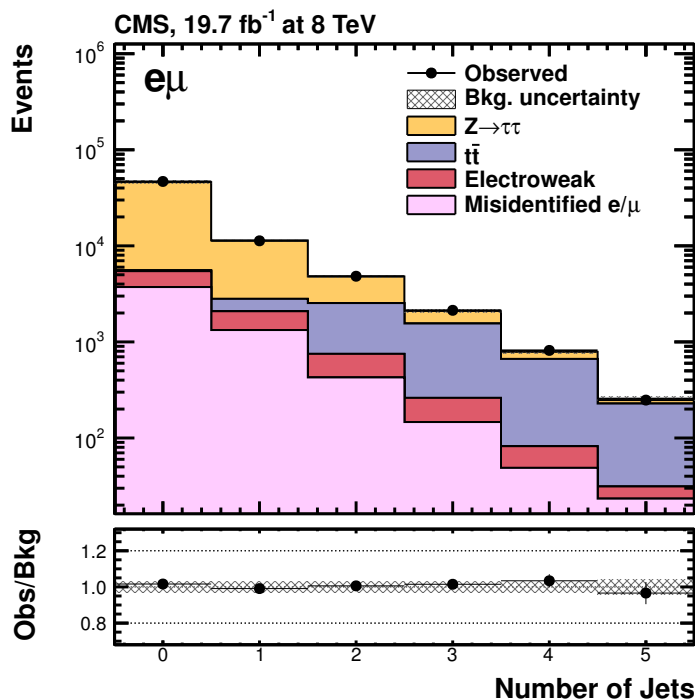


Figure 7. Observed and predicted distribution for the number of jets in the 8 TeV $e\mu$ analysis after the baseline selection described in section 4. The yields predicted for the various background contributions correspond to the result of the final fit presented in section 9. The electroweak background contribution includes events from diboson and single-top-quark production. The “bkg. uncertainty” band represents the combined statistical and systematic uncertainty in the background yield in each bin. The bottom inset shows the ratio of the observed and predicted numbers of events. The expected contribution from a SM Higgs signal is negligible.

is used to define the same categories as in the $\tau_h\tau_h$ channel. In each of these categories, the $W + \text{jets}$ background is normalized to the yield observed in the high- m_T control region through a factor that is then used to scale the $W + \text{jets}$ background in the $\tau_h\tau_h$ sample, with a 30% systematic uncertainty.

The $t\bar{t}$ production process is one of the main backgrounds in the $e\mu$ channel. Its shape for all LL' channels is predicted by the simulation, and the yield is adjusted to the one observed using a $t\bar{t}$ -enriched control sample, extracted by requiring b-tagged jets in the final state. The systematic uncertainty in the yield includes, among others, the systematic uncertainty in the b-tagging efficiency, which ranges from 1.5% to 7.4% depending on the b-tagged jet p_T [30]. Furthermore, it is affected by systematic uncertainties in the jet energy scale, the E_T^{miss} scale, and the background yields in the control sample. Figure 7 shows a good agreement between the observed and predicted distributions for the number of jets after the baseline selection in the 8 TeV $e\mu$ analysis, in particular for events with three or more jets, for which the $t\bar{t}$ process dominates.

QCD multijet events, in which one jet is misidentified as a τ_h and another as an ℓ , constitute another important source of background in the $\ell\tau_h$ channels. In the 0-jet and 1-jet low- $p_T^{\tau_h}$ categories that have a high event yield, the QCD multijet background

yield is obtained using a control sample where the ℓ and the τ_h are required to have the same charge. In this control sample, the QCD multijet yield is obtained by subtracting from the data the contribution of the Drell-Yan, $t\bar{t}$, and $W + \text{jets}$ processes, estimated as explained above. The expected contribution of the QCD multijet background in the opposite-charge signal sample is then derived by rescaling the yield obtained in the same-charge control sample by a factor of 1.06, which is measured using a pure QCD multijet sample obtained by inverting the ℓ isolation requirement and relaxing the τ_h isolation requirement. The 10% systematic uncertainty in this factor accounts for a small dependence on $p_T^{\tau_h}$ and the statistical uncertainty in the measurement, and dominates the uncertainty in the yield of this background contribution. In the VBF-tagged and 1-jet high- $p_T^{\tau_h}$ boosted categories, the number of events in the same-charge control sample is too small to use this procedure. Instead, the QCD multijet yield is obtained by multiplying the QCD multijet yield estimated after the baseline selection by the category selection efficiency. This efficiency is measured using a sample dominated by QCD multijet production in which the ℓ and the τ_h are not isolated. The yield is affected by a 20% systematic uncertainty. In all categories, the $m_{\tau\tau}$ template is obtained from a same-charge control region in which the ℓ isolation requirement is inverted. In addition, the VBF tagging and the τ_h isolation criteria are relaxed in the VBF-tagged and 1-jet high- $p_T^{\tau_h}$ boosted categories, respectively, to obtain a smooth template shape.

In the $\tau_h\tau_h$ channel, the large QCD multijet background is estimated from a control region with a relaxed τ_h isolation requirement, disjoint from the signal region. In this region, the QCD multijet background shape and yield are obtained by subtracting from the observed data the contribution of the Drell-Yan, $t\bar{t}$, and $W + \text{jets}$ processes, estimated as explained above. The QCD multijet background yield in the signal region is obtained by multiplying the yield in the control region by an extrapolation factor, obtained using identical signal region and control region definitions applied to a sample of same-charge $\tau_h\tau_h$ events. Depending on the event category, the systematic uncertainty in this yield is estimated to range from 35% to 50%. The uncertainty includes contributions from the limited number of events in the control region and uncertainties in the expected yields of the subtracted background components. The QCD multijet background shape in the signal region is taken to be the same as in the control region with a relaxed τ_h isolation requirement, an assumption that is verified by comparing the QCD multijet shapes obtained in the signal region and in the control region of the same-charge sample.

The small background due to $W + \text{jets}$ and QCD multijet production in the $e\mu$ channel corresponds to events in which one or two jets are misidentified as leptons, and is denoted as the “misidentified- ℓ ” background. A misidentified- ℓ control region is defined by requiring the ℓ to pass relaxed selection criteria, and to fail the nominal selection criteria. The expected contribution from processes with a dilepton final state is subtracted. The number of events N_ℓ in the signal region in which a jet is misidentified as an ℓ is estimated as the yield in the misidentified- ℓ control region multiplied by the ratio between the yields measured in the signal and control regions using a multijet sample. The procedure is applied separately for electrons and muons, leading to the estimation of N_e and N_μ . The number of events for which two jets are misidentified as an electron and a muon, $N_{e\mu}$, is

estimated from a control region in which both the electron and the muon pass the relaxed selection criteria and fail the nominal selection criteria. The background yield in the signal region is then estimated as $N_e + N_\mu - N_{e\mu}$. In the 0-jet and 1-jet low- p_T^{th} categories, the $m_{\tau\tau}$ template is taken from a same-charge control region with inverted electron isolation requirement. In the 1-jet high- p_T^{th} and VBF-tagged categories, the number of events in this control region is too small and the template is instead taken from the opposite-charge misidentified-electron control region.

The small contributions from diboson and single-top-quark production in the LL' channels are taken from simulation. For $m_H = 125$ GeV, the contribution from $H \rightarrow WW$ decays amounts to up to 45% of the expected SM Higgs boson signal in the VBF-tagged categories in the $e\mu$ channel, and to up to 60% of the complete expected SM Higgs boson signal in the 2-jet categories of the ee and $\mu\mu$ channels. In all other LL' channels, the contribution from $H \rightarrow WW$ decays is negligible.

In the $\ell + L\tau_h$ channels, the irreducible background is due to WZ and ZZ production, while the reducible background comes from QCD multijet, $W + \text{jets}$, $Z + \text{jets}$, $W + \gamma$, $Z + \gamma$, and $t\bar{t}$ production. In the $\ell\ell + LL'$ channels, ZZ production and $t\bar{t}$ production in association with a Z boson constitute the sources of irreducible background; the reducible background comes from $WZ + \text{jets}$, $Z + \text{jets}$, and $t\bar{t}$ production. Events from reducible background sources contain at least one jet misidentified as a lepton. For each channel, the reducible background contribution is estimated from sidebands in which one or more lepton candidates satisfy relaxed selection criteria but do not satisfy the nominal selection criteria. The number of reducible background events for which all leptons satisfy the nominal selection criteria is obtained by weighting the sideband events according to the probability for a lepton passing the relaxed selection criteria to also pass the nominal selection criteria. These misidentification probabilities are measured in independent control samples of QCD multijet, $W(\rightarrow \ell\nu) + \text{jets}$, and $Z(\rightarrow \ell\ell) + \text{jets}$ events with one lepton passing the relaxed selection criteria in addition to the well-identified leptons corresponding to the decay of the W or Z boson, if any. The misidentification probabilities are parameterized as a function of the lepton p_T , the number of jets in the event, and, in case a jet is found close to the lepton, the jet p_T . To obtain a smooth template shape, the isolation criteria for the leptons associated to the Higgs boson decay are relaxed in the $\ell\ell + LL'$ channels. The systematic uncertainties in the event yield of the reducible background components range from 15 to 30%. They include contributions from the limited number of events in the sideband, uncertainties in the estimation of the misidentification probabilities, and uncertainties in the background composition in the sidebands.

8 Systematic uncertainties

The values of a number of imprecisely known quantities can affect the rates and shapes of the $m_{\tau\tau}$ distributions for the signal and background processes. These systematic uncertainties can be grouped into theory related uncertainties, which are predominantly relevant for the expected signal yields, and into uncertainties from experimental sources, which can further be subdivided into uncertainties related to the reconstruction of physics objects and

uncertainties in the background estimation. The uncertainties related to the reconstruction of physics objects apply to processes estimated with simulated samples, most importantly the signal processes. As outlined in the previous section, the distributions for several background processes are estimated from data, and the corresponding systematic uncertainties are therefore mostly uncorrelated with the ones affecting the signal distributions.

The main experimental uncertainties in the decay channels involving a τ_h are related to the reconstruction of this object. The τ_h energy scale is obtained from a template fit to the τ_h mass distribution, such as the one shown in figure 2. In this fit, the shape of the mass distribution is morphed as a function of the τ_h energy scale parameter. The uncertainty of $\pm 3\%$ in the energy scale of each τ_h affects both the shape and the rate of the relevant signal and background distributions in each category. The τ_h identification and trigger efficiencies for genuine τ leptons sum up to an overall rate uncertainty of 6 to 10% per τ_h , depending on the decay channel, due to the different trigger and ℓ rejection criteria and additional uncertainties for higher $p_T^{\tau_h}$. For $Z \rightarrow \ell\ell$ events where jets, muons, or electrons are misidentified as τ_h , the estimation of the τ_h identification efficiency leads to rate uncertainties of 20 to 80%, including the statistical uncertainty due to the limited number of simulated events.

In the decay channels with muons or electrons, the uncertainties in the muon and electron identification, isolation, and trigger efficiencies lead to rate uncertainties of 2 to 4% for muons and 2 to 6% for electrons. The uncertainty in the electron energy scale is relevant only in the $e\mu$ and ee channels, where it affects the normalization and shape of the simulated $m_{\tau\tau}$ and final discriminant distributions. The uncertainty in the muon energy scale is found to have a negligible effect for all channels. The relative E_T^{miss} scale uncertainty of 5% affects the event yields for all channels making use of the E_T^{miss} in the event selection, in particular for the $\ell\tau_h$ channels due to the m_T selection [32]. This translates into yield uncertainties of 1 to 12%, depending on the channel and the event category. The uncertainties are largest for event categories with a minimum E_T^{miss} requirement and for background contributions with no physical source of E_T^{miss} , e.g. the $Z \rightarrow ee$ contribution in the high- $p_T^{\tau_h}$ boosted category in the $e\tau_h$ channel. The uncertainty in the jet energy scale varies with jet p_T and jet η [29] and leads to rate uncertainties for the signal contributions of up to 20% in the VBF-tagged categories. For the most important background samples, the effect on the rate is, however, well below 5%. Because of the veto of events with b-tagged jets, uncertainties in the tagging efficiency for b-quark jets and in the mistagging efficiency for c-quark, light-flavour, and gluon jets result in rate uncertainties of up to 8% for the different signal and background components. The uncertainty in the integrated luminosity amounts to 2.2% for the 7 TeV analysis [80] and 2.6% for the 8 TeV analysis [81], yielding corresponding rate uncertainties for the affected signal and background samples.

The uncertainties related to the estimation of the different background processes are discussed in detail in the previous section, and only a summary is given here. For the different Drell-Yan decay modes, the uncertainty in the inclusive $Z \rightarrow \tau\tau$ yield is 3%, with additional extrapolation uncertainties in the different categories in the range of 2 to 14%. The uncertainties in the $W + \text{jets}$ event yields estimated from data are in the range of 10–100%. The values are dominated by the statistical uncertainties involved in

the extrapolation from high to low m_T and due to the limited number of data events in the high- m_T control region. As a consequence, they are treated as uncorrelated with any other uncertainty. The QCD multijet background estimation results in 6 to 35% rate uncertainties for the LL' channels, except for the very pure dimuon final state and the VBF-tagged categories where uncertainties of up to 100% are estimated. Additional shape uncertainties are included in the $e\tau_h$, $\mu\tau_h$, and $e\mu$ channels to account for the uncertainty in the shape estimation from the control regions.

The rate and acceptance uncertainties for the signal processes related to the theoretical calculations are due to uncertainties in the parton distribution functions (PDF), variations of the renormalization and factorization scales, and uncertainties in the modelling of the underlying event and parton showers. The magnitude of the rate uncertainty depends on the production process and on the event category. In the VBF-tagged categories, the theoretical uncertainties concerning the $qq' \rightarrow H$ process are 4% from the PDFs and 3% from scale variations. The rate and acceptance uncertainties in the $gg \rightarrow H$ process in the VBF-tagged categories are estimated by comparing the four different MC generators POWHEG, MADGRAPH, POWHEG interfaced with MINLO [82], and aMC@NLO [83]. They amount to 30% and thus become of similar absolute size as the uncertainties in the $qq' \rightarrow H$ process.

For the $gg \rightarrow H$ process, additional uncertainties are incorporated to account for missing higher-order corrections ranging from 10 to 41% depending on the category and on the decay channel. The combined systematic uncertainty in the background yield arising from diboson and single-top-quark production processes is estimated to be 15% for the LL' channels based on recent CMS measurements [84, 85]. In the $\ell + L\tau_h$ and $\ell\ell + LL'$ channels, the uncertainties in the event yields of WZ production and ZZ production arise from scale variations and uncertainties in the PDFs, including the PDF uncertainties in the $gg \rightarrow ZZ$ event yields which are 44%. The resulting overall uncertainties range from 4 to 8%. The uncertainties in the small background from $t\bar{t} + Z$ production in the $\ell\ell + LL'$ channels amount to 50% [86].

In addition, uncertainties due to the limited number of simulated events or due to the limited number of events in data control regions are taken into account. These uncertainties are uncorrelated across bins in the individual templates. A summary of the considered systematic uncertainties is given in table 3.

9 Results

The search for an excess of SM Higgs boson events over the expected background involves a global maximum likelihood fit based on final discriminating variables which are either $m_{\tau\tau}$ or m_{vis} in all channels except for ee and $\mu\mu$ [87, 88]. In these two channels the final discriminating variable D is built for a given event from the output of two boosted decision trees B_1 and B_2 . The two BDTs are based on kinematic variables related to the $\ell\ell$ system and the \vec{E}_T^{miss} , on the distance of closest approach between the leptons, and, in the 2-jet category, the m_{jj} and $|\Delta\eta_{jj}|$ variables. The first BDT is trained to discriminate $Z \rightarrow \tau\tau$ from $Z \rightarrow \ell\ell$ events, whereas the second BDT is trained to discriminate $H \rightarrow \tau\tau$ from $Z \rightarrow \tau\tau$ events. Both BDTs are separately trained in the 2-jet category and in the combined 0-jet

Uncertainty	Affected processes	Change in acceptance
Tau energy scale	signal & sim. backgrounds	1–29%
Tau ID (& trigger)	signal & sim. backgrounds	6–19%
e misidentified as τ_h	Z \rightarrow ee	20–74%
μ misidentified as τ_h	Z \rightarrow $\mu\mu$	30%
Jet misidentified as τ_h	Z + jets	20–80%
Electron ID & trigger	signal & sim. backgrounds	2–6%
Muon ID & trigger	signal & sim. backgrounds	2–4%
Electron energy scale	signal & sim. backgrounds	up to 13%
Jet energy scale	signal & sim. backgrounds	up to 20%
E_T^{miss} scale	signal & sim. backgrounds	1–12%
$\varepsilon_{\text{b-tag}}$ b jets	signal & sim. backgrounds	up to 8%
$\varepsilon_{\text{b-tag}}$ light-flavoured jets	signal & sim. backgrounds	1–3%
Norm. Z production	Z	3%
Z \rightarrow $\tau\tau$ category	Z \rightarrow $\tau\tau$	2–14%
Norm. W + jets	W + jets	10–100%
Norm. $t\bar{t}$	$t\bar{t}$	8–35%
Norm. diboson	diboson	6–45%
Norm. QCD multijet	QCD multijet	6–70%
Shape QCD multijet	QCD multijet	shape only
Norm. reducible background	Reducible bkg.	15–30%
Shape reducible background	Reducible bkg.	shape only
Luminosity 7 TeV (8 TeV)	signal & sim. backgrounds	2.2% (2.6%)
PDF (qq)	signal & sim. backgrounds	4–5%
PDF (gg)	signal & sim. backgrounds	10%
Norm. ZZ/WZ	ZZ/WZ	4–8%
Norm. $t\bar{t}$ + Z	$t\bar{t}$ + Z	50%
Scale variation	signal	3–41%
Underlying event & parton shower	signal	2–10%
Limited number of events	all	shape only

Table 3. Systematic uncertainties, affected samples, and change in acceptance resulting from a variation of the nuisance parameter equivalent to one standard deviation. Several systematic uncertainties are treated as (partially) correlated for different decay channels and/or categories.

and 1-jet categories. The final discriminant is defined as

$$D = \int_{-\infty}^{B_1} \int_{-\infty}^{B_2} f_{\text{sig}}(B'_1, B'_2) dB'_1 dB'_2. \quad (9.1)$$

In this expression, f_{sig} is the two-dimensional joint probability density for the signal. Therefore, D represents the probability for a signal event to have a value lower than B_1 for the first BDT and B_2 for the second BDT.

Figures 8 and 9 show the $m_{\tau\tau}$ distributions observed for the 8 TeV dataset in the most sensitive categories of the $\mu\tau_h$, $e\tau_h$, $\tau_h\tau_h$, and $e\mu$ channels together with the background distributions resulting from the global fit described in detail below. The discriminator distributions for the 8 TeV dataset in the $\ell\ell$ channels are shown in figure 10. The complete set of distributions is presented in appendix A. The signal prediction for a Higgs boson

with $m_H = 125$ GeV is normalized to the SM expectation. The corresponding event yields for all event categories are given in tables 4 and 5 in appendix B.

For the global fit, the distributions of the final discriminating variable obtained for each category and each channel at 7 and 8 TeV are combined in a binned likelihood, involving the expected and observed numbers of events in each bin. The expected number of signal events is the one predicted by the SM for the production of a Higgs boson of mass m_H decaying into a pair of τ leptons, multiplied by a signal strength modifier μ treated as free parameter in the fit.

The systematic uncertainties are represented by nuisance parameters that are varied in the fit according to their probability density function. A log-normal probability density function is assumed for the nuisance parameters affecting the event yields of the various background contributions. Systematic uncertainties that affect the template shapes, e.g. the τ_h energy scale uncertainty, are represented by nuisance parameters whose variation results in a continuous perturbation of the spectrum [89] and which are assumed to have a Gaussian probability density function.

Nuisance parameters affect the yields and template shapes across categories and channels when applicable. For example, in the VBF-tagged categories of the $\mu\tau_h$ channel, the most important nuisance parameters related to background normalization are the ones affecting the $Z \rightarrow \tau\tau$ yield (τ_h selection efficiency) and the $W + \text{jets}$ yield (statistical uncertainty for the normalization to the yield in the high- m_T region, and extrapolation to the low- m_T region). The nuisance parameter affecting the $W + \text{jets}$ yield is constrained only by the events observed in the given category, in particular in the high-mass region. The nuisance parameters related to the τ_h identification efficiency and to the τ_h energy scale are, however, mostly constrained by the 0-jet and 1-jet categories, for which the number of events in the $Z \rightarrow \tau\tau$ peak is very large. Overall, the statistical uncertainty in the observed event yields is the dominant source of uncertainty for all combined results.

The excess of events observed in the most sensitive categories of figures 8 and 9 is highlighted in figure 11, which shows the observed and expected $m_{\tau\tau}$ distributions for all categories of the $\ell\tau_h$, $e\mu$, and $\tau_h\tau_h$ channels combined. The ee and $\mu\mu$ channels are not included because the final discrimination is based on D instead of $m_{\tau\tau}$ in these channels. The distributions are weighted in each category of each channel by the $S/(S+B)$ ratio where S is the expected signal yield for a SM Higgs boson with $m_H = 125$ GeV ($\mu = 1$) and B is the predicted background yield corresponding to the result of the global fit. The ratio is obtained in the central $m_{\tau\tau}$ interval containing 68% of the signal events. The figure also shows the difference between the observed data and expected background distributions, together with the expected distribution for a SM Higgs boson signal with $m_H = 125$ GeV.

The visible excess in the weighted $m_{\tau\tau}$ distribution is quantified by calculating the corresponding local p -values for the LL' channels using a profile-likelihood ratio test statistics [87, 88]. Figure 12 shows the distribution of local p -values and significances as a function of the Higgs boson mass hypothesis. The expected significance for a SM Higgs boson with $m_H = 125$ GeV is 3.6 standard deviations. For m_H between 110 and 130 GeV, the observed significance is larger than three standard deviations, and equals 3.4 standard deviations for $m_H = 125$ GeV. The corresponding best-fit value for μ is $\hat{\mu} = 0.86 \pm 0.29$ at $m_H = 125$ GeV.

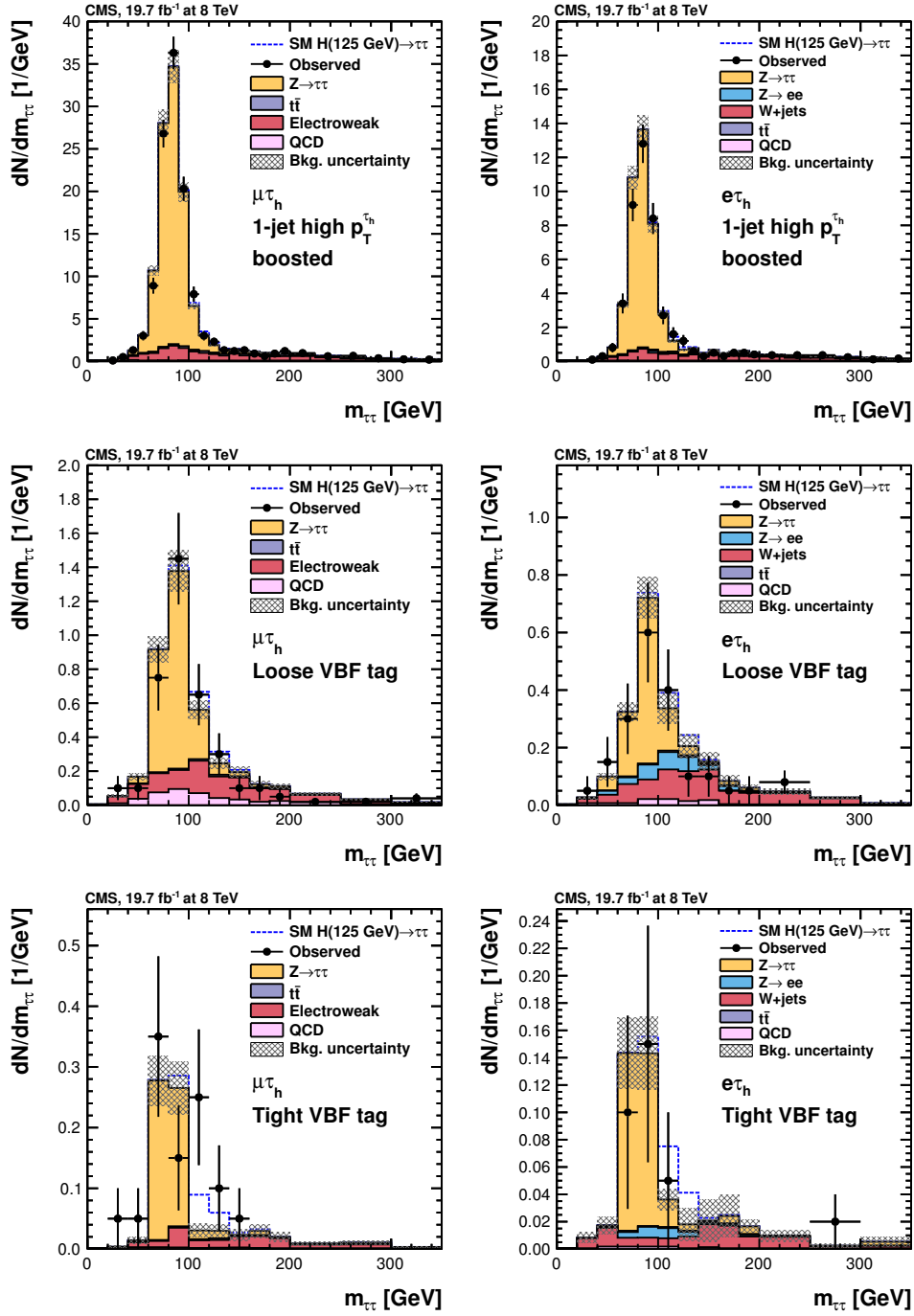


Figure 8. Observed and predicted $m_{\tau\tau}$ distributions in the 8 TeV $\mu\tau_h$ (left) and $e\tau_h$ (right) channels, and for the 1-jet high- p_T^h boosted (top), loose VBF tag (middle), and tight VBF tag (bottom) categories. The normalization of the predicted background distributions corresponds to the result of the global fit. The signal distribution, on the other hand, is normalized to the SM prediction. The signal and background histograms are stacked.

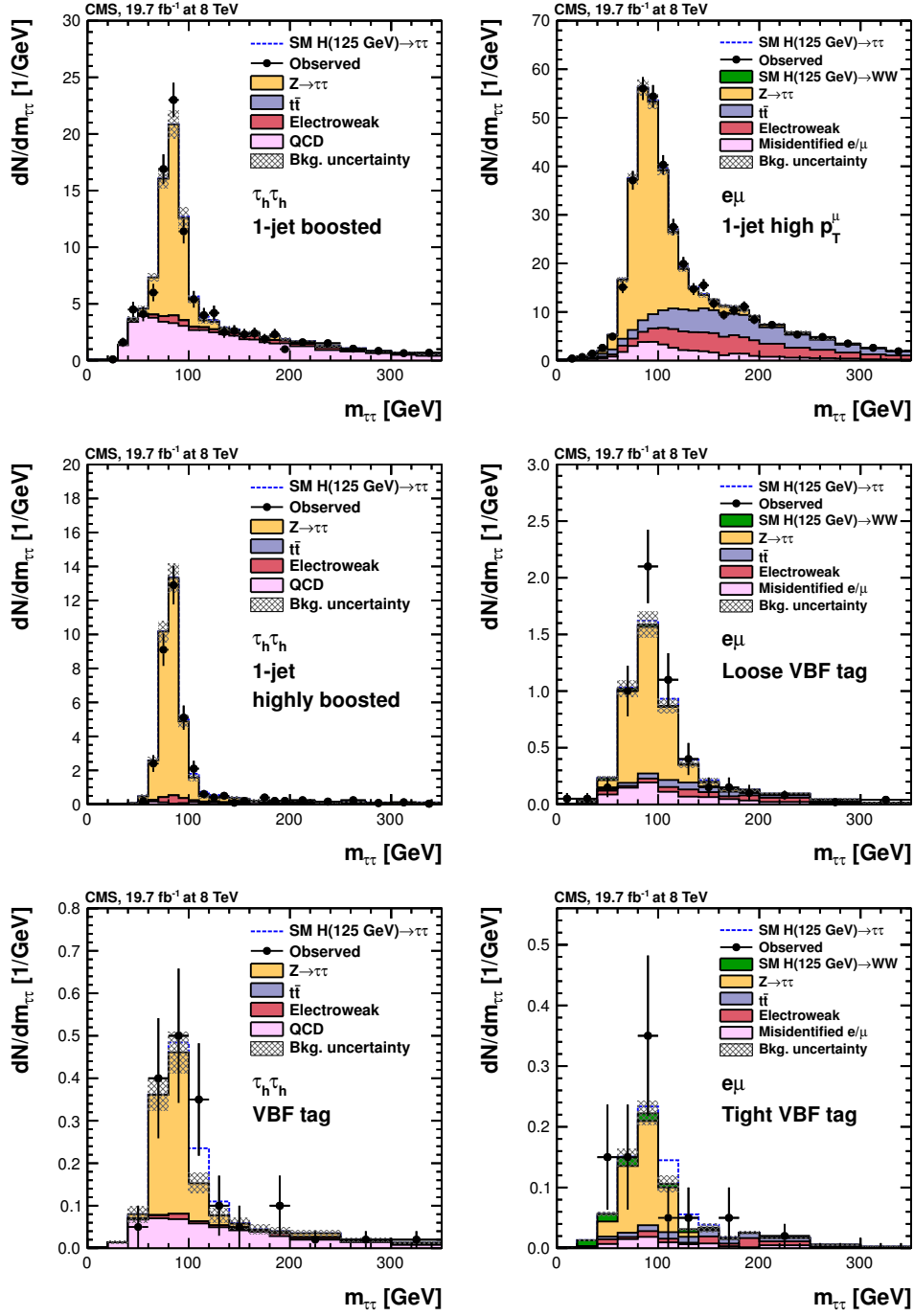


Figure 9. Observed and predicted $m_{\tau\tau}$ distributions in the 8 TeV $\tau_h\tau_h$ (left) channel for the 1-jet boosted (top), 1-jet highly-boosted (middle), and VBF-tagged (bottom) categories, and in the 8 TeV $e\mu$ (right) channel for the 1-jet high- p_T^μ (top), loose VBF tag (middle) and tight VBF tag (bottom) categories. The normalization of the predicted background distributions corresponds to the result of the global fit. The signal distribution, on the other hand, is normalized to the SM prediction. In the $e\mu$ channel, the expected contribution from $H \rightarrow WW$ decays is shown separately. The signal and background histograms are stacked.

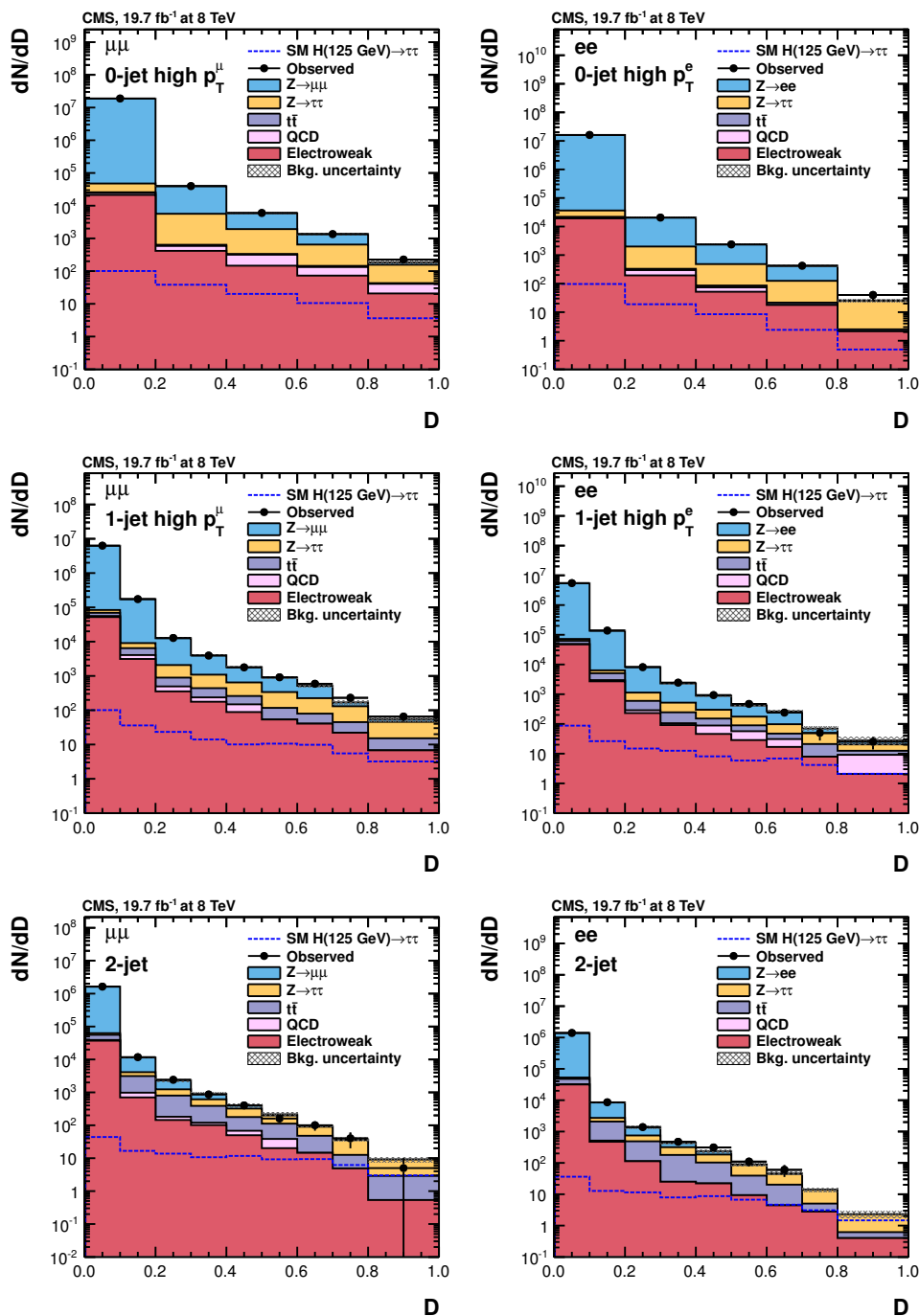


Figure 10. Observed and predicted distributions for the final discriminator D in the 8 TeV $\mu\mu$ (left) and ee (right) channels, and for the 0-jet high- p_T^l (top), 1-jet high- p_T^l (middle), and 2-jet (bottom) categories. The normalization of the predicted background distributions corresponds to the result of the global fit. The signal distribution, on the other hand, is normalized to the SM prediction. The open signal histogram is shown superimposed to the background histograms, which are stacked.

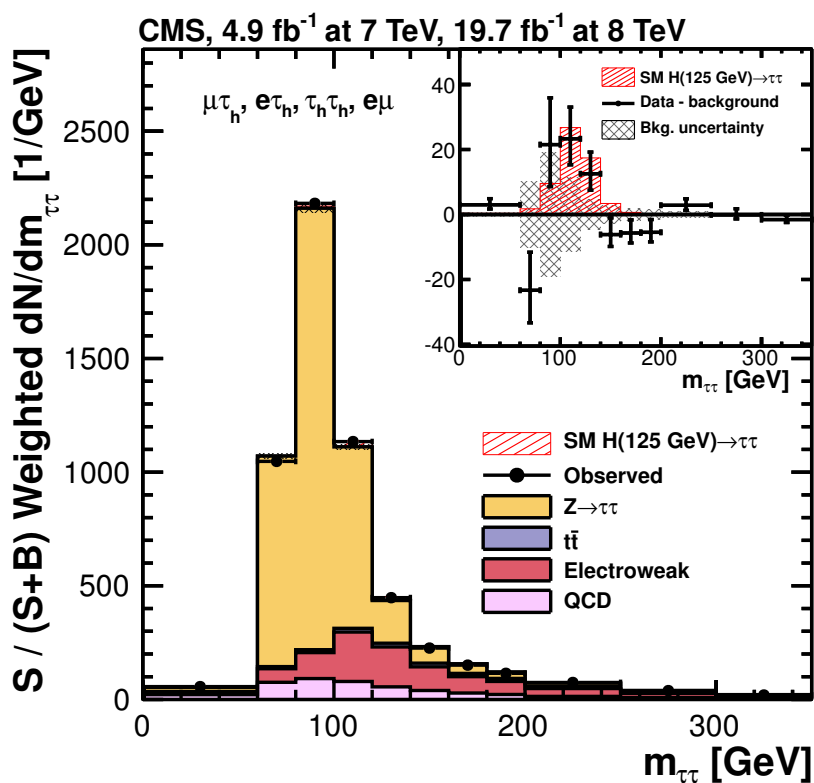


Figure 11. Combined observed and predicted $m_{\tau\tau}$ distributions for the $\mu\tau_h$, $e\tau_h$, $\tau_h\tau_h$, and $e\mu$ channels. The normalization of the predicted background distributions corresponds to the result of the global fit. The signal distribution, on the other hand, is normalized to the SM prediction ($\mu = 1$). The distributions obtained in each category of each channel are weighted by the ratio between the expected signal and signal-plus-background yields in the category, obtained in the central $m_{\tau\tau}$ interval containing 68% of the signal events. The inset shows the corresponding difference between the observed data and expected background distributions, together with the signal distribution for a SM Higgs boson at $m_H = 125$ GeV. The distribution from SM Higgs boson events in the WW decay channel does not significantly contribute to this plot.

The m_{vis} or $m_{\tau\tau}$ distributions obtained for the 8 TeV dataset in the $\ell + L\tau_h$ and $\ell\ell + LL'$ channels are shown in figure 13. Because of the small number of expected events in each event category, different event categories are combined. The complete set of distributions is presented in appendix A, and the event yields for the individual event categories are given in table 6 in appendix B.

The following results include all decay channels considered. Figure 14 left shows the observed 95% CL upper limit obtained using the modified frequentist construction CL_s [90, 91] together with the expected limit obtained for the background-only hypothesis for Higgs boson mass hypotheses ranging from 90 to 145 GeV. The background-only hypothesis includes the expected contribution from $H \rightarrow WW$ decays for $m_H = 125$ GeV. The difference between evaluating this contribution at $m_H = 125$ GeV or at the corresponding m_H value for $m_H \neq 125$ GeV is less than 5%. An excess is visible in the observed limit with respect to

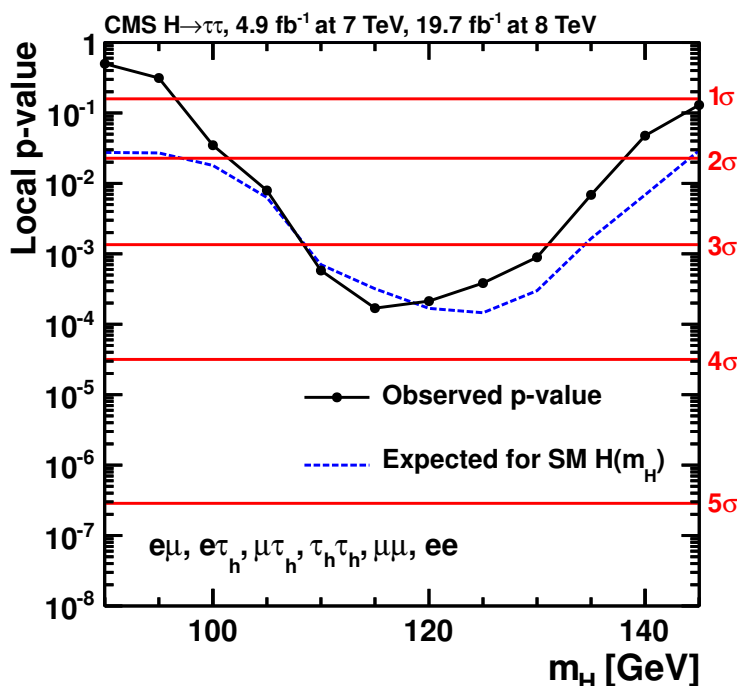


Figure 12. Local p -value and significance in number of standard deviations as a function of the SM Higgs boson mass hypothesis for the LL' channels. The observation (solid line) is compared to the expectation (dashed line) for a SM Higgs boson with mass m_H . The background-only hypothesis includes the $pp \rightarrow H(125 \text{ GeV}) \rightarrow WW$ process for every value of m_H .

the limit expected for the background-only hypothesis. The observed limit is compatible with the expected limit obtained in the signal-plus-background hypothesis for a SM Higgs boson with $m_H = 125 \text{ GeV}$ (figure 14 right). The excess is quantified in figure 15 which shows the local p -value as a function of m_H . For $m_H = 125 \text{ GeV}$, the expected p -value is smallest, corresponding to a significance of 3.7 standard deviations. The expected p -value is slightly smaller when including the $\ell + L\tau_h$ and $\ell\ell + LL'$ channels. The observed p -value is minimal for $m_H = 120 \text{ GeV}$ with a significance of 3.3 standard deviations. The observed significance is larger than three standard deviations for m_H between 115 and 130 GeV, and is equal to 3.2 standard deviations for $m_H = 125 \text{ GeV}$.

The best-fit value for μ , combining all channels, is $\hat{\mu} = 0.78 \pm 0.27$ at $m_H = 125 \text{ GeV}$. Figure 16 shows the results of the fits performed in each decay channel for all categories, and in each category for all decay channels. These compatibility tests do not constitute measurements of any physical parameter per se, but rather show the consistency of the various observations with the expectation for a SM Higgs boson with $m_H = 125 \text{ GeV}$. The uncertainties of the individual μ values in the 1-jet and 2-jet (VBF-tagged) categories are of similar size, showing that both contribute about equally to the sensitivity of the analysis. The fraction of signal events from VBF production in the 1-jet categories and of signal events produced via gluon-gluon fusion in the 2-jet (VBF-tagged) categories are each of the order of 20 to 30%; hence, it is not possible to fully disentangle the two production modes.

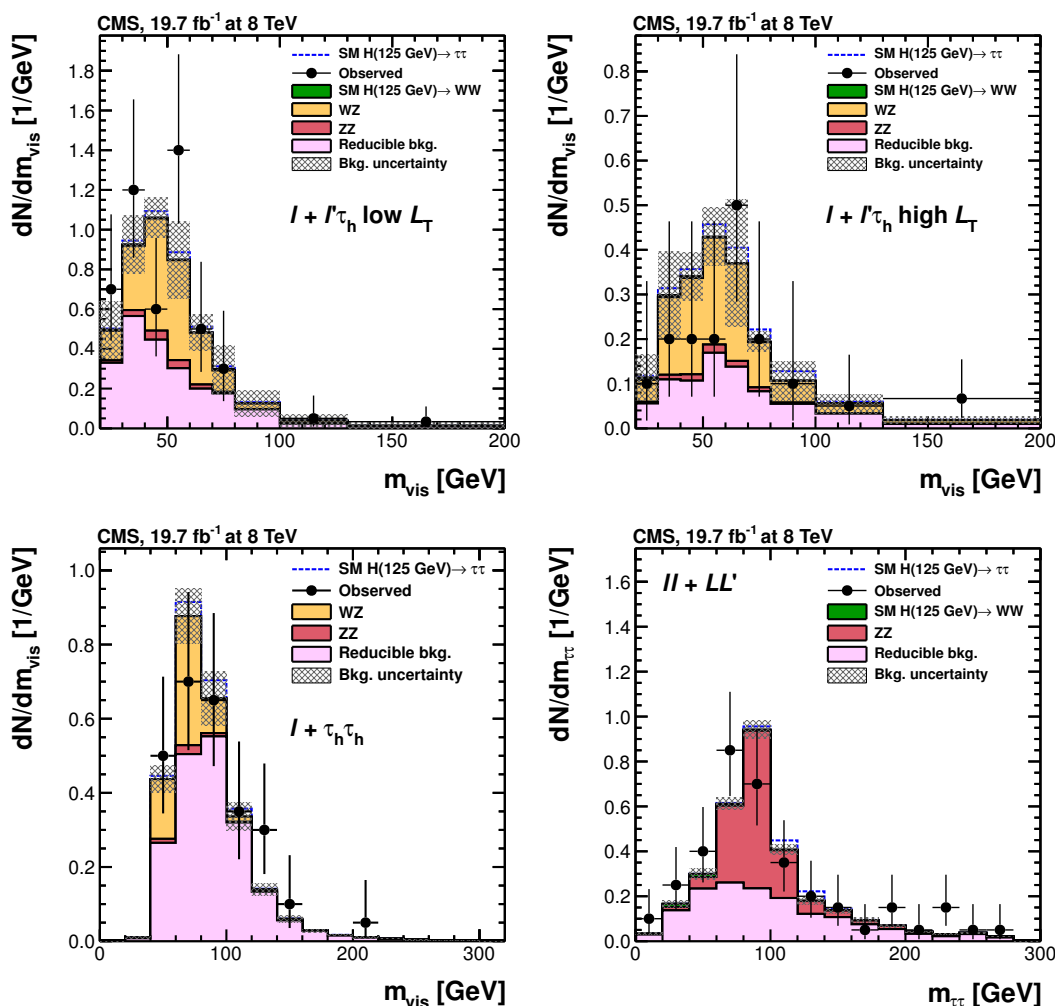


Figure 13. Observed and predicted m_{vis} distributions in the $\ell + \ell' \tau_h$ channel in the low- L_T (top left) and high- L_T (top right) categories, each for the 8 TeV dataset, and in the $\ell + \tau_h \tau_h$ channel (bottom left); observed and predicted $m_{\tau\tau}$ distributions in the $\ell\ell + LL'$ channel (bottom right). The normalization of the predicted background distributions corresponds to the result of the global fit. The signal distribution, on the other hand, is normalized to the SM prediction ($\mu = 1$). The signal and background histograms are stacked.

The combined distribution of the decimal logarithm $\log(S/(S + B))$ obtained in each bin of the final discriminating variables for all event categories and channels is shown in figure 17. Here, S denotes the expected signal yield for a SM Higgs boson with $m_H = 125 \text{ GeV}$ ($\mu = 1$) and B denotes the expected background yield in a given bin. The plot illustrates the contribution from the different event categories that are sensitive to the different Higgs boson production mechanisms. In addition, it provides a visualization of the observed excess of data events over the background expectation in the region of high $S/(S + B)$.

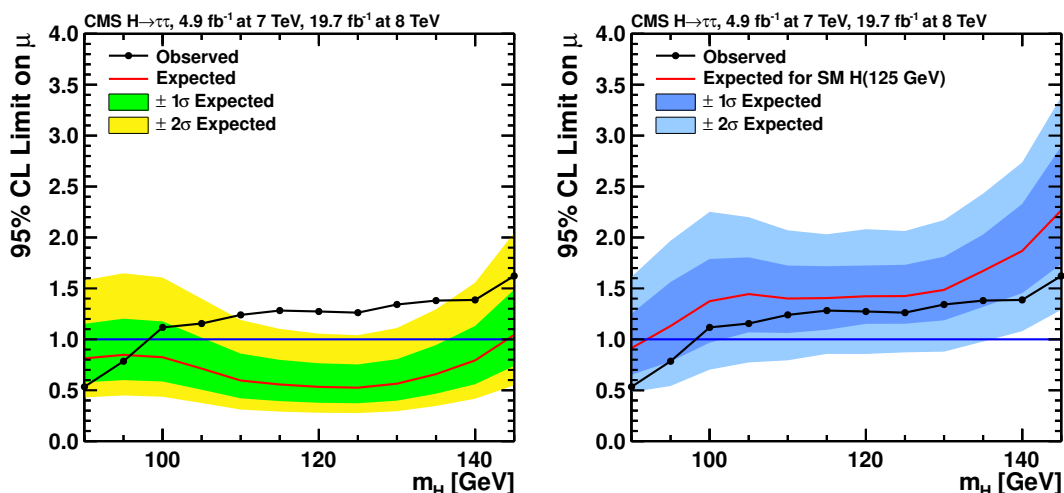


Figure 14. Combined observed 95% CL upper limit on the signal strength parameter μ , together with the expected limit obtained in the background-only hypothesis (left), and the signal-plus-background hypothesis for a SM Higgs boson with $m_H = 125$ GeV (right). The background-only hypothesis includes the $pp \rightarrow H(125 \text{ GeV}) \rightarrow WW$ process for every value of m_H . The bands show the expected one- and two-standard-deviation probability intervals around the expected limit.

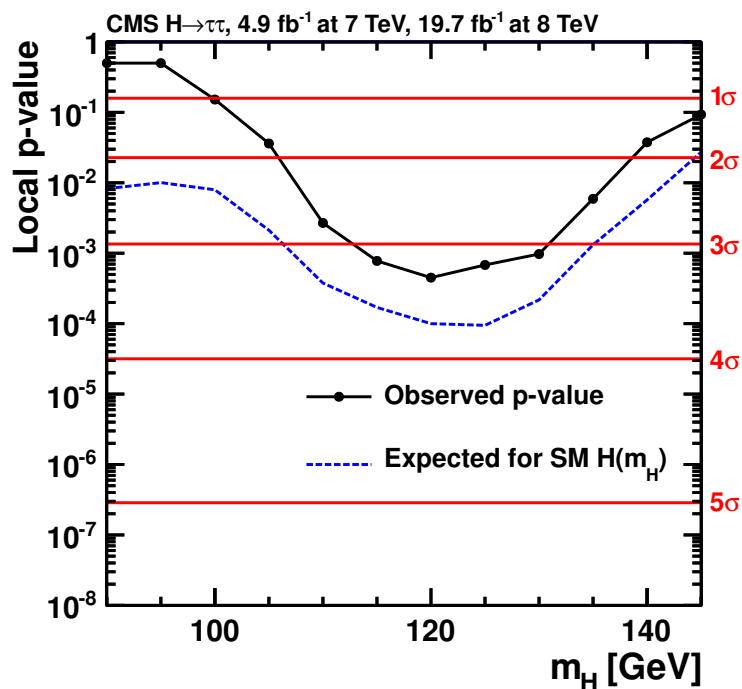


Figure 15. Local p -value and significance in number of standard deviations as a function of the SM Higgs boson mass hypothesis for the combination of all decay channels. The observation (solid line) is compared to the expectation (dashed line) for a SM Higgs boson with mass m_H . The background-only hypothesis includes the $pp \rightarrow H(125 \text{ GeV}) \rightarrow WW$ process for every value of m_H .

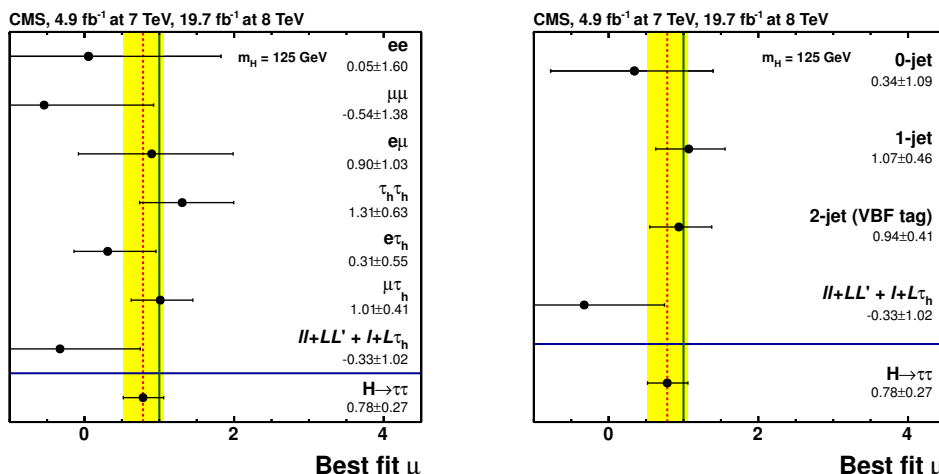


Figure 16. Best-fit signal strength values, for independent channels (left) and categories (right), for $m_H = 125$ GeV. The combined value for the $H \rightarrow \tau\tau$ analysis in both plots corresponds to $\hat{\mu} = 0.78 \pm 0.27$, obtained in the global fit combining all categories of all channels. The dashed line corresponds to the best-fit μ value. The contribution from the $pp \rightarrow H(125 \text{ GeV}) \rightarrow WW$ process is treated as background normalized to the SM expectation.

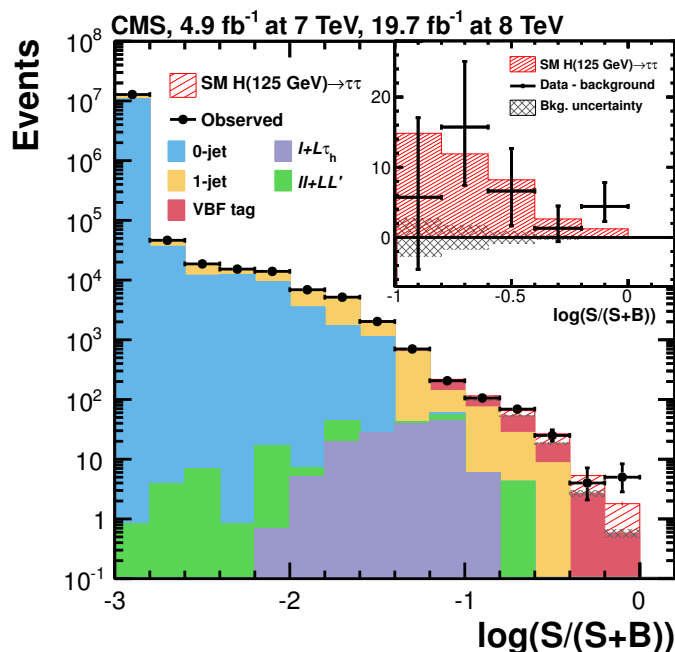


Figure 17. Combined observed and predicted distributions of the decimal logarithm $\log(S/(S+B))$ in each bin of the final $m_{\tau\tau}$, m_{vis} , or discriminator distributions obtained in all event categories and decay channels, with $S/(S+B)$ denoting the ratio of the predicted signal and signal-plus-background event yields in each bin. The normalization of the predicted background distributions corresponds to the result of the global fit. The signal distribution, on the other hand, is normalized to the SM prediction ($\mu = 1$). The inset shows the corresponding difference between the observed data and expected background distributions, together with the signal distribution for a SM Higgs boson at $m_H = 125$ GeV. The distribution from SM Higgs boson events in the WW decay channel does not significantly contribute to this plot.

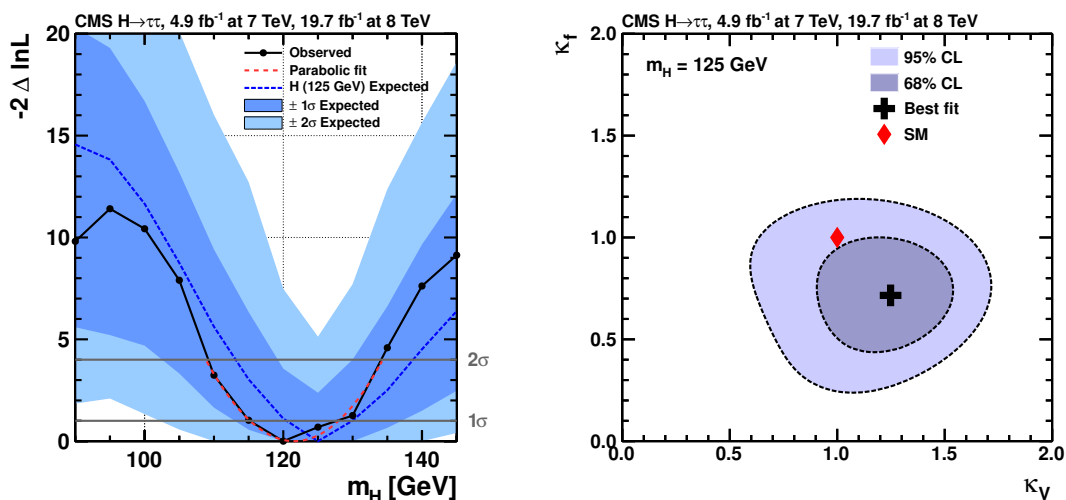


Figure 18. Scan of the negative log-likelihood difference, $-2\Delta \ln \mathcal{L}$, as a function of m_H (left) and as a function of κ_V and κ_f (right). For each point, all nuisance parameters are profiled. For the likelihood scan as a function of m_H , the background-only hypothesis includes the $pp \rightarrow H(125 \text{ GeV}) \rightarrow WW$ process for every value of m_H . The observation (solid line) is compared to the expectation (dashed line) for a SM Higgs boson with mass $m_H = 125 \text{ GeV}$. For the likelihood scan as a function of κ_V and κ_f , the $H \rightarrow WW$ contribution is treated as a signal process.

Figure 18 left presents a scan of the negative log-likelihood difference, $-2\Delta \ln \mathcal{L}$, as a function of m_H . For each point in the parameter space, all nuisance parameters and the μ parameter are profiled. The background-only hypothesis includes the contribution from the $pp \rightarrow H(125 \text{ GeV}) \rightarrow WW$ process for every value of m_H . The difference between evaluating this additional background at $m_H = 125 \text{ GeV}$ or at the corresponding m_H value for $m_H \neq 125 \text{ GeV}$ is small. At the mass value corresponding to the minimum of the mass scan, the combined statistical and systematic uncertainties from the likelihood scan amount to 6 GeV. Additional contributions to the overall uncertainty of the mass measurement arise due to uncertainties in the absolute energy scale and its variation with p_T of 1 to 2% for τ_h candidates, electrons, muons, and the E_T^{miss} , summing up to an uncertainty of 4 GeV. Given the coarse m_H granularity, a parabolic fit is performed to $-2\Delta \ln \mathcal{L}$ values below 4. The combined measured mass of the Higgs boson is $m_H = 122 \pm 7 \text{ GeV}$.

Figure 18 right shows a likelihood scan in the two-dimensional (κ_V, κ_f) parameter space for $m_H = 125 \text{ GeV}$. The κ_V and κ_f parameters quantify the ratio between the measured and the SM value for the coupling of the Higgs boson to vector bosons and fermions, respectively [49]. To consistently measure deviations of the fermionic and the bosonic couplings of the Higgs boson, the $H \rightarrow WW$ contribution is considered as a signal process in this likelihood scan. For the VBF production of a Higgs boson that decays to a WW pair, the bosonic coupling enters both in the production and in the decay, thus providing sensitivity to the bosonic coupling despite the small expected event rates. All nuisance parameters are profiled for each point in the parameter space. The observed likelihood contour is consistent with the SM expectation of $\kappa_V = \kappa_f = 1$.

10 Summary

We report a search for the standard model Higgs boson decaying into a pair of τ leptons. The search is based on the full proton-proton collision sample recorded by CMS in 2011 and 2012, corresponding to an integrated luminosity of 4.9 fb^{-1} at a centre-of-mass energy of 7 TeV and 19.7 fb^{-1} at 8 TeV. The analysis is performed in six channels corresponding to the final states $\mu\tau_h$, $e\tau_h$, $\tau_h\tau_h$, $e\mu$, $\mu\mu$, and ee . The gluon-gluon fusion and vector-boson fusion production of a Higgs boson are probed in the one-jet and two-jet final states, respectively, whereas the production of a Higgs boson in association with a W or Z boson decaying leptonically is targeted by requiring additional electrons or muons in the final state. An excess of events over the background-only hypothesis is observed with a local significance in excess of 3 standard deviations for Higgs boson mass hypotheses between $m_H = 115$ and 130 GeV, and equal to 3.2 standard deviations at $m_H = 125$ GeV, to be compared to an expected significance of 3.7 standard deviations. The best fit of the observed $H \rightarrow \tau\tau$ signal cross section times branching fraction for $m_H = 125$ GeV is 0.78 ± 0.27 times the standard model expectation. Assuming that this excess corresponds to a Higgs boson decaying to $\tau\tau$, its mass is measured to be $m_H = 122 \pm 7$ GeV. These results constitute evidence for the coupling between the τ lepton and the 125 GeV Higgs boson discovered in 2012 by the ATLAS and CMS Collaborations.

Acknowledgments

We congratulate our colleagues in the CERN accelerator departments for the excellent performance of the LHC and thank the technical and administrative staffs at CERN and at other CMS institutes for their contributions to the success of the CMS effort. In addition, we gratefully acknowledge the computing centres and personnel of the Worldwide LHC Computing Grid for delivering so effectively the computing infrastructure essential to our analyses. Finally, we acknowledge the enduring support for the construction and operation of the LHC and the CMS detector provided by the following funding agencies: the Austrian Federal Ministry of Science and Research and the Austrian Science Fund; the Belgian Fonds de la Recherche Scientifique, and Fonds voor Wetenschappelijk Onderzoek; the Brazilian Funding Agencies (CNPq, CAPES, FAPERJ, and FAPESP); the Bulgarian Ministry of Education and Science; CERN; the Chinese Academy of Sciences, Ministry of Science and Technology, and National Natural Science Foundation of China; the Colombian Funding Agency (COLCIENCIAS); the Croatian Ministry of Science, Education and Sport, and the Croatian Science Foundation; the Research Promotion Foundation, Cyprus; the Ministry of Education and Research, Recurrent financing contract SF0690030s09 and European Regional Development Fund, Estonia; the Academy of Finland, Finnish Ministry of Education and Culture, and Helsinki Institute of Physics; the Institut National de Physique Nucléaire et de Physique des Particules / CNRS, and Commissariat à l'Énergie Atomique et aux Énergies Alternatives / CEA, France; the Bundesministerium für Bildung und Forschung, Deutsche Forschungsgemeinschaft, and Helmholtz-Gemeinschaft Deutscher Forschungszentren, Germany; the General Secretariat for Research and Technology, Greece;

the National Scientific Research Foundation, and National Innovation Office, Hungary; the Department of Atomic Energy and the Department of Science and Technology, India; the Institute for Studies in Theoretical Physics and Mathematics, Iran; the Science Foundation, Ireland; the Istituto Nazionale di Fisica Nucleare, Italy; the Korean Ministry of Education, Science and Technology and the World Class University program of NRF, Republic of Korea; the Lithuanian Academy of Sciences; the Mexican Funding Agencies (CINVESTAV, CONACYT, SEP, and UASLP-FAI); the Ministry of Business, Innovation and Employment, New Zealand; the Pakistan Atomic Energy Commission; the Ministry of Science and Higher Education and the National Science Centre, Poland; the Fundação para a Ciência e a Tecnologia, Portugal; JINR, Dubna; the Ministry of Education and Science of the Russian Federation, the Federal Agency of Atomic Energy of the Russian Federation, Russian Academy of Sciences, and the Russian Foundation for Basic Research; the Ministry of Education, Science and Technological Development of Serbia; the Secretaría de Estado de Investigación, Desarrollo e Innovación and Programa Consolider-Ingenio 2010, Spain; the Swiss Funding Agencies (ETH Board, ETH Zurich, PSI, SNF, UniZH, Canton Zurich, and SER); the National Science Council, Taipei; the Thailand Center of Excellence in Physics, the Institute for the Promotion of Teaching Science and Technology of Thailand, Special Task Force for Activating Research and the National Science and Technology Development Agency of Thailand; the Scientific and Technical Research Council of Turkey, and Turkish Atomic Energy Authority; the Science and Technology Facilities Council, UK; the US Department of Energy, and the US National Science Foundation.

Individuals have received support from the Marie-Curie programme and the European Research Council and EPLANET (European Union); the Leventis Foundation; the A. P. Sloan Foundation; the Alexander von Humboldt Foundation; the Belgian Federal Science Policy Office; the Fonds pour la Formation à la Recherche dans l'Industrie et dans l'Agriculture (FRIA-Belgium); the Agentschap voor Innovatie door Wetenschap en Technologie (IWT-Belgium); the Ministry of Education, Youth and Sports (MEYS) of Czech Republic; the Council of Science and Industrial Research, India; the Compagnia di San Paolo (Torino); the HOMING PLUS programme of Foundation for Polish Science, cofinanced by EU, Regional Development Fund; and the Thalís and Aristeia programmes cofinanced by EU-ESF and the Greek NSRF.

A Post-fit distributions

The $m_{\tau\tau}$ distributions obtained with the 7 and 8 TeV datasets are shown respectively in figures 19 and 20 for the $\mu\tau_h$ channel, in figures 21 and 22 for the $e\tau_h$ channel, and in figures 23 and 24 for the $e\mu$ channel. The distributions of the final discriminator D obtained with the 7 and 8 TeV datasets are shown respectively in figures 25 and 26 for the $\mu\mu$ channel, and in figures 27 and 28 for the ee channel. The figures are arranged according to the category layout of figure 4.

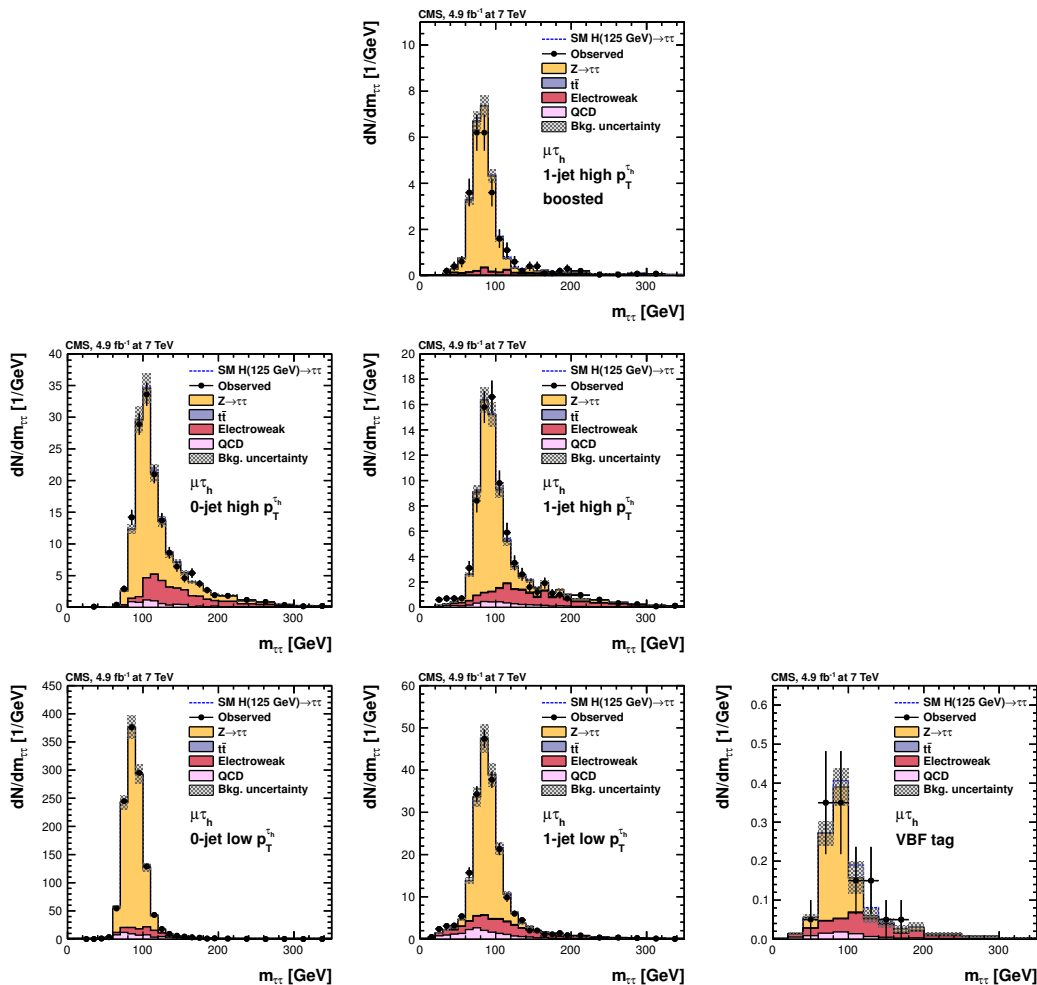


Figure 19. Observed and predicted $m_{\tau\tau}$ distributions in the $\mu\tau_h$ channel, for all categories used in the 7 TeV data analysis. The normalization of the predicted background distributions corresponds to the result of the global fit. The signal distribution, on the other hand, is normalized to the SM prediction. The signal and background histograms are stacked.

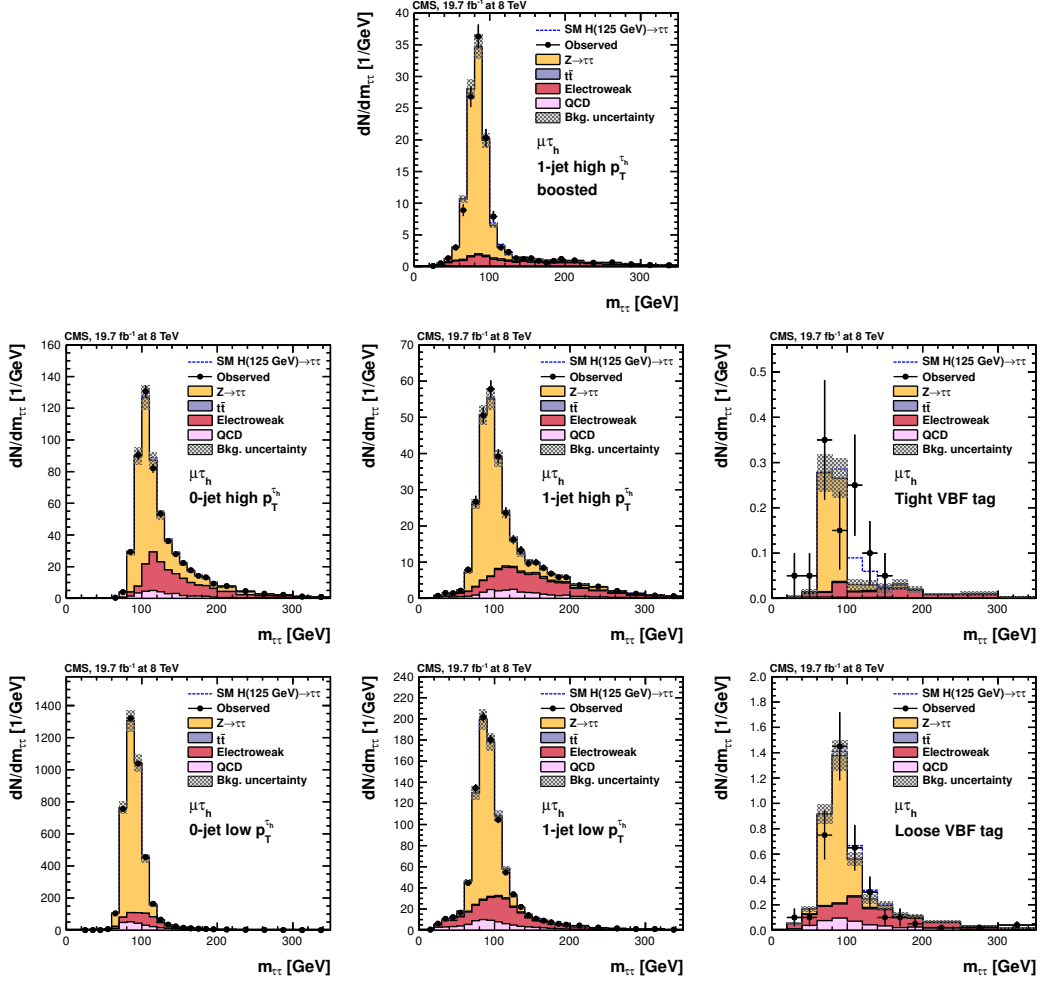


Figure 20. Observed and predicted $m_{\tau\tau}$ distributions in the $\mu\tau_h$ channel, for all categories used in the 8 TeV data analysis. The normalization of the predicted background distributions corresponds to the result of the global fit. The signal distribution, on the other hand, is normalized to the SM prediction. The signal and background histograms are stacked.

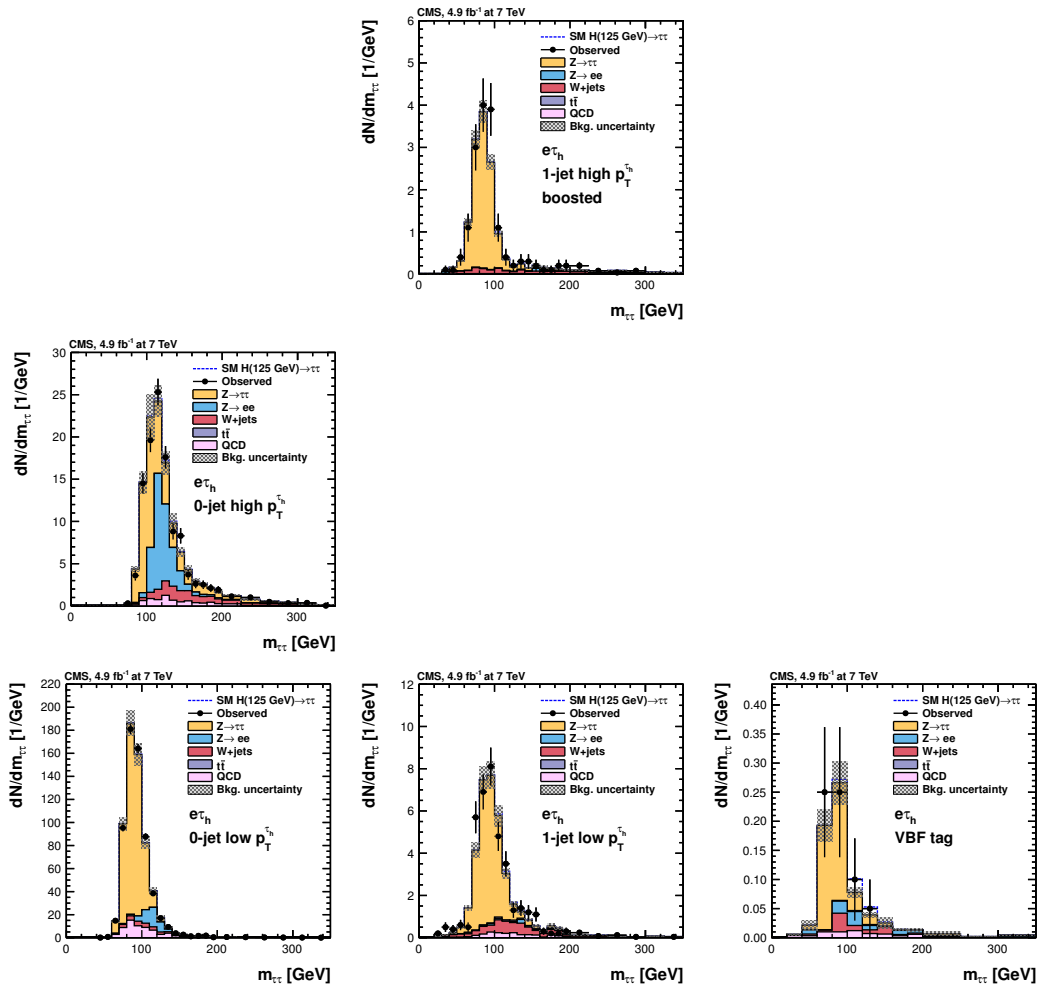


Figure 21. Observed and predicted $m_{\tau\tau}$ distributions in the $e\tau_h$ channel, for all categories used in the 7 TeV data analysis. The normalization of the predicted background distributions corresponds to the result of the global fit. The signal distribution, on the other hand, is normalized to the SM prediction. The signal and background histograms are stacked.

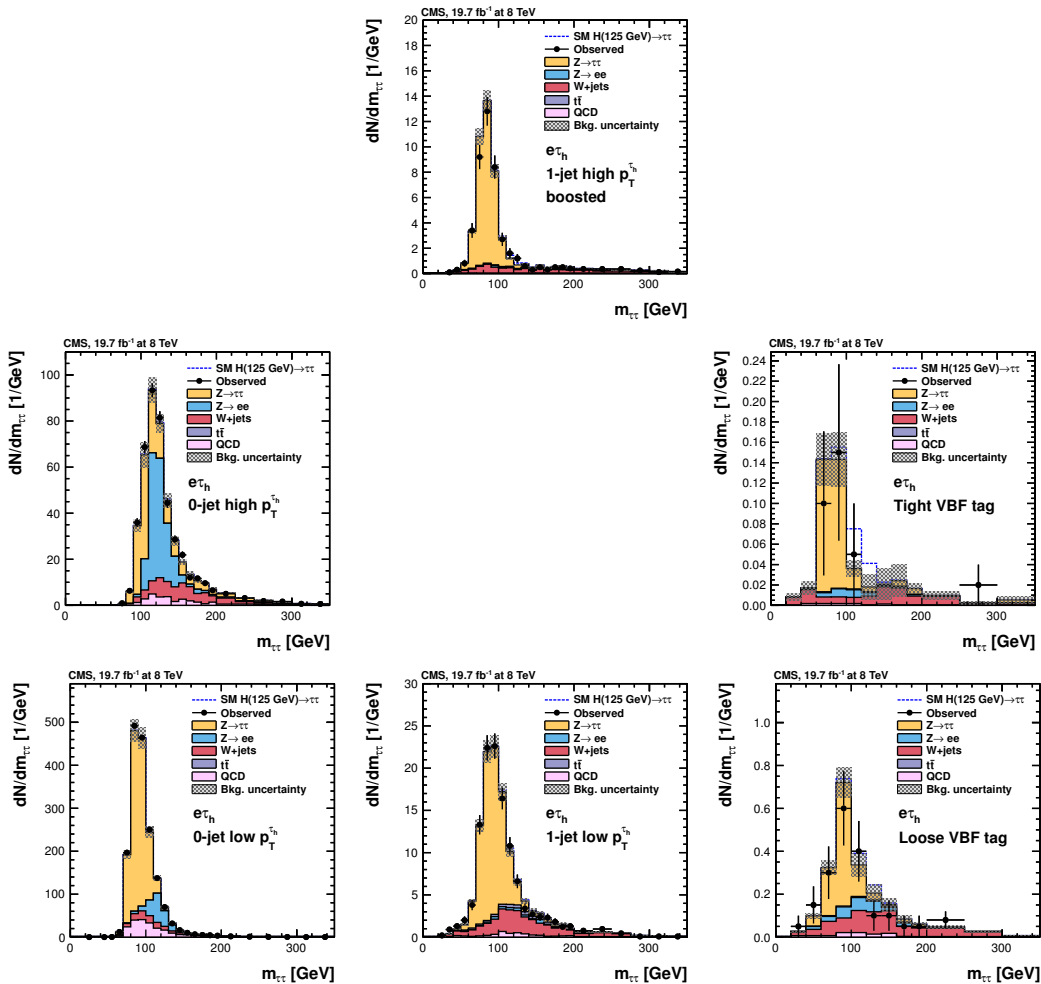


Figure 22. Observed and predicted $m_{\tau\tau}$ distributions in the $e\tau_h$ channel, for all categories used in the 8 TeV data analysis. The normalization of the predicted background distributions corresponds to the result of the global fit. The signal distribution, on the other hand, is normalized to the SM prediction. The signal and background histograms are stacked.

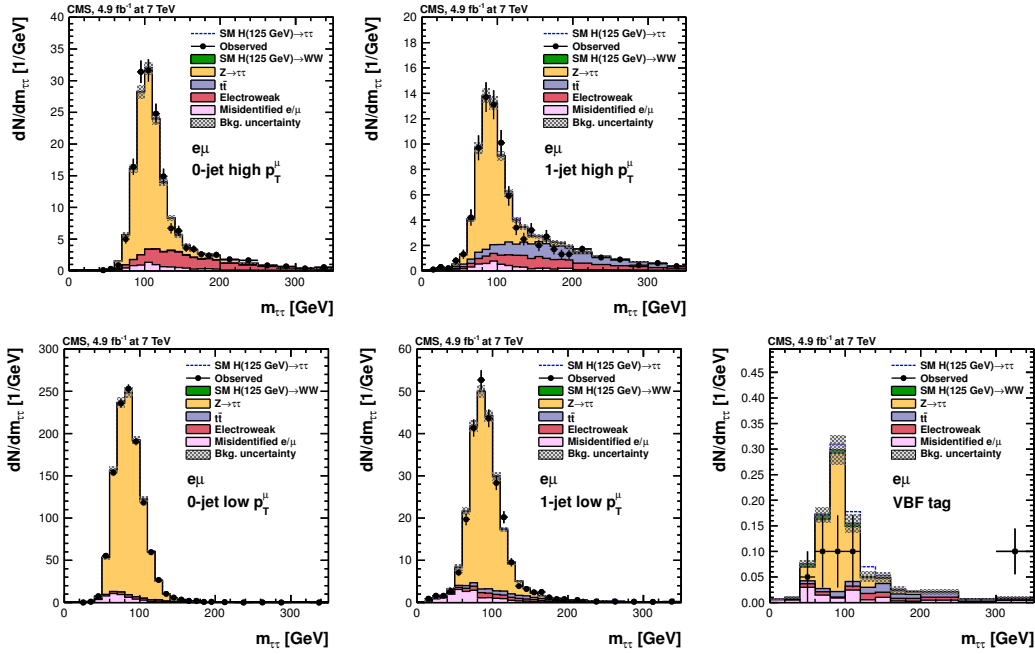


Figure 23. Observed and predicted $m_{\tau\tau}$ distributions in the $e\mu$ channel, for all categories used in the 7 TeV data analysis. The normalization of the predicted background distributions corresponds to the result of the global fit. The signal distribution, on the other hand, is normalized to the SM prediction. The signal and background histograms are stacked.

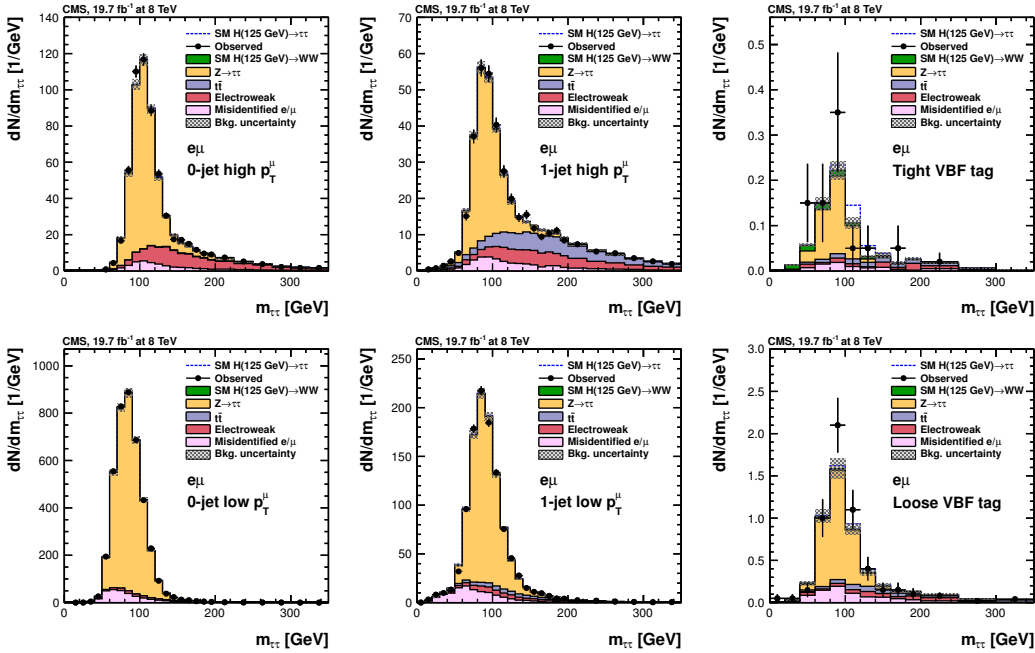


Figure 24. Observed and predicted $m_{\tau\tau}$ distributions in the $e\mu$ channel, for all categories used in the 8 TeV data analysis. The normalization of the predicted background distributions corresponds to the result of the global fit. The signal distribution, on the other hand, is normalized to the SM prediction. The signal and background histograms are stacked.

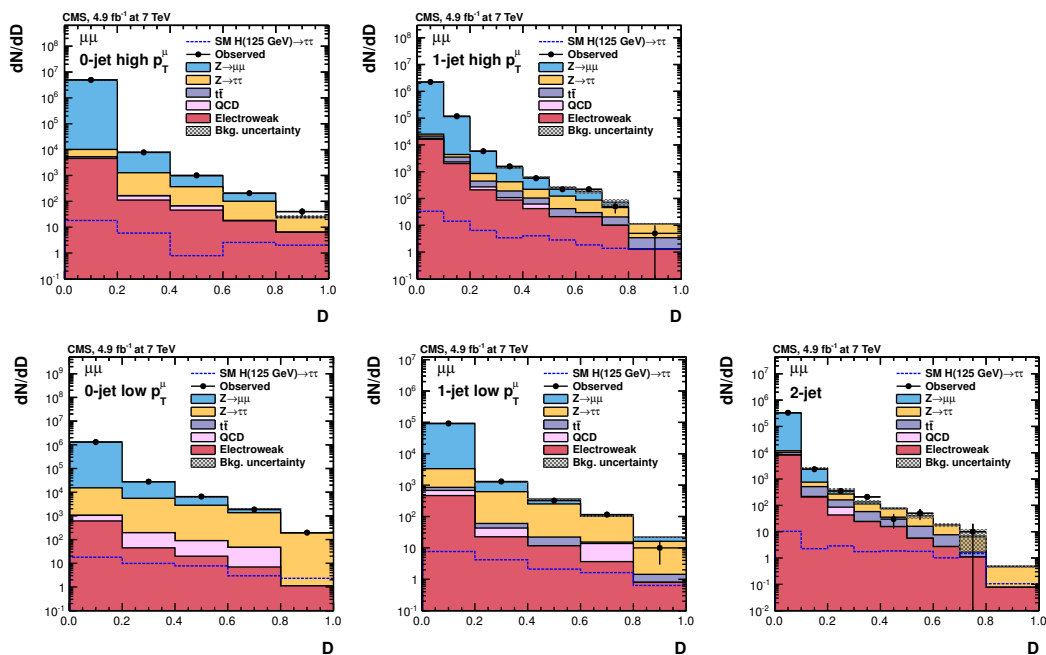


Figure 25. Observed and predicted D distributions in the $\mu\mu$ channel, for all categories used in the 7 TeV data analysis. The normalization of the predicted background distributions corresponds to the result of the global fit. The signal distribution, on the other hand, is normalized to the SM prediction. The open signal histogram is shown superimposed to the background histograms, which are stacked.

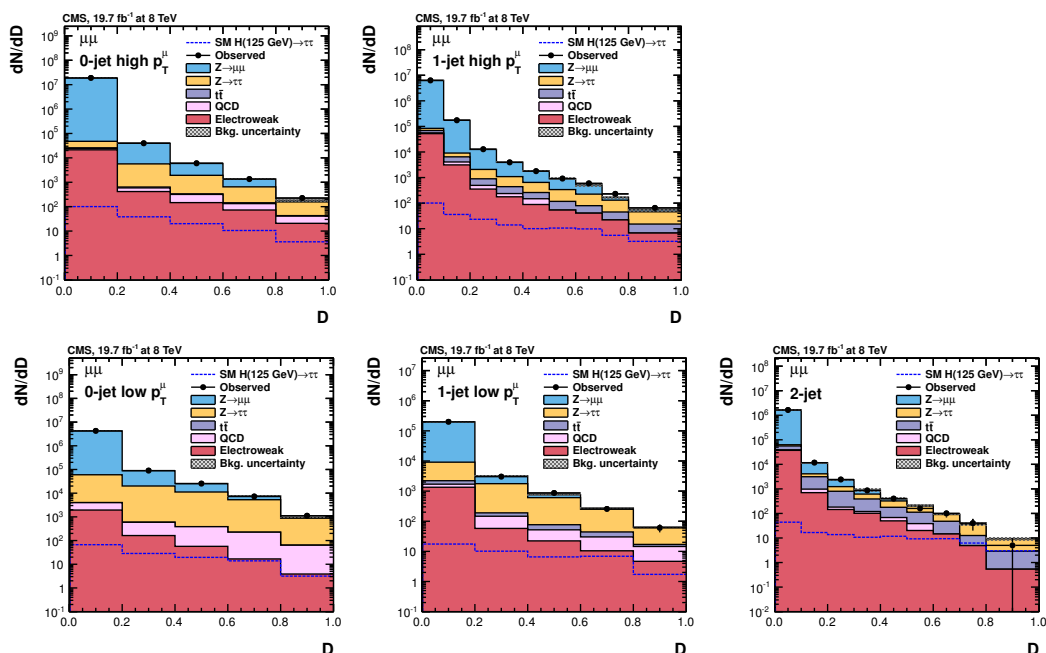


Figure 26. Observed and predicted D distributions in the $\mu\mu$ channel, for all categories used in the 8 TeV data analysis. The normalization of the predicted background distributions corresponds to the result of the global fit. The signal distribution, on the other hand, is normalized to the SM prediction. The open signal histogram is shown superimposed to the background histograms, which are stacked.

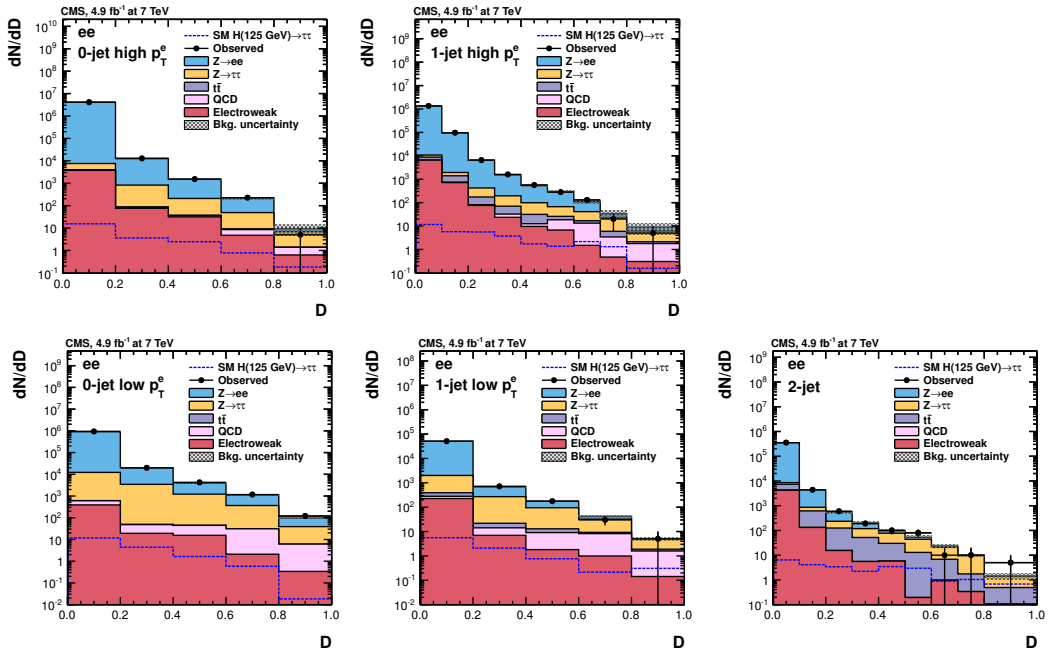


Figure 27. Observed and predicted D distributions in the ee channel, for all categories used in the 7 TeV data analysis. The normalization of the predicted background distributions corresponds to the result of the global fit. The signal distribution, on the other hand, is normalized to the SM prediction. The open signal histogram is shown superimposed to the background histograms, which are stacked.

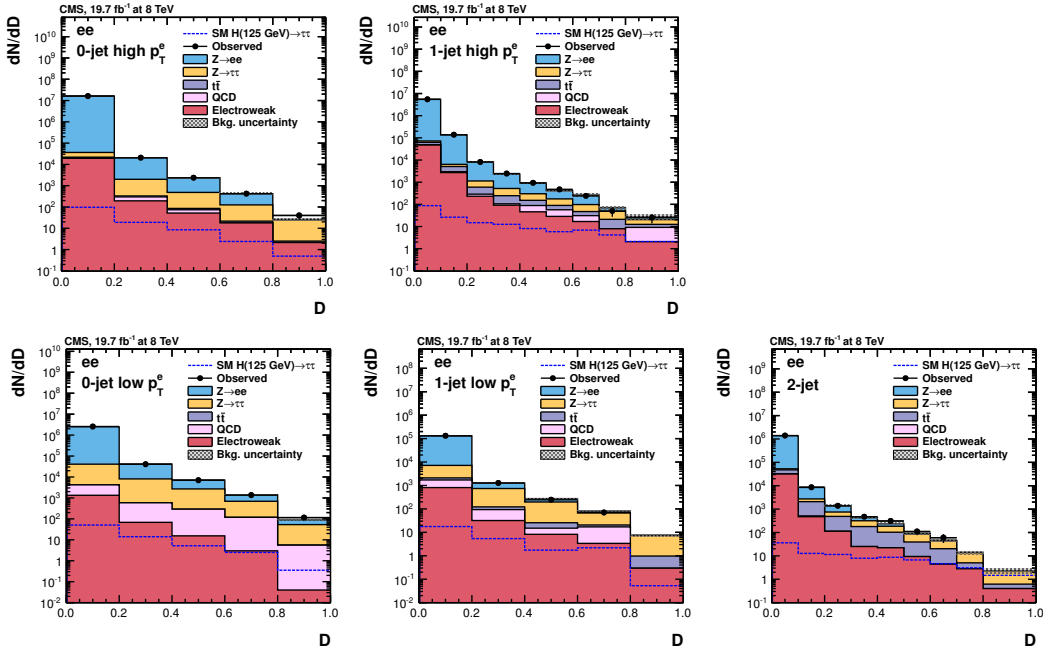


Figure 28. Observed and predicted D distributions in the ee channel, for all categories used in the 8 TeV data analysis. The normalization of the predicted background distributions corresponds to the result of the global fit. The signal distribution, on the other hand, is normalized to the SM prediction. The open signal histogram is shown superimposed to the background histograms, which are stacked.

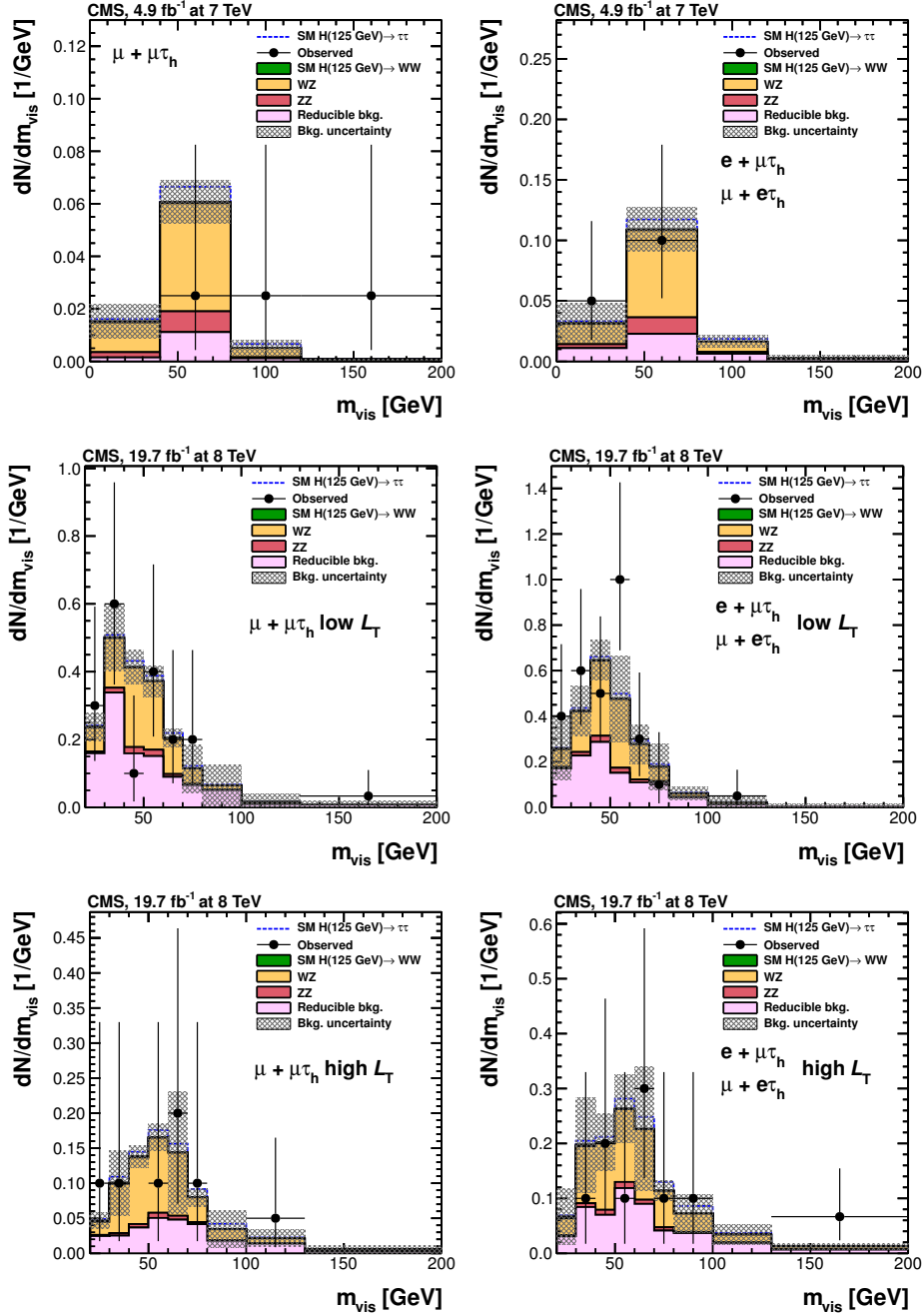


Figure 29. Observed and predicted m_{vis} distributions in the $\mu + \mu\tau_h$ (left) and $e + \mu\tau_h/\mu + e\tau_h$ (right) channels for the 7 TeV data analysis (top) and in the low- L_T (middle) and high- L_T (bottom) categories used in the 8 TeV data analysis. The normalization of the predicted background distributions corresponds to the result of the global fit. The signal distribution, on the other hand, is normalized to the SM prediction. The signal and background histograms are stacked.

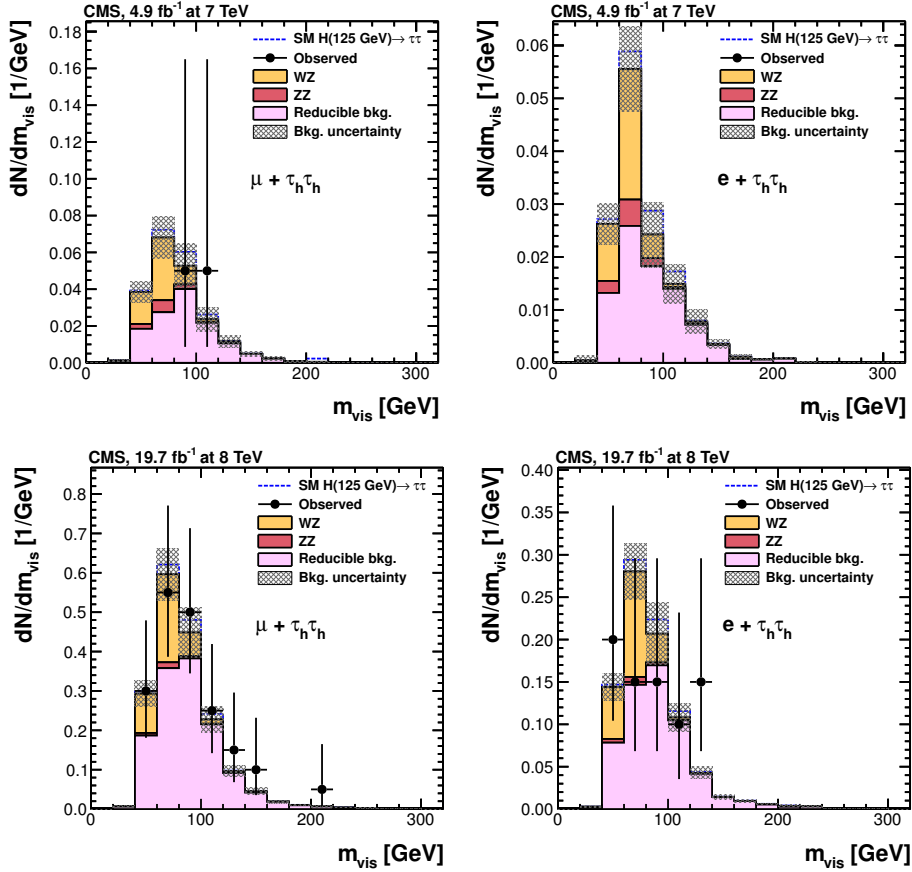


Figure 30. Observed and predicted m_{vis} distributions in the $\mu + \tau_h \tau_h$ (left) and $e + \tau_h \tau_h$ (right) channels for the 7 TeV data analysis (top) and the 8 TeV data analysis (bottom). The normalization of the predicted background distributions corresponds to the result of the global fit. The signal distribution, on the other hand, is normalized to the SM prediction. The signal and background histograms are stacked.

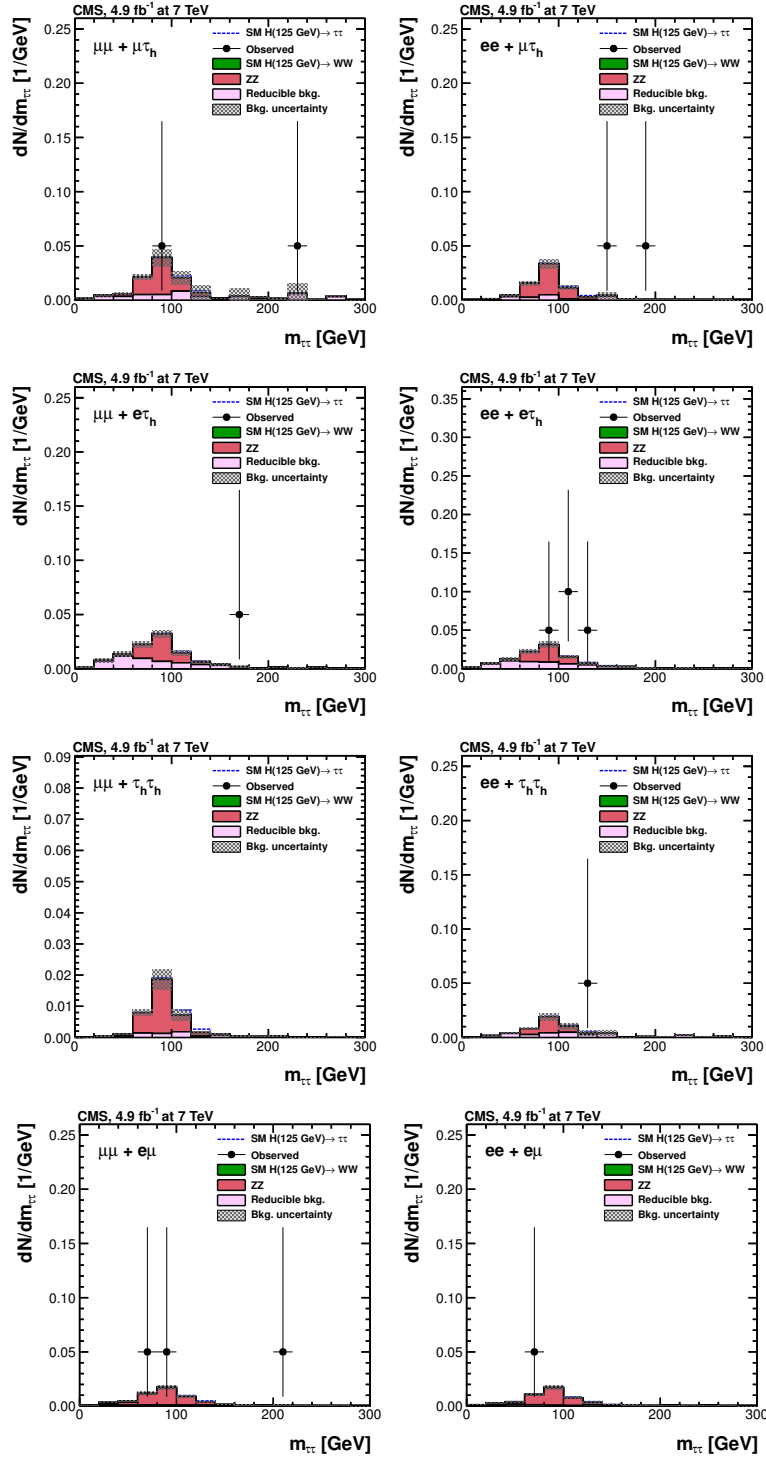


Figure 31. Observed and predicted $m_{\tau\tau}$ distributions for the four different LL' final states of the $ee + LL'$ (left) and $\mu\mu + LL'$ (right) channels for the 7 TeV data analysis. The normalization of the predicted background distributions corresponds to the result of the global fit. The signal distribution, on the other hand, is normalized to the SM prediction. The signal and background histograms are stacked.

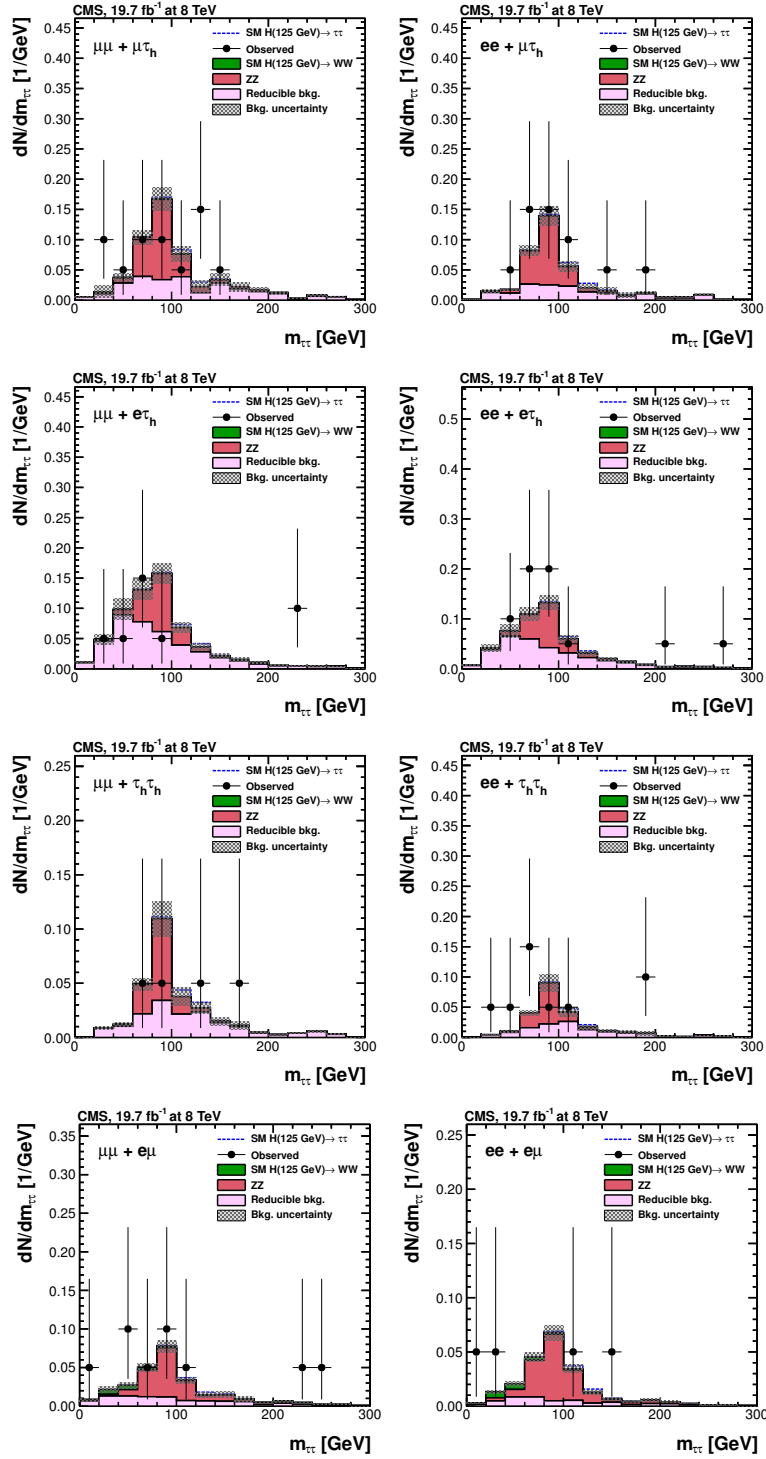


Figure 32. Observed and predicted $m_{\tau\tau}$ distributions for the four different LL' final states of the $ee + LL'$ (left) and $\mu\mu + LL'$ (right) channels for the 8 TeV data analysis. The normalization of the predicted background distributions corresponds to the result of the global fit. The signal distribution, on the other hand, is normalized to the SM prediction. The signal and background histograms are stacked.

B Event yields

Event category	SM Higgs ($m_H = 125$ GeV)				Background	Data	$\frac{S}{S+B}$	RMS (GeV)
	ggH	VBF	VH	Σ signal				
$\mu\tau_h$								
0-jet low- $p_T^{\tau_h}$ 7 TeV	23.1	0.2	0.1	23.5 ± 3.4	11950 ± 590	11959	0.002	17.4
0-jet low- $p_T^{\tau_h}$ 8 TeV	83.0	0.8	0.4	85.0 ± 11.0	40800 ± 1900	40353	0.003	16.3
0-jet high- $p_T^{\tau_h}$ 7 TeV	17.5	0.2	0.2	17.9 ± 2.6	1595 ± 83	1594	0.022	15.1
0-jet high- $p_T^{\tau_h}$ 8 TeV	66.2	0.7	0.6	67.5 ± 9.3	5990 ± 250	5789	0.020	15.2
1-jet low- $p_T^{\tau_h}$ 7 TeV	9.1	1.6	0.8	11.5 ± 1.7	2020 ± 120	2047	0.012	18.8
1-jet low- $p_T^{\tau_h}$ 8 TeV	36.0	6.0	3.0	45.0 ± 6.0	9030 ± 360	9010	0.010	18.6
1-jet high- $p_T^{\tau_h}$ 7 TeV	7.7	1.1	0.6	9.4 ± 1.3	796 ± 39	817	0.033	19.1
1-jet high- $p_T^{\tau_h}$ 8 TeV	29.6	4.3	2.4	36.3 ± 4.6	3180 ± 130	3160	0.029	19.7
1-jet high- $p_T^{\tau_h}$ boosted 7 TeV	2.6	0.8	0.5	3.9 ± 0.6	282 ± 16	269	0.054	17.7
1-jet high- $p_T^{\tau_h}$ boosted 8 TeV	11.5	2.9	2.0	16.5 ± 2.6	1265 ± 62	1253	0.072	17.2
VBF tag 7 TeV	0.2	1.3	–	1.6 ± 0.1	22 ± 2	23	0.14	19.6
Loose VBF tag 8 TeV	1.1	3.4	–	4.5 ± 0.4	81 ± 7	76	0.17	17.0
Tight VBF tag 8 TeV	0.3	2.0	–	2.4 ± 0.2	15 ± 2	20	0.49	18.1
$e\tau_h$								
0-jet low- $p_T^{\tau_h}$ 7 TeV	11.8	0.1	0.1	12.0 ± 1.8	6140 ± 320	6238	0.002	16.4
0-jet low- $p_T^{\tau_h}$ 8 TeV	33.4	0.3	0.2	34.0 ± 4.6	16750 ± 750	17109	0.002	15.8
0-jet high- $p_T^{\tau_h}$ 7 TeV	11.1	0.1	0.1	11.3 ± 1.7	1159 ± 62	1191	0.015	14.3
0-jet high- $p_T^{\tau_h}$ 8 TeV	31.4	0.3	0.3	32.1 ± 4.4	4380 ± 170	4536	0.010	15.4
1-jet low- $p_T^{\tau_h}$ 7 TeV	3.1	0.6	0.3	4.0 ± 0.6	366 ± 25	385	0.029	19.6
1-jet low- $p_T^{\tau_h}$ 8 TeV	9.1	1.8	1.0	11.9 ± 1.6	1200 ± 56	1214	0.025	16.5
1-jet high- $p_T^{\tau_h}$ boosted 7 TeV	1.2	0.3	0.2	1.8 ± 0.3	150 ± 9	167	0.089	15.5
1-jet high- $p_T^{\tau_h}$ boosted 8 TeV	5.1	1.4	0.9	7.5 ± 1.1	497 ± 27	476	0.11	15.5
VBF tag 7 TeV	0.2	0.7	–	0.9 ± 0.1	14 ± 2	13	0.24	15.9
Loose VBF tag 8 TeV	0.6	1.8	–	2.4 ± 0.2	45 ± 4	40	0.14	16.7
Tight VBF tag 8 TeV	0.3	1.3	–	1.6 ± 0.1	9 ± 2	7	0.51	16.2
$\tau_h\tau_h$								
1-jet boosted 8 TeV	7.2	2.1	1.0	10.3 ± 1.7	1133 ± 49	1120	0.054	15.2
1-jet highly-boosted 8 TeV	5.6	1.6	1.2	8.4 ± 1.2	380 ± 23	366	0.14	13.1
VBF tag 8 TeV	0.5	2.4	–	3.0 ± 0.3	29 ± 4	34	0.32	14.3
$e\mu$								
0-jet low- p_T^μ 7 TeV	20.8	0.2	0.2	21.1 ± 3.0	11320 ± 260	11283	0.002	24.4
0-jet low- p_T^μ 8 TeV	70.3	0.7	0.7	71.7 ± 9.6	40410 ± 830	40381	0.002	23.6
0-jet high- p_T^μ 7 TeV	7.5	0.1	0.1	7.8 ± 1.1	1636 ± 55	1676	0.007	22.7
0-jet high- p_T^μ 8 TeV	24.0	0.2	0.5	24.7 ± 3.3	6000 ± 150	6095	0.006	20.7
1-jet low- p_T^μ 7 TeV	9.0	1.6	1.0	11.7 ± 1.5	2475 ± 74	2482	0.009	23.7
1-jet low- p_T^μ 8 TeV	40.6	6.5	3.7	50.8 ± 6.1	10910 ± 250	10926	0.007	23.8
1-jet high- p_T^μ 7 TeV	4.7	1.0	0.6	6.2 ± 0.8	928 ± 37	901	0.015	23.3
1-jet high- p_T^μ 8 TeV	18.0	3.4	2.6	23.9 ± 2.9	4040 ± 110	4050	0.014	23.1
Loose VBF tag 7 TeV	0.2	1.0	–	1.2 ± 0.1	19 ± 1	12	0.13	23.0
Loose VBF tag 8 TeV	0.6	2.6	–	3.3 ± 0.3	99 ± 6	112	0.054	23.5
Tight VBF tag 8 TeV	0.2	1.5	–	1.6 ± 0.1	14 ± 1	17	0.31	17.8

Table 4. Observed and predicted event yields in all event categories of the $\mu\tau_h$, $e\tau_h$, $\tau_h\tau_h$, and $e\mu$ channels in the full $m_{\tau\tau}$ mass range. The event yields of the predicted background distributions correspond to the result of the global fit. The signal yields, on the other hand, are normalized to the standard model prediction. The different signal processes are labelled as ggH (gluon-gluon fusion), VH (production in association with a W or Z boson), and VBF (vector-boson fusion). The $\frac{S}{S+B}$ variable denotes the ratio of the signal and the signal-plus-background yields in the central $m_{\tau\tau}$ range containing 68% of the signal events for $m_H = 125$ GeV. The RMS variable denotes the standard deviation of the $m_{\tau\tau}$ distribution for corresponding signal events.

Event category	SM Higgs ($m_H = 125$ GeV)				Background	Data
	ggH	VBF	VH	Σ signal		
$\mu\mu$						
0-jet low- p_T^μ 7 TeV	8.0	0.1	0.1	8.2 ± 1.2	266200 ± 1400	266365
0-jet low- p_T^μ 8 TeV	25.4	0.3	0.6	26.4 ± 3.8	873200 ± 2600	873709
0-jet high- p_T^μ 7 TeV	5.5	0.1	0.3	5.9 ± 0.8	982900 ± 2100	982442
0-jet high- p_T^μ 8 TeV	30.6	0.4	3.5	34.6 ± 4.6	3775700 ± 3100	3776365
1-jet low- p_T^μ 7 TeV	2.5	0.4	0.3	3.2 ± 0.4	18680 ± 180	18757
1-jet low- p_T^μ 8 TeV	7.0	1.0	0.6	8.6 ± 1.1	40900 ± 360	40606
1-jet high- p_T^μ 7 TeV	3.7	1.4	1.9	7.0 ± 0.6	233600 ± 1200	234390
1-jet high- p_T^μ 8 TeV	15.1	2.2	4.4	21.7 ± 2.3	646000 ± 2500	646549
2-jet 7 TeV	1.4	0.2	0.7	2.4 ± 0.3	33260 ± 350	33186
2-jet 8 TeV	6.3	3.9	2.6	12.8 ± 1.4	164100 ± 1400	164469
ee						
0-jet low- p_T^e 7 TeV	3.6	–	0.1	3.7 ± 0.5	190900 ± 1000	190890
0-jet low- p_T^e 8 TeV	14.3	0.2	0.3	14.7 ± 2.2	519440 ± 700	519376
0-jet high- p_T^e 7 TeV	4.0	–	0.5	4.5 ± 0.6	819900 ± 1700	820035
0-jet high- p_T^e 8 TeV	22.3	0.3	2.5	25.1 ± 3.4	3225000 ± 2000	3225144
1-jet low- p_T^e 7 TeV	1.5	0.2	0.1	1.8 ± 0.2	10268 ± 97	10300
1-jet low- p_T^e 8 TeV	4.6	0.6	0.3	5.5 ± 0.7	26570 ± 180	26604
1-jet high- p_T^e 7 TeV	2.4	0.4	0.6	3.4 ± 0.4	144900 ± 740	144945
1-jet high- p_T^e 8 TeV	11.7	1.9	3.2	16.9 ± 1.8	560000 ± 1900	560104
2-jet 7 TeV	1.6	0.6	0.4	2.6 ± 0.4	35800 ± 280	35796
2-jet 8 TeV	5.0	2.8	1.6	9.4 ± 1.1	140000 ± 1200	140070

Table 5. Observed and predicted event yields in all event categories of the ee and $\mu\mu$ channels for the full discriminator value D region. The event yields of the predicted background distributions correspond to the result of the global fit. The signal yields, on the other hand, are normalized to the standard model prediction. The different signal processes are labelled as ggH (gluon-gluon fusion), VH (production in association with a W or Z boson), and VBF (vector-boson fusion).

Event category	Signal	Background	Data	$\frac{S}{S+B}$
$\ell\ell + LL'$				
$\mu\mu + \mu\tau_h$ 7 TeV	0.111 ± 0.005	2.4 ± 0.3	2	0.103
$\mu\mu + \mu\tau_h$ 8 TeV	0.427 ± 0.021	10.5 ± 0.6	12	0.092
$ee + \mu\tau_h$ 7 TeV	0.087 ± 0.004	1.5 ± 0.1	2	0.135
$ee + \mu\tau_h$ 8 TeV	0.385 ± 0.018	7.6 ± 0.4	11	0.149
$\mu\mu + e\tau_h$ 7 TeV	0.078 ± 0.004	2.2 ± 0.1	1	0.092
$\mu\mu + e\tau_h$ 8 TeV	0.293 ± 0.014	12.2 ± 0.6	8	0.081
$ee + e\tau_h$ 7 TeV	0.075 ± 0.004	2.2 ± 0.1	4	0.077
$ee + e\tau_h$ 8 TeV	0.279 ± 0.013	10.2 ± 0.5	13	0.063
$\mu\mu + \tau_h\tau_h$ 7 TeV	0.073 ± 0.006	0.8 ± 0.1	0	0.195
$\mu\mu + \tau_h\tau_h$ 8 TeV	0.285 ± 0.022	5.8 ± 0.4	4	0.150
$ee + \tau_h\tau_h$ 7 TeV	0.061 ± 0.004	1.1 ± 0.1	1	0.127
$ee + \tau_h\tau_h$ 8 TeV	0.260 ± 0.020	4.8 ± 0.4	9	0.148
$\mu\mu + e\mu$ 7 TeV	0.051 ± 0.002	1.0 ± 0.1	3	0.100
$\mu\mu + e\mu$ 8 TeV	0.202 ± 0.008	5.1 ± 0.3	9	0.105
$ee + e\mu$ 7 TeV	0.045 ± 0.002	1.0 ± 0.0	1	0.077
$ee + e\mu$ 8 TeV	0.185 ± 0.007	4.0 ± 0.2	4	0.082
$\ell + \tau_h\tau_h$				
$\mu + \tau_h\tau_h$ 7 TeV	0.35 ± 0.03	4.1 ± 0.4	2	0.098
$\mu + \tau_h\tau_h$ 8 TeV	1.57 ± 0.12	35.2 ± 2.1	38	0.054
$e + \tau_h\tau_h$ 7 TeV	0.23 ± 0.02	2.7 ± 0.2	0	0.101
$e + \tau_h\tau_h$ 8 TeV	0.87 ± 0.08	16.5 ± 1.1	15	0.062
$\ell + \ell'\tau_h$				
$\mu + \mu\tau_h$ 7 TeV	0.33 ± 0.02	3.2 ± 0.4	2	0.090
$\mu + \mu\tau_h$ low L_T 8 TeV	0.72 ± 0.03	20.7 ± 2.2	19	0.046
$\mu + \mu\tau_h$ high L_T 8 TeV	0.72 ± 0.02	8.4 ± 1.3	7	0.102
$e + \mu\tau_h/\mu + e\tau_h$ 7 TeV	0.47 ± 0.03	6.2 ± 1.0	6	0.074
$e + \mu\tau_h/\mu + e\tau_h$ low L_T 8 TeV	0.92 ± 0.03	24.6 ± 3.2	30	0.041
$e + \mu\tau_h/\mu + e\tau_h$ high L_T 8 TeV	1.15 ± 0.04	13.9 ± 2.0	11	0.109

Table 6. Observed and predicted event yields in all event categories of the $\ell\ell + LL'$ and $\ell + L\tau_h$ channels for the full $m_{\tau\tau}$ and m_{vis} regions, respectively. The event yields of the predicted background distributions correspond to the result of the global fit. The signal yields, on the other hand, are normalized to the standard model prediction. Only SM Higgs boson production ($m_H = 125$ GeV) in association with a W or Z boson is considered as a signal process. The $\frac{S}{S+B}$ variable denotes the ratio of the signal and the signal-plus-background yields in the central $m_{\tau\tau}$ range containing 68% of the signal events for $m_H = 125$ GeV.

Open Access. This article is distributed under the terms of the Creative Commons Attribution License ([CC-BY 4.0](https://creativecommons.org/licenses/by/4.0/)), which permits any use, distribution and reproduction in any medium, provided the original author(s) and source are credited.

References

- [1] S. Weinberg, *A model of leptons*, *Phys. Rev. Lett.* **19** (1967) 1264 [[INSPIRE](#)].
- [2] A. Salam, *Weak and electromagnetic interactions*, in *Elementary particle physics: relativistic groups and analyticity*, N. Svartholm ed., Almqvist & Wiksell, Stockholm Sweden (1968).
- [3] F. Englert and R. Brout, *Broken symmetry and the mass of gauge vector mesons*, *Phys. Rev. Lett.* **13** (1964) 321 [[INSPIRE](#)].
- [4] P.W. Higgs, *Broken symmetries, massless particles and gauge fields*, *Phys. Lett.* **12** (1964) 132 [[INSPIRE](#)].
- [5] P.W. Higgs, *Broken symmetries and the masses of gauge bosons*, *Phys. Rev. Lett.* **13** (1964) 508 [[INSPIRE](#)].
- [6] G.S. Guralnik, C.R. Hagen and T.W.B. Kibble, *Global conservation laws and massless particles*, *Phys. Rev. Lett.* **13** (1964) 585 [[INSPIRE](#)].
- [7] P.W. Higgs, *Spontaneous symmetry breakdown without massless bosons*, *Phys. Rev.* **145** (1966) 1156 [[INSPIRE](#)].
- [8] T.W.B. Kibble, *Symmetry breaking in non-Abelian gauge theories*, *Phys. Rev.* **155** (1967) 1554 [[INSPIRE](#)].
- [9] ATLAS collaboration, *Observation of a new particle in the search for the standard model Higgs boson with the ATLAS detector at the LHC*, *Phys. Lett. B* **716** (2012) 1 [[arXiv:1207.7214](#)] [[INSPIRE](#)].
- [10] CMS collaboration, *Observation of a new boson at a mass of 125 GeV with the CMS experiment at the LHC*, *Phys. Lett. B* **716** (2012) 30 [[arXiv:1207.7235](#)] [[INSPIRE](#)].
- [11] CMS collaboration, *Observation of a new boson with mass near 125 GeV in pp collisions at $\sqrt{s} = 7$ and 8 TeV*, *JHEP* **06** (2013) 081 [[arXiv:1303.4571](#)] [[INSPIRE](#)].
- [12] CMS collaboration, *Study of the mass and spin-parity of the Higgs boson candidate via its decays to Z boson pairs*, *Phys. Rev. Lett.* **110** (2013) 081803 [[arXiv:1212.6639](#)] [[INSPIRE](#)].
- [13] ATLAS collaboration, *Evidence for the spin-0 nature of the Higgs boson using ATLAS data*, *Phys. Lett. B* **726** (2013) 120 [[arXiv:1307.1432](#)] [[INSPIRE](#)].
- [14] ALEPH collaboration, R. Barate et al., *Observation of an excess in the search for the standard model Higgs boson at ALEPH*, *Phys. Lett. B* **495** (2000) 1 [[hep-ex/0011045](#)] [[INSPIRE](#)].
- [15] DELPHI collaboration, J. Abdallah et al., *Final results from DELPHI on the searches for SM and MSSM neutral Higgs bosons*, *Eur. Phys. J. C* **32** (2004) 145 [[hep-ex/0303013](#)] [[INSPIRE](#)].
- [16] L3 collaboration, P. Achard et al., *Standard model Higgs boson with the L3 experiment at LEP*, *Phys. Lett. B* **517** (2001) 319 [[hep-ex/0107054](#)] [[INSPIRE](#)].
- [17] OPAL collaboration, G. Abbiendi et al., *Search for the standard model Higgs boson in e^+e^- collisions at $\sqrt{s} = 192$ –209 GeV*, *Phys. Lett. B* **499** (2001) 38 [[hep-ex/0101014](#)] [[INSPIRE](#)].

- [18] CDF collaboration, T. Aaltonen et al., *Search for a low mass standard model Higgs boson in the $\tau\tau$ decay channel in $p\bar{p}$ collisions at $\sqrt{s} = 1.96$ TeV*, *Phys. Rev. Lett.* **108** (2012) 181804 [[arXiv:1201.4880](#)] [[INSPIRE](#)].
- [19] D0 collaboration, V.M. Abazov et al., *Search for the standard model Higgs boson in τ lepton pair final states*, *Phys. Lett. B* **714** (2012) 237 [[arXiv:1203.4443](#)] [[INSPIRE](#)].
- [20] ATLAS collaboration, *Search for the standard model Higgs boson in the H to $\tau^+\tau^-$ decay mode in $\sqrt{s} = 7$ TeV pp collisions with ATLAS*, *JHEP* **09** (2012) 070 [[arXiv:1206.5971](#)] [[INSPIRE](#)].
- [21] CMS collaboration, *Search for neutral Higgs bosons decaying to τ pairs in pp collisions at $\sqrt{s} = 7$ TeV*, *Phys. Lett. B* **713** (2012) 68 [[arXiv:1202.4083](#)] [[INSPIRE](#)].
- [22] CMS collaboration, *The CMS experiment at the CERN LHC*, *2008 JINST* **3** S08004 [[INSPIRE](#)].
- [23] K. Rose, *Deterministic annealing for clustering, compression, classification, regression, and related optimization problems*, *IEEE Proc.* **86** (1998) 2210.
- [24] CMS collaboration, *Particle-flow event reconstruction in CMS and performance for jets, taus and MET*, *CMS-PAS-PFT-09-001* (2009).
- [25] CMS collaboration, *Commissioning of the particle-flow reconstruction in minimum-bias and jet events from pp collisions at 7 TeV*, *CMS-PAS-PFT-10-002* (2010).
- [26] CMS collaboration, *Commissioning of the particle-flow event reconstruction with leptons from J/Ψ and W decays at 7 TeV*, *CMS-PAS-PFT-10-003* (2010).
- [27] M. Cacciari, G.P. Salam and G. Soyez, *FastJet user manual*, *Eur. Phys. J. C* **72** (2012) 1896 [[arXiv:1111.6097](#)] [[INSPIRE](#)].
- [28] M. Cacciari and G.P. Salam, *Dispelling the N^3 myth for the k_t jet-finder*, *Phys. Lett. B* **641** (2006) 57 [[hep-ph/0512210](#)] [[INSPIRE](#)].
- [29] CMS collaboration, *Determination of jet energy calibration and transverse momentum resolution in CMS*, *2011 JINST* **6** P11002 [[arXiv:1107.4277](#)] [[INSPIRE](#)].
- [30] CMS collaboration, *Identification of b -quark jets with the CMS experiment*, *2013 JINST* **8** P04013 [[arXiv:1211.4462](#)] [[INSPIRE](#)].
- [31] CMS collaboration, *Pileup jet identification*, *CMS-PAS-JME-13-005* (2013).
- [32] CMS collaboration, *MET performance in 8 TeV data*, *CMS-PAS-JME-12-002* (2012).
- [33] A. Hocker, J. Stelzer, F. Tegenfeldt, H. Voss, K. Voss et al., *TMVA — Toolkit for MultiVariate Data Analysis*, *PoS(ACAT)040* [[physics/0703039](#)] [[INSPIRE](#)].
- [34] CMS collaboration, *Performance of CMS muon reconstruction in pp collision events at $\sqrt{s} = 7$ TeV*, *2012 JINST* **7** P10002 [[arXiv:1206.4071](#)] [[INSPIRE](#)].
- [35] CMS collaboration, *Electron reconstruction and identification at $\sqrt{s} = 7$ TeV*, *CMS-PAS-EGM-10-004* (2010).
- [36] CMS collaboration, *Performance of τ -lepton reconstruction and identification in CMS*, *2012 JINST* **7** P01001 [[arXiv:1109.6034](#)] [[INSPIRE](#)].
- [37] P. Nason, *A new method for combining NLO QCD with shower Monte Carlo algorithms*, *JHEP* **11** (2004) 040 [[hep-ph/0409146](#)] [[INSPIRE](#)].

- [38] S. Frixione, P. Nason and C. Oleari, *Matching NLO QCD computations with parton shower simulations: the POWHEG method*, *JHEP* **11** (2007) 070 [[arXiv:0709.2092](#)] [[INSPIRE](#)].
- [39] S. Alioli, P. Nason, C. Oleari and E. Re, *A general framework for implementing NLO calculations in shower Monte Carlo programs: the POWHEG BOX*, *JHEP* **06** (2010) 043 [[arXiv:1002.2581](#)] [[INSPIRE](#)].
- [40] S. Alioli, K. Hamilton, P. Nason, C. Oleari and E. Re, *Jet pair production in POWHEG*, *JHEP* **04** (2011) 081 [[arXiv:1012.3380](#)] [[INSPIRE](#)].
- [41] S. Alioli, P. Nason, C. Oleari and E. Re, *NLO Higgs boson production via gluon fusion matched with shower in POWHEG*, *JHEP* **04** (2009) 002 [[arXiv:0812.0578](#)] [[INSPIRE](#)].
- [42] T. Sjöstrand, S. Mrenna and P.Z. Skands, *PYTHIA 6.4 physics and manual*, *JHEP* **05** (2006) 026 [[hep-ph/0603175](#)] [[INSPIRE](#)].
- [43] J. Alwall, M. Herquet, F. Maltoni, O. Mattelaer and T. Stelzer, *MadGraph 5: going beyond*, *JHEP* **06** (2011) 128 [[arXiv:1106.0522](#)] [[INSPIRE](#)].
- [44] CMS collaboration, *Measurement of the underlying event activity at the LHC with $\sqrt{s} = 7$ TeV and comparison with $\sqrt{s} = 0.9$ TeV*, *JHEP* **09** (2011) 109 [[arXiv:1107.0330](#)] [[INSPIRE](#)].
- [45] S. Jadach, J.H. Kuhn and Z. Was, *TAUOLA: a library of Monte Carlo programs to simulate decays of polarized τ leptons*, *Comput. Phys. Commun.* **64** (1990) 275 [[INSPIRE](#)].
- [46] D. de Florian, G. Ferrera, M. Grazzini and D. Tommasini, *Higgs boson production at the LHC: transverse momentum resummation effects in the $H \rightarrow 2\gamma$, $H \rightarrow WW \rightarrow l\nu l\nu$ and $H \rightarrow ZZ \rightarrow 4l$ decay modes*, *JHEP* **06** (2012) 132 [[arXiv:1203.6321](#)] [[INSPIRE](#)].
- [47] LHC HIGGS CROSS SECTION WORKING GROUP collaboration, S. Dittmaier et al., *Handbook of LHC Higgs cross sections: 1. Inclusive observables*, [arXiv:1101.0593](#) [[INSPIRE](#)].
- [48] S. Dittmaier et al., *Handbook of LHC Higgs cross sections: 2. Differential distributions*, [arXiv:1201.3084](#) [[INSPIRE](#)].
- [49] LHC HIGGS CROSS SECTION WORKING GROUP collaboration, S. Heinemeyer et al., *Handbook of LHC Higgs cross sections: 3. Higgs properties*, [arXiv:1307.1347](#) [[INSPIRE](#)].
- [50] A. Djouadi, M. Spira and P. Zerwas, *Production of Higgs bosons in proton colliders: QCD corrections*, *Phys. Lett. B* **264** (1991) 440 [[INSPIRE](#)].
- [51] S. Dawson, *Radiative corrections to Higgs boson production*, *Nucl. Phys. B* **359** (1991) 283 [[INSPIRE](#)].
- [52] M. Spira, A. Djouadi, D. Graudenz and P. Zerwas, *Higgs boson production at the LHC*, *Nucl. Phys. B* **453** (1995) 17 [[hep-ph/9504378](#)] [[INSPIRE](#)].
- [53] R.V. Harlander and W.B. Kilgore, *Next-to-next-to-leading order Higgs production at hadron colliders*, *Phys. Rev. Lett.* **88** (2002) 201801 [[hep-ph/0201206](#)] [[INSPIRE](#)].
- [54] C. Anastasiou and K. Melnikov, *Higgs boson production at hadron colliders in NNLO QCD*, *Nucl. Phys. B* **646** (2002) 220 [[hep-ph/0207004](#)] [[INSPIRE](#)].
- [55] V. Ravindran, J. Smith and W.L. van Neerven, *NNLO corrections to the total cross-section for Higgs boson production in hadron hadron collisions*, *Nucl. Phys. B* **665** (2003) 325 [[hep-ph/0302135](#)] [[INSPIRE](#)].
- [56] S. Catani, D. de Florian, M. Grazzini and P. Nason, *Soft gluon resummation for Higgs boson production at hadron colliders*, *JHEP* **07** (2003) 028 [[hep-ph/0306211](#)] [[INSPIRE](#)].

- [57] U. Aglietti, R. Bonciani, G. Degrossi and A. Vicini, *Two loop light fermion contribution to Higgs production and decays*, *Phys. Lett. B* **595** (2004) 432 [[hep-ph/0404071](#)] [[INSPIRE](#)].
- [58] G. Degrossi and F. Maltoni, *Two-loop electroweak corrections to Higgs production at hadron colliders*, *Phys. Lett. B* **600** (2004) 255 [[hep-ph/0407249](#)] [[INSPIRE](#)].
- [59] S. Actis, G. Passarino, C. Sturm and S. Uccirati, *NLO electroweak corrections to Higgs boson production at hadron colliders*, *Phys. Lett. B* **670** (2008) 12 [[arXiv:0809.1301](#)] [[INSPIRE](#)].
- [60] C. Anastasiou, R. Boughezal and F. Petriello, *Mixed QCD-electroweak corrections to Higgs boson production in gluon fusion*, *JHEP* **04** (2009) 003 [[arXiv:0811.3458](#)] [[INSPIRE](#)].
- [61] D. de Florian and M. Grazzini, *Higgs production through gluon fusion: updated cross sections at the Tevatron and the LHC*, *Phys. Lett. B* **674** (2009) 291 [[arXiv:0901.2427](#)] [[INSPIRE](#)].
- [62] J. Baglio and A. Djouadi, *Higgs production at the LHC*, *JHEP* **03** (2011) 055 [[arXiv:1012.0530](#)] [[INSPIRE](#)].
- [63] M. Ciccolini, A. Denner and S. Dittmaier, *Strong and electroweak corrections to the production of Higgs + 2 jets via weak interactions at the LHC*, *Phys. Rev. Lett.* **99** (2007) 161803 [[arXiv:0707.0381](#)] [[INSPIRE](#)].
- [64] M. Ciccolini, A. Denner and S. Dittmaier, *Electroweak and QCD corrections to Higgs production via vector-boson fusion at the LHC*, *Phys. Rev. D* **77** (2008) 013002 [[arXiv:0710.4749](#)] [[INSPIRE](#)].
- [65] K. Arnold et al., *VBFNLO: a parton level Monte Carlo for processes with electroweak bosons*, *Comput. Phys. Commun.* **180** (2009) 1661 [[arXiv:0811.4559](#)] [[INSPIRE](#)].
- [66] O. Brein, A. Djouadi and R. Harlander, *NNLO QCD corrections to the Higgs-strahlung processes at hadron colliders*, *Phys. Lett. B* **579** (2004) 149 [[hep-ph/0307206](#)] [[INSPIRE](#)].
- [67] M. Ciccolini, S. Dittmaier and M. Krämer, *Electroweak radiative corrections to associated WH and ZH production at hadron colliders*, *Phys. Rev. D* **68** (2003) 073003 [[hep-ph/0306234](#)] [[INSPIRE](#)].
- [68] J. Butterworth et al., *The tools and Monte Carlo working group summary report*, [arXiv:1003.1643](#) [[INSPIRE](#)].
- [69] A. Denner, S. Heinemeyer, I. Puljak, D. Rebuszi and M. Spira, *Standard model Higgs-boson branching ratios with uncertainties*, *Eur. Phys. J. C* **71** (2011) 1753 [[arXiv:1107.5909](#)] [[INSPIRE](#)].
- [70] S. Alekhin et al., *The PDF4LHC working group interim report*, [arXiv:1101.0536](#) [[INSPIRE](#)].
- [71] M. Botje et al., *The PDF4LHC working group interim recommendations*, [arXiv:1101.0538](#) [[INSPIRE](#)].
- [72] H.-L. Lai et al., *New parton distributions for collider physics*, *Phys. Rev. D* **82** (2010) 074024 [[arXiv:1007.2241](#)] [[INSPIRE](#)].
- [73] R.D. Ball et al., *Impact of heavy quark masses on parton distributions and LHC phenomenology*, *Nucl. Phys. B* **849** (2011) 296 [[arXiv:1101.1300](#)] [[INSPIRE](#)].
- [74] GEANT4 collaboration, S. Agostinelli et al., *GEANT4 — a simulation toolkit*, *Nucl. Instrum. Meth. A* **506** (2003) 250 [[INSPIRE](#)].
- [75] CMS collaboration, *Measurement of the inclusive Z cross section via decays to τ pairs in pp collisions at $\sqrt{s} = 7$ TeV*, *JHEP* **08** (2011) 117 [[arXiv:1104.1617](#)] [[INSPIRE](#)].

- [76] CMS collaboration, *Missing transverse energy performance of the CMS detector*, 2011 *JINST* **6** P09001 [[arXiv:1106.5048](#)] [[INSPIRE](#)].
- [77] B. Bullock, K. Hagiwara and A.D. Martin, *τ polarization and its correlations as a probe of new physics*, *Nucl. Phys. B* **395** (1993) 499 [[INSPIRE](#)].
- [78] PARTICLE DATA GROUP collaboration, J. Beringer et al., *Review of particle physics*, *Phys. Rev. D* **86** (2012) 010001 [[INSPIRE](#)].
- [79] CMS collaboration, *Measurements of inclusive W and Z cross sections in pp collisions at $\sqrt{s} = 7$ TeV*, *JHEP* **01** (2011) 080 [[arXiv:1012.2466](#)] [[INSPIRE](#)].
- [80] CMS collaboration, *Absolute calibration of the luminosity measurement at CMS: winter 2012 update*, *CMS-PAS-SMP-12-008* (2012).
- [81] CMS collaboration, *CMS luminosity based on pixel cluster counting — Summer 2013 update*, *CMS-PAS-LUM-13-001* (2013).
- [82] K. Hamilton, P. Nason and G. Zanderighi, *MINLO: Multi-scale Improved NLO*, *JHEP* **10** (2012) 155 [[arXiv:1206.3572](#)] [[INSPIRE](#)].
- [83] S. Frixione and B.R. Webber, *Matching NLO QCD computations and parton shower simulations*, *JHEP* **06** (2002) 029 [[hep-ph/0204244](#)] [[INSPIRE](#)].
- [84] CMS collaboration, *Measurement of W^+W^- and ZZ production cross sections in pp collisions at $\sqrt{s} = 8$ TeV*, *Phys. Lett. B* **721** (2013) 190 [[arXiv:1301.4698](#)] [[INSPIRE](#)].
- [85] CMS collaboration, *Measurement of the single-top-quark t -channel cross section in pp collisions at $\sqrt{s} = 7$ TeV*, *JHEP* **12** (2012) 035 [[arXiv:1209.4533](#)] [[INSPIRE](#)].
- [86] CMS collaboration, *Measurement of associated production of vector bosons and top quark-antiquark pairs at $\sqrt{s} = 7$ TeV*, *Phys. Rev. Lett.* **110** (2013) 172002 [[arXiv:1303.3239](#)] [[INSPIRE](#)].
- [87] ATLAS and CMS collaborations, LHC Higgs Combination Group, *Procedure for the LHC Higgs boson search combination in Summer 2011*, *ATL-PHYS-PUB-2011-11* (2011).
- [88] CMS collaboration, *Combined results of searches for the standard model Higgs boson in pp collisions at $\sqrt{s} = 7$ TeV*, *Phys. Lett. B* **710** (2012) 26 [[arXiv:1202.1488](#)] [[INSPIRE](#)].
- [89] J.S. Conway, *Incorporating nuisance parameters in likelihoods for multisource spectra*, in the proceedings of *PHYSTAT 2011 Workshop on Statistical Issues Related to Discovery Claims in Search Experiments and Unfolding*, January 17–20, CERN, Geneva, Switzerland (2011).
- [90] T. Junk, *Confidence level computation for combining searches with small statistics*, *Nucl. Instrum. Meth. A* **434** (1999) 435 [[hep-ex/9902006](#)] [[INSPIRE](#)].
- [91] A.L. Read, *Presentation of search results: the $CL(s)$ technique*, *J. Phys. G* **28** (2002) 2693 [[INSPIRE](#)].

The CMS collaboration

Yerevan Physics Institute, Yerevan, Armenia

S. Chatrchyan, V. Khachatryan, A.M. Sirunyan, A. Tumasyan

Institut für Hochenergiephysik der OeAW, Wien, Austria

W. Adam, T. Bergauer, M. Dragicevic, J. Erö, C. Fabjan¹, M. Friedl, R. Frühwirth¹, V.M. Ghete, C. Hartl, N. Hörmann, J. Hrubec, M. Jeitler¹, W. Kiesenhofer, V. Knünz, M. Krammer¹, I. Krätschmer, D. Liko, I. Mikulec, D. Rabady², B. Rahbaran, H. Rohringer, R. Schöfbeck, J. Strauss, A. Taurok, W. Treberer-Treberspurg, W. Waltenberger, C.-E. Wulz¹

National Centre for Particle and High Energy Physics, Minsk, Belarus

V. Mossolov, N. Shumeiko, J. Suarez Gonzalez

Universiteit Antwerpen, Antwerpen, Belgium

S. Alderweireldt, M. Bansal, S. Bansal, T. Cornelis, E.A. De Wolf, X. Janssen, A. Knutsson, S. Luyckx, S. Ochesanu, B. Roland, R. Rougny, H. Van Haevermaet, P. Van Mechelen, N. Van Remortel, A. Van Spilbeeck

Vrije Universiteit Brussel, Brussel, Belgium

F. Blekman, S. Blyweert, J. D'Hondt, N. Heracleous, A. Kalogeropoulos, J. Keaveney, T.J. Kim, S. Lowette, M. Maes, A. Olbrechts, D. Strom, S. Tavernier, W. Van Doninck, P. Van Mulders, G.P. Van Onsem, I. Villella

Université Libre de Bruxelles, Bruxelles, Belgium

C. Caillol, B. Clerbaux, G. De Lentdecker, L. Favart, A.P.R. Gay, A. Léonard, P.E. Marage, A. Mohammadi, L. Perniè, T. Reis, T. Seva, L. Thomas, C. Vander Velde, P. Vanlaer, J. Wang

Ghent University, Ghent, Belgium

V. Adler, K. Beernaert, L. Benucci, A. Cimmino, S. Costantini, S. Crucy, S. Dildick, G. Garcia, B. Klein, J. Lellouch, J. McCartin, A.A. Ocampo Rios, D. Ryckbosch, S. Salva Diblen, M. Sigamani, N. Strobbe, F. Thyssen, M. Tytgat, S. Walsh, E. Yazgan, N. Zaganidis

Université Catholique de Louvain, Louvain-la-Neuve, Belgium

S. Basegmez, C. Beluffi³, G. Bruno, R. Castello, A. Caudron, L. Ceard, G.G. Da Silveira, C. Delaere, T. du Pree, D. Favart, L. Forthomme, A. Giammanco⁴, J. Hollar, P. Jez, M. Komm, V. Lemaitre, J. Liao, O. Militaru, C. Nuttens, D. Pagano, L. Perrini, A. Pin, K. Piotrkowski, A. Popov⁵, L. Quertenmont, M. Selvaggi, M. Vidal Marono, J.M. Vizan Garcia

Université de Mons, Mons, Belgium

N. Bely, T. Caebergs, E. Daubie, G.H. Hammad

Centro Brasileiro de Pesquisas Fisicas, Rio de Janeiro, Brazil

G.A. Alves, M. Correa Martins Junior, T. Martins, M.E. Pol, M.H.G. Souza

Universidade do Estado do Rio de Janeiro, Rio de Janeiro, Brazil

W.L. Aldá Júnior, W. Carvalho, J. Chinellato⁶, A. Custódio, E.M. Da Costa, D. De Jesus Damiao, C. De Oliveira Martins, S. Fonseca De Souza, H. Malbouisson, M. Malek, D. Matos Figueiredo, L. Mundim, H. Nogima, W.L. Prado Da Silva, J. Santaolalla, A. Santoro, A. Sznajder, E.J. Tonelli Manganote⁶, A. Vilela Pereira

Universidade Estadual Paulista ^a, Universidade Federal do ABC ^b, São Paulo, Brazil

C.A. Bernardes^b, F.A. Dias^{a,7}, T.R. Fernandez Perez Tomei^a, E.M. Gregores^b, P.G. Mercadante^b, S.F. Novaes^a, Sandra S. Padula^a

Institute for Nuclear Research and Nuclear Energy, Sofia, Bulgaria

V. Genchev², P. Iaydjiev², A. Marinov, S. Piperov, M. Rodozov, G. Sultanov, M. Vutova

University of Sofia, Sofia, Bulgaria

A. Dimitrov, I. Glushkov, R. Hadjiiska, V. Kozhuharov, L. Litov, B. Pavlov, P. Petkov

Institute of High Energy Physics, Beijing, China

J.G. Bian, G.M. Chen, H.S. Chen, M. Chen, R. Du, C.H. Jiang, D. Liang, S. Liang, X. Meng, R. Plestina⁸, J. Tao, X. Wang, Z. Wang

State Key Laboratory of Nuclear Physics and Technology, Peking University, Beijing, China

C. Asawatangtrakuldee, Y. Ban, Y. Guo, Q. Li, W. Li, S. Liu, Y. Mao, S.J. Qian, D. Wang, L. Zhang, W. Zou

Universidad de Los Andes, Bogota, Colombia

C. Avila, C.A. Carrillo Montoya, L.F. Chaparro Sierra, C. Florez, J.P. Gomez, B. Gomez Moreno, J.C. Sanabria

Technical University of Split, Split, Croatia

N. Godinovic, D. Lelas, D. Polic, I. Puljak

University of Split, Split, Croatia

Z. Antunovic, M. Kovac

Institute Rudjer Boskovic, Zagreb, Croatia

V. Brigljevic, K. Kadija, J. Luetic, D. Mekterovic, S. Morovic, L. Tikvica

University of Cyprus, Nicosia, Cyprus

A. Attikis, G. Mavromanolakis, J. Mousa, C. Nicolaou, F. Ptochos, P.A. Razis

Charles University, Prague, Czech Republic

M. Finger, M. Finger Jr.

Academy of Scientific Research and Technology of the Arab Republic of Egypt, Egyptian Network of High Energy Physics, Cairo, Egypt

Y. Assran⁹, S. Elgammal¹⁰, A. Ellithi Kamel¹¹, M.A. Mahmoud¹², A. Mahrous¹³, A. Radi^{14,15}

National Institute of Chemical Physics and Biophysics, Tallinn, Estonia

M. Kadastik, M. Müntel, M. Murumaa, M. Raidal, L. Rebane, A. Tiko

Department of Physics, University of Helsinki, Helsinki, Finland

P. Eerola, G. Fedi, M. Voutilainen

Helsinki Institute of Physics, Helsinki, Finland

J. Härkönen, V. Karimäki, R. Kinnunen, M.J. Kortelainen, T. Lampén, K. Lassila-Perini, S. Lehti, T. Lindén, P. Luukka, T. Mäenpää, T. Peltola, E. Tuominen, J. Tuominiemi, E. Tuovinen, L. Wendland

Lappeenranta University of Technology, Lappeenranta, Finland

T. Tuuva

DSM/IRFU, CEA/Saclay, Gif-sur-Yvette, France

M. Besancon, F. Couderc, M. Dejardin, D. Denegri, B. Fabbro, J.L. Faure, F. Ferri, S. Ganjour, A. Givernaud, P. Gras, G. Hamel de Monchenault, P. Jarry, E. Locci, J. Malcles, A. Nayak, J. Rander, A. Rosowsky, M. Titov

Laboratoire Leprince-Ringuet, Ecole Polytechnique, IN2P3-CNRS, Palaiseau, France

S. Baffioni, F. Beaudette, P. Busson, C. Charlot, N. Daci, T. Dahms, M. Dalchenko, L. Dobrzynski, A. Florent, R. Granier de Cassagnac, L. Mastrolorenzo, P. Miné, C. Mironov, I.N. Naranjo, M. Nguyen, C. Ochando, P. Paganini, D. Sabes, R. Salerno, J.b. Sauvan, Y. Sirois, C. Veelken, Y. Yilmaz, A. Zabi

Institut Pluridisciplinaire Hubert Curien, Université de Strasbourg, Université de Haute Alsace Mulhouse, CNRS/IN2P3, Strasbourg, France

J.-L. Agram¹⁶, J. Andrea, D. Bloch, J.-M. Brom, E.C. Chabert, C. Collard, E. Conte¹⁶, F. Drouhin¹⁶, J.-C. Fontaine¹⁶, D. Gelé, U. Goerlach, C. Goetzmann, P. Juillot, A.-C. Le Bihan, P. Van Hove

Centre de Calcul de l'Institut National de Physique Nucleaire et de Physique des Particules, CNRS/IN2P3, Villeurbanne, France

S. Gadrat

Université de Lyon, Université Claude Bernard Lyon 1, CNRS-IN2P3, Institut de Physique Nucléaire de Lyon, Villeurbanne, France

S. Beauceron, N. Beaupere, G. Boudoul, S. Brochet, J. Chasserat, R. Chierici, D. Contardo², P. Depasse, H. El Mamouni, J. Fan, J. Fay, S. Gascon, M. Gouzevitch, B. Ille, T. Kurca, M. Lethuillier, L. Mirabito, S. Perries, J.D. Ruiz Alvarez, L. Sgandurra, V. Sordini, M. Vander Donckt, P. Verdier, S. Viret, H. Xiao

Institute of High Energy Physics and Informatization, Tbilisi State University, Tbilisi, Georgia

Z. Tsamalaidze¹⁷

RWTH Aachen University, I. Physikalisches Institut, Aachen, Germany

C. Autermann, S. Beranek, M. Bontenackels, B. Calpas, M. Edelhoff, L. Feld, O. Hindrichs, K. Klein, A. Ostapchuk, A. Perieanu, F. Raupach, J. Sammet, S. Schael, D. Sprenger, H. Weber, B. Wittmer, V. Zhukov⁵

RWTH Aachen University, III. Physikalisches Institut A, Aachen, Germany

M. Ata, J. Caudron, E. Dietz-Laursonn, D. Duchardt, M. Erdmann, R. Fischer, A. Güth, T. Hebbeker, C. Heidemann, K. Hoepfner, D. Klingebiel, S. Knutzen, P. Kreuzer, M. Merzschmeyer, A. Meyer, M. Olschewski, K. Padeken, P. Papacz, H. Reithler, S.A. Schmitz, L. Sonnenschein, D. Teyssier, S. Thüer, M. Weber

RWTH Aachen University, III. Physikalisches Institut B, Aachen, Germany

V. Cherepanov, Y. Erdogan, G. Flügge, H. Geenen, M. Geisler, W. Haj Ahmad, F. Hoehle, B. Kargoll, T. Kress, Y. Kuessel, J. Lingemann², A. Nowack, I.M. Nugent, L. Perchalla, O. Pooth, A. Stahl

Deutsches Elektronen-Synchrotron, Hamburg, Germany

I. Asin, N. Bartosik, J. Behr, W. Behrenhoff, U. Behrens, A.J. Bell, M. Bergholz¹⁸, A. Bethani, K. Borras, A. Burgmeier, A. Cakir, L. Calligaris, A. Campbell, S. Choudhury, F. Costanza, C. Diez Pardos, S. Dooling, T. Dorland, G. Eckerlin, D. Eckstein, T. Eichhorn, G. Flucke, A. Geiser, A. Grebenyuk, P. Gunnellini, S. Habib, J. Hauk, G. Hellwig, M. Hempel, D. Horton, H. Jung, M. Kasemann, P. Katsas, J. Kieseler, C. Kleinwort, M. Krämer, D. Krücker, W. Lange, J. Leonard, K. Lipka, W. Lohmann¹⁸, B. Lutz, R. Mankel, I. Marfin, I.-A. Melzer-Pellmann, A.B. Meyer, J. Mnich, A. Mussgiller, S. Naumann-Emme, O. Novgorodova, F. Nowak, E. Ntomari, H. Perrey, A. Petrukhin, D. Pitzl, R. Placakyte, A. Raspereza, P.M. Ribeiro Cipriano, C. Riedl, E. Ron, M.Ö. Sahin, J. Salfeld-Nebgen, P. Saxena, R. Schmidt¹⁸, T. Schoerner-Sadenius, M. Schröder, M. Stein, A.D.R. Vargas Trevino, R. Walsh, C. Wissing

University of Hamburg, Hamburg, Germany

M. Aldaya Martin, V. Blobel, H. Enderle, J. Erfle, E. Garutti, K. Goebel, M. Görner, M. Gosselink, J. Haller, R.S. Höing, H. Kirschenmann, R. Klanner, R. Kogler, J. Lange, T. Lapsien, T. Lenz, I. Marchesini, J. Ott, T. Peiffer, N. Pietsch, D. Rathjens, C. Sander, H. Schettler, P. Schleper, E. Schlieckau, A. Schmidt, M. Seidel, J. Sibille¹⁹, V. Sola, H. Stadie, G. Steinbrück, D. Troendle, E. Usai, L. Vanelderen

Institut für Experimentelle Kernphysik, Karlsruhe, Germany

C. Barth, C. Baus, J. Berger, C. Böser, E. Butz, R. Caspart, T. Chwalek, F. Colombo, W. De Boer, A. Descroix, A. Dierlamm, M. Feindt, R. Friese, M. Guthoff², F. Hartmann², T. Hauth², H. Held, K.H. Hoffmann, U. Husemann, I. Katkov⁵, A. Kornmayer², E. Kuznetsova, P. Lobelle Pardo, D. Martschei, M.U. Mozer, T. Müller, Th. Müller, M. Niegel, A. Nürnberg, O. Oberst, G. Quast, K. Rabbertz, F. Ratnikov, S. Röcker, F.-P. Schilling, G. Schott, H.J. Simonis, F.M. Stober, R. Ulrich, J. Wagner-Kuhr, S. Wayand, T. Weiler, R. Wolf, M. Zeise

Institute of Nuclear and Particle Physics (INPP), NCSR Demokritos, Aghia Paraskevi, Greece

G. Anagnostou, G. Daskalakis, T. Geralis, S. Kesisoglou, A. Kyriakis, D. Loukas, A. Markou, C. Markou, A. Psallidas, I. Topsis-giotis

University of Athens, Athens, Greece

L. Gouskos, A. Panagiotou, N. Saoulidou, E. Stiliaris

University of Ioánnina, Ioánnina, Greece

X. Aslanoglou, I. Evangelou², G. Flouris, C. Foudas², J. Jones, P. Kokkas, N. Manthos, I. Papadopoulos, E. Paradas

Wigner Research Centre for Physics, Budapest, Hungary

G. Bencze², C. Hajdu, P. Hidas, D. Horvath²⁰, F. Sikler, V. Veszpremi, G. Vesztergombi²¹, A.J. Zsigmond

Institute of Nuclear Research ATOMKI, Debrecen, Hungary

N. Beni, S. Czellar, J. Molnar, J. Palinkas, Z. Szillasi

University of Debrecen, Debrecen, Hungary

J. Karancsi, P. Raics, Z.L. Trocsanyi, B. Ujvari

National Institute of Science Education and Research, Bhubaneswar, India

S.K. Swain

Panjab University, Chandigarh, India

S.B. Beri, V. Bhatnagar, N. Dhingra, R. Gupta, M. Kaur, M.Z. Mehta, M. Mittal, N. Nishu, A. Sharma, J.B. Singh

University of Delhi, Delhi, India

Ashok Kumar, Arun Kumar, S. Ahuja, A. Bhardwaj, B.C. Choudhary, A. Kumar, S. Malhotra, M. Naimuddin, K. Ranjan, V. Sharma, R.K. Shivpuri

Saha Institute of Nuclear Physics, Kolkata, India

S. Banerjee, S. Bhattacharya, K. Chatterjee, S. Dutta, B. Gomber, Sa. Jain, Sh. Jain, R. Khurana, A. Modak, S. Mukherjee, D. Roy, S. Sarkar, M. Sharan, A.P. Singh

Bhabha Atomic Research Centre, Mumbai, India

A. Abdulsalam, D. Dutta, S. Kailas, V. Kumar, A.K. Mohanty², L.M. Pant, P. Shukla, A. Topkar

Tata Institute of Fundamental Research - EHEP, Mumbai, India

T. Aziz, R.M. Chatterjee, S. Ganguly, S. Ghosh, M. Guchait²², A. Gurtu²³, G. Kole, S. Kumar, M. Maity²⁴, G. Majumder, K. Mazumdar, G.B. Mohanty, B. Parida, K. Sudhakar, N. Wickramage²⁵

Tata Institute of Fundamental Research - HECR, Mumbai, India

S. Banerjee, R.K. Dewanjee, S. Dugad

Institute for Research in Fundamental Sciences (IPM), Tehran, Iran

H. Arfaei, H. Bakhshiansohi, H. Behnamian, S.M. Etesami²⁶, A. Fahim²⁷, A. Jafari, M. Khakzad, M. Mohammadi Najafabadi, M. Naseri, S. Paktinat Mehdiabadi, B. Safarzadeh²⁸, M. Zeinali

University College Dublin, Dublin, Ireland

M. Grunewald

INFN Sezione di Bari ^a, Università di Bari ^b, Politecnico di Bari ^c, Bari, Italy

M. Abbrescia^{a,b}, L. Barbone^{a,b}, C. Calabria^{a,b}, S.S. Chhibra^{a,b}, A. Colaleo^a, D. Creanza^{a,c}, N. De Filippis^{a,c}, M. De Palma^{a,b}, L. Fiore^a, G. Iaselli^{a,c}, G. Maggi^{a,c}, M. Maggi^a, B. Marangelli^{a,b}, S. My^{a,c}, S. Nuzzo^{a,b}, N. Pacifico^a, A. Pompili^{a,b}, G. Pugliese^{a,c}, R. Radogna^{a,b}, G. Selvaggi^{a,b}, L. Silvestris^a, G. Singh^{a,b}, R. Venditti^{a,b}, P. Verwilligen^a, G. Zito^a

INFN Sezione di Bologna ^a, Università di Bologna ^b, Bologna, Italy

G. Abbiendi^a, A.C. Benvenuti^a, D. Bonacorsi^{a,b}, S. Braibant-Giacomelli^{a,b}, L. Brigliadori^{a,b}, R. Campanini^{a,b}, P. Capiluppi^{a,b}, A. Castro^{a,b}, F.R. Cavallo^a, G. Codispoti^{a,b}, M. Cuffiani^{a,b}, G.M. Dallavalle^a, F. Fabbri^a, A. Fanfani^{a,b}, D. Fasanella^{a,b}, P. Giacomelli^a, C. Grandi^a, L. Guiducci^{a,b}, S. Marcellini^a, G. Masetti^a, M. Meneghelli^{a,b}, A. Montanari^a, F.L. Navarria^{a,b}, F. Odorici^a, A. Perrotta^a, F. Primavera^{a,b}, A.M. Rossi^{a,b}, T. Rovelli^{a,b}, G.P. Siroli^{a,b}, N. Tosi^{a,b}, R. Travaglini^{a,b}

INFN Sezione di Catania ^a, Università di Catania ^b, CSFNSM ^c, Catania, Italy

S. Albergo^{a,b}, G. Cappello^a, M. Chiorboli^{a,b}, S. Costa^{a,b}, F. Giordano^{a,2}, R. Potenza^{a,b}, A. Tricomi^{a,b}, C. Tuve^{a,b}

INFN Sezione di Firenze ^a, Università di Firenze ^b, Firenze, Italy

G. Barbagli^a, V. Ciulli^{a,b}, C. Civinini^a, R. D'Alessandro^{a,b}, E. Focardi^{a,b}, E. Gallo^a, S. Gonzi^{a,b}, V. Gori^{a,b}, P. Lenzi^{a,b}, M. Meschini^a, S. Paoletti^a, G. Sguazzoni^a, A. Tropiano^{a,b}

INFN Laboratori Nazionali di Frascati, Frascati, Italy

L. Benussi, S. Bianco, F. Fabbri, D. Piccolo

INFN Sezione di Genova ^a, Università di Genova ^b, Genova, Italy

P. Fabbriatore^a, R. Ferretti^{a,b}, F. Ferro^a, M. Lo Vetere^{a,b}, R. Musenich^a, E. Robutti^a, S. Tosi^{a,b}

INFN Sezione di Milano-Bicocca ^a, Università di Milano-Bicocca ^b, Milano, Italy

M.E. Dinardo^{a,b}, S. Fiorendi^{a,b,2}, S. Gennai^a, R. Gerosa, A. Ghezzi^{a,b}, P. Govoni^{a,b}, M.T. Lucchini^{a,b,2}, S. Malvezzi^a, R.A. Manzoni^{a,b,2}, A. Martelli^{a,b,2}, B. Marzocchi, D. Menasce^a, L. Moroni^a, M. Paganoni^{a,b}, D. Pedrini^a, S. Ragazzi^{a,b}, N. Redaelli^a, T. Tabarelli de Fatis^{a,b}

INFN Sezione di Napoli ^a, Università di Napoli 'Federico II' ^b, Università della Basilicata (Potenza) ^c, Università G. Marconi (Roma) ^d, Napoli, Italy

S. Buontempo^a, N. Cavallo^{a,c}, S. Di Guida^{a,d}, F. Fabozzi^{a,c}, A.O.M. Iorio^{a,b}, L. Lista^a, S. Meola^{a,d,2}, M. Merola^a, P. Paolucci^{a,2}

INFN Sezione di Padova ^a, Università di Padova ^b, Università di Trento (Trento) ^c, Padova, Italy

P. Azzi^a, N. Bacchetta^a, D. Bisello^{a,b}, A. Branca^{a,b}, R. Carlin^{a,b}, P. Checchia^a, T. Dorigo^a, M. Galanti^{a,b,2}, F. Gasparini^{a,b}, U. Gasparini^{a,b}, P. Giubilato^{a,b}, A. Gozzelino^a, K. Kanishchev^{a,c}, S. Lacaprara^a, I. Lazzizzera^{a,c}, M. Margoni^{a,b}, A.T. Meneguzzo^{a,b}, M. Nespolo^a, J. Pazzini^{a,b}, N. Pozzobon^{a,b}, P. Ronchese^{a,b}, F. Simonetto^{a,b}, E. Torassa^a, M. Tosi^{a,b}, A. Triossi^a, S. Vanini^{a,b}, P. Zotto^{a,b}, A. Zucchetta^{a,b}, G. Zumerle^{a,b}

INFN Sezione di Pavia ^a, Università di Pavia ^b, Pavia, Italy

M. Gabusi^{a,b}, S.P. Ratti^{a,b}, C. Riccardi^{a,b}, P. Salvini^a, P. Vitulo^{a,b}

INFN Sezione di Perugia ^a, Università di Perugia ^b, Perugia, Italy

M. Biasini^{a,b}, G.M. Bilei^a, L. Fanò^{a,b}, P. Lariccia^{a,b}, G. Mantovani^{a,b}, M. Menichelli^a, F. Romeo^{a,b}, A. Saha^a, A. Santocchia^{a,b}, A. Spiezia^{a,b}

INFN Sezione di Pisa ^a, Università di Pisa ^b, Scuola Normale Superiore di Pisa ^c, Pisa, Italy

K. Androsov^{a,29}, P. Azzurri^a, G. Bagliesi^a, J. Bernardini^a, T. Boccali^a, G. Broccoli^{a,c}, R. Castaldi^a, M.A. Ciocci^{a,29}, R. Dell'Orso^a, S. Donato^{a,c}, F. Fiori^{a,c}, L. Foà^{a,c}, A. Giassi^a, M.T. Grippo^{a,29}, A. Kraan^a, F. Ligabue^{a,c}, T. Lomtadze^a, L. Martini^{a,b}, A. Messineo^{a,b}, C.S. Moon^{a,30}, F. Palla^{a,2}, A. Rizzi^{a,b}, A. Savoy-Navarro^{a,31}, A.T. Serban^a, P. Spagnolo^a, P. Squillacioti^{a,29}, R. Tenchini^a, G. Tonelli^{a,b}, A. Venturi^a, P.G. Verdini^a, C. Vernieri^{a,c}

INFN Sezione di Roma ^a, Università di Roma ^b, Roma, Italy

L. Barone^{a,b}, F. Cavallari^a, D. Del Re^{a,b}, M. Diemoz^a, M. Grassi^{a,b}, C. Jorda^a, E. Longo^{a,b}, F. Margaroli^{a,b}, P. Meridiani^a, F. Micheli^{a,b}, S. Nourbakhsh^{a,b}, G. Organtini^{a,b}, R. Paramatti^a, S. Rahatlou^{a,b}, C. Rovelli^a, L. Soffi^{a,b}, P. Traczyk^{a,b}

INFN Sezione di Torino ^a, Università di Torino ^b, Università del Piemonte Orientale (Novara) ^c, Torino, Italy

N. Amapane^{a,b}, R. Arcidiacono^{a,c}, S. Argiro^{a,b}, M. Arneodo^{a,c}, R. Bellan^{a,b}, C. Biino^a, N. Cartiglia^a, S. Casasso^{a,b}, M. Costa^{a,b}, A. Degano^{a,b}, N. Demaria^a, C. Mariotti^a, S. Maselli^a, E. Migliore^{a,b}, V. Monaco^{a,b}, M. Musich^a, M.M. Obertino^{a,c}, G. Ortona^{a,b}, L. Pacher^{a,b}, N. Pastrone^a, M. Pelliccioni^{a,2}, A. Potenza^{a,b}, A. Romero^{a,b}, M. Ruspa^{a,c}, R. Sacchi^{a,b}, A. Solano^{a,b}, A. Staiano^a, U. Tamponi^a

INFN Sezione di Trieste ^a, Università di Trieste ^b, Trieste, Italy

S. Belforte^a, V. Candelise^{a,b}, M. Casarsa^a, F. Cossutti^a, G. Della Ricca^{a,b}, B. Gobbo^a, C. La Licata^{a,b}, M. Marone^{a,b}, D. Montanino^{a,b}, A. Penzo^a, A. Schizzi^{a,b}, T. Umer^{a,b}, A. Zanetti^a

Kangwon National University, Chunchon, Korea

S. Chang, T.Y. Kim, S.K. Nam

Kyungpook National University, Daegu, Korea

D.H. Kim, G.N. Kim, J.E. Kim, M.S. Kim, D.J. Kong, S. Lee, Y.D. Oh, H. Park, A. Sakharov, D.C. Son

Chonnam National University, Institute for Universe and Elementary Particles, Kwangju, Korea

J.Y. Kim, Zero J. Kim, S. Song

Korea University, Seoul, Korea

S. Choi, D. Gyun, B. Hong, M. Jo, H. Kim, Y. Kim, B. Lee, K.S. Lee, S.K. Park, Y. Roh

University of Seoul, Seoul, Korea

M. Choi, J.H. Kim, C. Park, I.C. Park, S. Park, G. Ryu

Sungkyunkwan University, Suwon, Korea

Y. Choi, Y.K. Choi, J. Goh, E. Kwon, J. Lee, H. Seo, I. Yu

Vilnius University, Vilnius, Lithuania

A. Juodagalvis

National Centre for Particle Physics, Universiti Malaya, Kuala Lumpur, Malaysia

J.R. Komaragiri

Centro de Investigacion y de Estudios Avanzados del IPN, Mexico City, Mexico

H. Castilla-Valdez, E. De La Cruz-Burelo, I. Heredia-de La Cruz³², R. Lopez-Fernandez, J. Martínez-Ortega, A. Sanchez-Hernandez, L.M. Villasenor-Cendejas

Universidad Iberoamericana, Mexico City, Mexico

S. Carrillo Moreno, F. Vazquez Valencia

Benemerita Universidad Autonoma de Puebla, Puebla, Mexico

H.A. Salazar Ibarguen

Universidad Autónoma de San Luis Potosí, San Luis Potosí, Mexico

E. Casimiro Linares, A. Morelos Pineda

University of Auckland, Auckland, New Zealand

D. Krofcheck

University of Canterbury, Christchurch, New Zealand

P.H. Butler, R. Doesburg, S. Reucroft

National Centre for Physics, Quaid-I-Azam University, Islamabad, Pakistan

A. Ahmad, M. Ahmad, M.I. Asghar, J. Butt, Q. Hassan, H.R. Hoorani, W.A. Khan, T. Khurshid, S. Qazi, M.A. Shah, M. Shoaib

National Centre for Nuclear Research, Swierk, Poland

H. Bialkowska, M. Bluj³³, B. Boimska, T. Frueboes, M. Górski, M. Kazana, K. Nawrocki, K. Romanowska-Rybinska, M. Szleper, G. Wrochna, P. Zalewski

Institute of Experimental Physics, Faculty of Physics, University of Warsaw, Warsaw, Poland

G. Brona, K. Bunkowski, M. Cwiok, W. Dominik, K. Doroba, A. Kalinowski, M. Konecki, J. Krolikowski, M. Misiura, W. Wolszczak

Laboratório de Instrumentação e Física Experimental de Partículas, Lisboa, Portugal

P. Bargassa, C. Beirão Da Cruz E Silva, P. Faccioli, P.G. Ferreira Parracho, M. Gallinaro, F. Nguyen, J. Rodrigues Antunes, J. Seixas, J. Varela, P. Vischia

Joint Institute for Nuclear Research, Dubna, Russia

S. Afanasiev, P. Bunin, I. Golutvin, I. Gorbunov, V. Karjavin, V. Konoplyanikov, G. Kozlov, A. Lanev, A. Malakhov, V. Matveev³⁴, P. Moisenz, V. Palichik, V. Perelygin, M. Savina, S. Shmatov, S. Shulha, V. Smirnov, A. Zarubin

Petersburg Nuclear Physics Institute, Gatchina (St. Petersburg), Russia

V. Golovtsov, Y. Ivanov, V. Kim, P. Levchenko, V. Murzin, V. Oreshkin, I. Smirnov, V. Sulimov, L. Uvarov, S. Vavilov, A. Vorobyev, An. Vorobyev

Institute for Nuclear Research, Moscow, Russia

Yu. Andreev, A. Dermenev, S. Gninenko, N. Golubev, M. Kirsanov, N. Krasnikov, A. Pashenkov, D. Tlisov, A. Toropin

Institute for Theoretical and Experimental Physics, Moscow, Russia

V. Epshteyn, V. Gavrilov, N. Lychkovskaya, V. Popov, G. Safronov, S. Semenov, A. Spiridonov, V. Stolin, E. Vlasov, A. Zhokin

P.N. Lebedev Physical Institute, Moscow, Russia

V. Andreev, M. Azarkin, I. Dremin, M. Kirakosyan, A. Leonidov, G. Mesyats, S.V. Rusakov, A. Vinogradov

Skobeltsyn Institute of Nuclear Physics, Lomonosov Moscow State University, Moscow, Russia

A. Belyaev, E. Boos, V. Bunichev, M. Dubinin⁷, L. Dudko, A. Ershov, A. Gribushin, V. Klyukhin, O. Kodolova, I. Lokhtin, S. Obraztsov, S. Petrushanko, V. Savrin

State Research Center of Russian Federation, Institute for High Energy Physics, Protvino, Russia

I. Azhgirey, I. Bayshev, S. Bitioukov, V. Kachanov, A. Kalinin, D. Konstantinov, V. Krychkine, V. Petrov, R. Ryutin, A. Sobol, L. Tourtchanovitch, S. Troshin, N. Tyurin, A. Uzunian, A. Volkov

University of Belgrade, Faculty of Physics and Vinca Institute of Nuclear Sciences, Belgrade, Serbia

P. Adzic³⁵, M. Djordjevic, M. Ekmedzic, J. Milosevic

Centro de Investigaciones Energéticas Medioambientales y Tecnológicas (CIEMAT), Madrid, Spain

M. Aguilar-Benitez, J. Alcaraz Maestre, C. Battilana, E. Calvo, M. Cerrada, M. Chamizo Llatas², N. Colino, B. De La Cruz, A. Delgado Peris, D. Domínguez Vázquez, C. Fernandez Bedoya, J.P. Fernández Ramos, A. Ferrando, J. Flix, M.C. Fouz, P. Garcia-Abia, O. Gonzalez Lopez, S. Goy Lopez, J.M. Hernandez, M.I. Josa, G. Merino, E. Navarro De Martino, A. Pérez-Calero Yzquierdo, J. Puerta Pelayo, A. Quintario Olmeda, I. Redondo, L. Romero, M.S. Soares, C. Willmott

Universidad Autónoma de Madrid, Madrid, Spain

C. Albajar, J.F. de Trocóniz, M. Missiroli

Universidad de Oviedo, Oviedo, Spain

H. Brun, J. Cuevas, J. Fernandez Menendez, S. Folgueras, I. Gonzalez Caballero, L. Lloret Iglesias

Instituto de Física de Cantabria (IFCA), CSIC-Universidad de Cantabria, Santander, Spain

J.A. Brochero Cifuentes, I.J. Cabrillo, A. Calderon, J. Duarte Campderros, M. Fernandez, G. Gomez, J. Gonzalez Sanchez, A. Graziano, A. Lopez Virto, J. Marco, R. Marco, C. Martinez Rivero, F. Matorras, F.J. Munoz Sanchez, J. Piedra Gomez, T. Rodrigo, A.Y. Rodríguez-Marrero, A. Ruiz-Jimeno, L. Scodellaro, I. Vila, R. Vilar Cortabitarte

CERN, European Organization for Nuclear Research, Geneva, Switzerland

D. Abbaneo, E. Auffray, G. Auzinger, M. Bachtis, P. Baillon, A.H. Ball, D. Barney, A. Benaglia, J. Bendavid, L. Benhabib, J.F. Benitez, C. Bernet⁸, G. Bianchi, P. Bloch, A. Bocci, A. Bonato, O. Bondu, C. Botta, H. Breuker, T. Camporesi, G. Cerminara, T. Christiansen, J.A. Coarasa Perez, S. Colafranceschi³⁶, M. D'Alfonso, D. d'Enterria, A. Dabrowski, A. David, F. De Guio, A. De Roeck, S. De Visscher, M. Dobson, N. Dupont-Sagorin, A. Elliott-Peisert, J. Eugster, G. Franzoni, W. Funk, M. Giffels, D. Gigi, K. Gill, M. Girone, M. Giunta, F. Glege, R. Gomez-Reino Garrido, S. Gowdy, R. Guida, J. Hammer, M. Hansen, P. Harris, V. Innocente, P. Janot, E. Karavakis, K. Kousouris, K. Krajczar, P. Lecoq, C. Lourenço, N. Magini, L. Malgeri, M. Mannelli, L. Masetti, F. Meijers, S. Mersi, E. Meschi, F. Moortgat, M. Mulders, P. Musella, L. Orsini, E. Palencia Cortezon, L. Pape, E. Perez, L. Perrozzi, A. Petrilli, G. Petrucciani, A. Pfeiffer, M. Pierini, M. Pimiä, D. Piparo, M. Plagge, A. Racz, W. Reece, G. Rolandi³⁷, M. Rovere, H. Sakulin, F. Santanastasio, C. Schäfer, C. Schwick, S. Sekmen, A. Sharma, P. Siegrist, P. Silva, M. Simon, P. Sphicas³⁸, J. Steggemann, B. Stieger, M. Stoye, D. Treille, A. Tsirou, G.I. Veres²¹, J.R. Vlimant, H.K. Wöhri, W.D. Zeuner

Paul Scherrer Institut, Villigen, Switzerland

W. Bertl, K. Deiters, W. Erdmann, R. Horisberger, Q. Ingram, H.C. Kaestli, S. König, D. Kotlinski, U. Langenegger, D. Renker, T. Rohe

Institute for Particle Physics, ETH Zurich, Zurich, Switzerland

F. Bachmair, L. Bäni, L. Bianchini, P. Bortignon, M.A. Buchmann, B. Casal, N. Chanon, A. Deisher, G. Dissertori, M. Dittmar, M. Donegà, M. Dünser, P. Eller, C. Grab, D. Hits, W. Lustermann, B. Mangano, A.C. Marini, P. Martinez Ruiz del Arbol, D. Meister, N. Mohr, C. Nägeli³⁹, P. Nef, F. Nessi-Tedaldi, F. Pandolfi, F. Pauss, M. Peruzzi, M. Quittnat, F.J. Ronga, M. Rossini, A. Starodumov⁴⁰, M. Takahashi, L. Tauscher[†], K. Theofilatos, R. Wallny, H.A. Weber

Universität Zürich, Zurich, Switzerland

C. Amsler⁴¹, M.F. Canelli, V. Chiochia, A. De Cosa, C. Favaro, A. Hinzmann, T. Hreus, M. Ivova Rikova, B. Kilminster, B. Millan Mejias, J. Ngadiuba, P. Robmann, H. Snoek, S. Taroni, M. Verzetti, Y. Yang

National Central University, Chung-Li, Taiwan

M. Cardaci, K.H. Chen, C. Ferro, C.M. Kuo, S.W. Li, W. Lin, Y.J. Lu, R. Volpe, S.S. Yu

National Taiwan University (NTU), Taipei, Taiwan

P. Bartalini, P. Chang, Y.H. Chang, Y.W. Chang, Y. Chao, K.F. Chen, P.H. Chen, C. Dietz, U. Grundler, W.-S. Hou, Y. Hsiung, K.Y. Kao, Y.J. Lei, Y.F. Liu, R.-S. Lu, D. Majumder, E. Petrakou, X. Shi, J.G. Shiu, Y.M. Tzeng, M. Wang, R. Wilken

Chulalongkorn University, Bangkok, Thailand

B. Asavapibhop, N. Suwonjandee

Cukurova University, Adana, Turkey

A. Adiguzel, M.N. Bakirci⁴², S. Cerci⁴³, C. Dozen, I. Dumanoglu, E. Eskut, S. Girgis, G. Gokbulut, E. Gurpinar, I. Hos, E.E. Kangal, A. Kayis Topaksu, G. Onengut⁴⁴, K. Ozdemir, S. Ozturk⁴², A. Polatoz, K. Sogut⁴⁵, D. Sunar Cerci⁴³, B. Tali⁴³, H. Topakli⁴², M. Vergili

Middle East Technical University, Physics Department, Ankara, Turkey

I.V. Akin, T. Aliev, B. Bilin, S. Bilmis, M. Deniz, H. Gamsizkan, A.M. Guler, G. Karapinar⁴⁶, K. Ocalan, A. Ozpineci, M. Serin, R. Sever, U.E. Surat, M. Yalvac, M. Zeyrek

Bogazici University, Istanbul, Turkey

E. Gülmez, B. Isildak⁴⁷, M. Kaya⁴⁸, O. Kaya⁴⁸, S. Ozkorucuklu⁴⁹

Istanbul Technical University, Istanbul, Turkey

H. Bahtiyar⁵⁰, E. Barlas, K. Cankocak, Y.O. Günaydin⁵¹, F.I. Vardarli, M. Yücel

National Scientific Center, Kharkov Institute of Physics and Technology, Kharkov, Ukraine

L. Levchuk, P. Sorokin

University of Bristol, Bristol, United Kingdom

J.J. Brooke, E. Clement, D. Cussans, H. Flacher, R. Frazier, J. Goldstein, M. Grimes, G.P. Heath, H.F. Heath, J. Jacob, L. Kreczko, C. Lucas, Z. Meng, D.M. Newbold⁵², S. Paramesvaran, A. Poll, S. Senkin, V.J. Smith, T. Williams

Rutherford Appleton Laboratory, Didcot, United Kingdom

K.W. Bell, A. Belyaev⁵³, C. Brew, R.M. Brown, D.J.A. Cockerill, J.A. Coughlan, K. Harder, S. Harper, J. Ilic, E. Olaiya, D. Petyt, C.H. Shepherd-Themistocleous, A. Thea, I.R. Tomalin, W.J. Womersley, S.D. Worm

Imperial College, London, United Kingdom

M. Baber, R. Bainbridge, O. Buchmuller, D. Burton, D. Colling, N. Cripps, M. Cutajar, P. Dauncey, G. Davies, M. Della Negra, W. Ferguson, J. Fulcher, D. Futyan, A. Gilbert, A. Guneratne Bryer, G. Hall, Z. Hatherell, J. Hays, G. Iles, M. Jarvis, G. Karapostoli, M. Kenzie, R. Lane, R. Lucas⁵², L. Lyons, A.-M. Magnan, J. Marrouche, B. Mathias, R. Nandi, J. Nash, A. Nikitenko⁴⁰, J. Pela, M. Pesaresi, K. Petridis, M. Pioppi⁵⁴, D.M. Raymond, S. Rogerson, A. Rose, C. Seez, P. Sharp[†], A. Sparrow, A. Tapper, M. Vazquez Acosta, T. Virdee, S. Wakefield, N. Wardle

Brunel University, Uxbridge, United Kingdom

J.E. Cole, P.R. Hobson, A. Khan, P. Kyberd, D. Leggat, D. Leslie, W. Martin, I.D. Reid, P. Symonds, L. Teodorescu, M. Turner

Baylor University, Waco, USA

J. Dittmann, K. Hatakeyama, A. Kasmi, H. Liu, T. Scarborough

The University of Alabama, Tuscaloosa, USA

O. Charaf, S.I. Cooper, C. Henderson, P. Rumerio

Boston University, Boston, USA

A. Avetisyan, T. Bose, C. Fantasia, A. Heister, P. Lawson, D. Lazic, C. Richardson, J. Rohlf, D. Sperka, J. St. John, L. Sulak

Brown University, Providence, USA

J. Alimena, S. Bhattacharya, G. Christopher, D. Cutts, Z. Demiragli, A. Ferapontov, A. Garabedian, U. Heintz, S. Jabeen, G. Kukartsev, E. Laird, G. Landsberg, M. Luk, M. Narain, M. Segala, T. Sinthuprasith, T. Speer, J. Swanson

University of California, Davis, Davis, USA

R. Breedon, G. Breto, M. Calderon De La Barca Sanchez, S. Chauhan, M. Chertok, J. Conway, R. Conway, P.T. Cox, R. Erbacher, M. Gardner, W. Ko, A. Kopecky, R. Lander, T. Miceli, M. Mulhearn, D. Pellett, J. Pilot, F. Ricci-Tam, B. Rutherford, M. Searle, S. Shalhout, J. Smith, M. Squires, M. Tripathi, S. Wilbur, R. Yohay

University of California, Los Angeles, USA

V. Andreev, D. Cline, R. Cousins, S. Erhan, P. Everaerts, C. Farrell, M. Felcini, J. Hauser, M. Ignatenko, C. Jarvis, G. Rakness, P. Schlein[†], E. Takasugi, V. Valuev, M. Weber

University of California, Riverside, Riverside, USA

J. Babb, R. Clare, J. Ellison, J.W. Gary, G. Hanson, J. Heilman, P. Jandir, F. Lacroix, H. Liu, O.R. Long, A. Luthra, M. Malberti, H. Nguyen, A. Shrinivas, J. Sturdy, S. Sumowidagdo, S. Wimpenny

University of California, San Diego, La Jolla, USA

W. Andrews, J.G. Branson, G.B. Cerati, S. Cittolin, R.T. D’Agnolo, D. Evans, A. Holzner, R. Kelley, D. Kovalskyi, M. Lebourgeois, J. Letts, I. Macneill, S. Padhi, C. Palmer, M. Pieri, M. Sani, V. Sharma, S. Simon, E. Sudano, M. Tadel, Y. Tu, A. Vartak, S. Wasserbaech⁵⁵, F. Würthwein, A. Yagil, J. Yoo

University of California, Santa Barbara, Santa Barbara, USA

D. Barge, J. Bradmiller-Feld, C. Campagnari, T. Danielson, A. Dishaw, K. Flowers, M. Franco Sevilla, P. Geffert, C. George, F. Golf, J. Incandela, C. Justus, R. Magaña Villalba, N. Mccoll, V. Pavlunin, J. Richman, R. Rossin, D. Stuart, W. To, C. West

California Institute of Technology, Pasadena, USA

A. Apresyan, A. Bornheim, J. Bunn, Y. Chen, E. Di Marco, J. Duarte, D. Kcira, A. Mott, H.B. Newman, C. Pena, C. Rogan, M. Spiropulu, V. Timciuc, R. Wilkinson, S. Xie, R.Y. Zhu

Carnegie Mellon University, Pittsburgh, USA

V. Azzolini, A. Calamba, R. Carroll, T. Ferguson, Y. Iiyama, D.W. Jang, M. Paulini, J. Russ, H. Vogel, I. Vorobiev

University of Colorado at Boulder, Boulder, USA

J.P. Cumalat, B.R. Drell, W.T. Ford, A. Gaz, E. Luiggi Lopez, U. Nauenberg, J.G. Smith, K. Stenson, K.A. Ulmer, S.R. Wagner

Cornell University, Ithaca, USA

J. Alexander, A. Chatterjee, J. Chu, N. Eggert, L.K. Gibbons, W. Hopkins, A. Khukhunaishvili, B. Kreis, N. Mirman, G. Nicolas Kaufman, J.R. Patterson, A. Ryd, E. Salvati, W. Sun, W.D. Teo, J. Thom, J. Thompson, J. Tucker, Y. Weng, L. Winstrom, P. Wittich

Fairfield University, Fairfield, USA

D. Winn

Fermi National Accelerator Laboratory, Batavia, USA

S. Abdullin, M. Albrow, J. Anderson, G. Apollinari, L.A.T. Bauerdick, A. Beretvas, J. Berryhill, P.C. Bhat, K. Burkett, J.N. Butler, V. Chetluru, H.W.K. Cheung, F. Chlebana, S. Cihangir, V.D. Elvira, I. Fisk, J. Freeman, Y. Gao, E. Gottschalk, L. Gray, D. Green, S. Grünendahl, O. Gutsche, D. Hare, R.M. Harris, J. Hirschauer, B. Hooberman, S. Jindariani, M. Johnson, U. Joshi, K. Kaadze, B. Klima, S. Kwan, J. Linacre, D. Lincoln, R. Lipton, J. Lykken, K. Maeshima, J.M. Marraffino, V.I. Martinez Outschoorn, S. Maruyama, D. Mason, P. McBride, K. Mishra, S. Mrenna, Y. Musienko³⁴, S. Nahn, C. Newman-Holmes, V. O’Dell, O. Prokofyev, N. Ratnikova, E. Sexton-Kennedy, S. Sharma, W.J. Spalding, L. Spiegel, L. Taylor, S. Tkaczyk, N.V. Tran, L. Uplegger, E.W. Vaandering, R. Vidal, A. Whitbeck, J. Whitmore, W. Wu, F. Yang, J.C. Yun

University of Florida, Gainesville, USA

D. Acosta, P. Avery, D. Bourilkov, T. Cheng, S. Das, M. De Gruttola, G.P. Di Giovanni, D. Dobur, R.D. Field, M. Fisher, Y. Fu, I.K. Furic, J. Hugon, B. Kim, J. Konigsberg,

A. Korytov, A. Kropivnitskaya, T. Kypreos, J.F. Low, K. Matchev, P. Milenovic⁵⁶, G. Mitselmakher, L. Muniz, A. Rinkevicius, L. Shchutska, N. Skhirtladze, M. Snowball, J. Yelton, M. Zakaria

Florida International University, Miami, USA

V. Gaultney, S. Hewamanage, S. Linn, P. Markowitz, G. Martinez, J.L. Rodriguez

Florida State University, Tallahassee, USA

T. Adams, A. Askew, J. Bochenek, J. Chen, B. Diamond, J. Haas, S. Hagopian, V. Hagopian, K.F. Johnson, H. Prosper, V. Veeraraghavan, M. Weinberg

Florida Institute of Technology, Melbourne, USA

M.M. Baarmand, B. Dorney, M. Hohlmann, H. Kalakhety, F. Yumiceva

University of Illinois at Chicago (UIC), Chicago, USA

M.R. Adams, L. Apanasevich, V.E. Bazterra, R.R. Betts, I. Bucinskaite, R. Cavanaugh, O. Evdokimov, L. Gauthier, C.E. Gerber, D.J. Hofman, S. Khalatyan, P. Kurt, D.H. Moon, C. O'Brien, C. Silkworth, P. Turner, N. Varelas

The University of Iowa, Iowa City, USA

U. Akgun, E.A. Albayrak⁵⁰, B. Bilki⁵⁷, W. Clarida, K. Dilsiz, F. Duru, M. Haytmyradov, J.-P. Merlo, H. Mermerkaya⁵⁸, A. Mestvirishvili, A. Moeller, J. Nachtman, H. Ogul, Y. Onel, F. Ozok⁵⁰, R. Rahmat, S. Sen, P. Tan, E. Tiras, J. Wetzel, T. Yetkin⁵⁹, K. Yi

Johns Hopkins University, Baltimore, USA

B.A. Barnett, B. Blumenfeld, S. Bolognesi, D. Fehling, A.V. Gritsan, P. Maksimovic, C. Martin, M. Swartz

The University of Kansas, Lawrence, USA

P. Baringer, A. Bean, G. Benelli, R.P. Kenny III, M. Murray, D. Noonan, S. Sanders, J. Sekaric, R. Stringer, Q. Wang, J.S. Wood

Kansas State University, Manhattan, USA

A.F. Barfuss, I. Chakaberia, A. Ivanov, S. Khalil, M. Makouski, Y. Maravin, L.K. Saini, S. Shrestha, I. Svintradze

Lawrence Livermore National Laboratory, Livermore, USA

J. Gronberg, D. Lange, F. Rebassoo, D. Wright

University of Maryland, College Park, USA

A. Baden, B. Calvert, S.C. Eno, J.A. Gomez, N.J. Hadley, R.G. Kellogg, T. Kolberg, Y. Lu, M. Marionneau, A.C. Mignerey, K. Pedro, A. Skuja, J. Temple, M.B. Tonjes, S.C. Tonwar

Massachusetts Institute of Technology, Cambridge, USA

A. Apyan, R. Barbieri, G. Bauer, W. Busza, I.A. Cali, M. Chan, L. Di Matteo, V. Dutta, G. Gomez Ceballos, M. Goncharov, D. Gulhan, M. Klute, Y.S. Lai, Y.-J. Lee, A. Levin, P.D. Luckey, T. Ma, C. Paus, D. Ralph, C. Roland, G. Roland, G.S.F. Stephans, F. Stöckli, K. Sumorok, D. Velicanu, J. Veverka, B. Wyslouch, M. Yang, A.S. Yoon, M. Zanetti, V. Zhukova

University of Minnesota, Minneapolis, USA

B. Dahmes, A. De Benedetti, A. Gude, S.C. Kao, K. Klapoetke, Y. Kubota, J. Mans, N. Pastika, R. Rusack, A. Singovsky, N. Tambe, J. Turkewitz

University of Mississippi, Oxford, USA

J.G. Acosta, L.M. Cremaldi, R. Kroeger, S. Oliveros, L. Perera, D.A. Sanders, D. Summers

University of Nebraska-Lincoln, Lincoln, USA

E. Avdeeva, K. Bloom, S. Bose, D.R. Claes, A. Dominguez, R. Gonzalez Suarez, J. Keller, D. Knowlton, I. Kravchenko, J. Lazo-Flores, S. Malik, F. Meier, G.R. Snow

State University of New York at Buffalo, Buffalo, USA

J. Dolen, A. Godshalk, I. Iashvili, S. Jain, A. Kharchilava, A. Kumar, S. Rappoccio

Northeastern University, Boston, USA

G. Alverson, E. Barberis, D. Baumgartel, M. Chasco, J. Haley, A. Massironi, D. Nash, T. Orimoto, D. Trocino, D. Wood, J. Zhang

Northwestern University, Evanston, USA

A. Anastassov, K.A. Hahn, A. Kubik, L. Lusito, N. Mucia, N. Odell, B. Pollack, A. Pozdnyakov, M. Schmitt, S. Stoynev, K. Sung, M. Velasco, S. Won

University of Notre Dame, Notre Dame, USA

D. Berry, A. Brinkerhoff, K.M. Chan, A. Drozdetskiy, M. Hildreth, C. Jessop, D.J. Karmgard, N. Kellams, J. Kolb, K. Lannon, W. Luo, S. Lynch, N. Marinelli, D.M. Morse, T. Pearson, M. Planer, R. Ruchti, J. Slaunwhite, N. Valls, M. Wayne, M. Wolf, A. Woodard

The Ohio State University, Columbus, USA

L. Antonelli, B. Bylsma, L.S. Durkin, S. Flowers, C. Hill, R. Hughes, K. Kotov, T.Y. Ling, D. Puigh, M. Rodenburg, G. Smith, C. Vuosalo, B.L. Winer, H. Wolfe, H.W. Wulsin

Princeton University, Princeton, USA

E. Berry, P. Elmer, V. Halyo, P. Hebda, J. Hegeman, A. Hunt, P. Jindal, S.A. Koay, P. Lujan, D. Marlow, T. Medvedeva, M. Mooney, J. Olsen, P. Piroué, X. Quan, A. Raval, H. Saka, D. Stickland, C. Tully, J.S. Werner, S.C. Zenz, A. Zuranski

University of Puerto Rico, Mayaguez, USA

E. Brownson, A. Lopez, H. Mendez, J.E. Ramirez Vargas

Purdue University, West Lafayette, USA

E. Alagoz, D. Benedetti, G. Bolla, D. Bortoletto, M. De Mattia, A. Everett, Z. Hu, M.K. Jha, M. Jones, K. Jung, M. Kress, N. Leonardo, D. Lopes Pegna, V. Maroussov, P. Merkel, D.H. Miller, N. Neumeister, B.C. Radburn-Smith, I. Shipsey, D. Silvers, A. Svyatkovskiy, F. Wang, W. Xie, L. Xu, H.D. Yoo, J. Zablocki, Y. Zheng

Purdue University Calumet, Hammond, USA

N. Parashar

Rice University, Houston, USA

A. Adair, B. Akgun, K.M. Ecklund, F.J.M. Geurts, W. Li, B. Michlin, B.P. Padley, R. Redjimi, J. Roberts, J. Zabel

University of Rochester, Rochester, USA

B. Betchart, A. Bodek, R. Covarelli, P. de Barbaro, R. Demina, Y. Eshaq, T. Ferbel, A. Garcia-Bellido, P. Goldenzweig, J. Han, A. Harel, D.C. Miner, G. Petrillo, D. Vishnevskiy, M. Zielinski

The Rockefeller University, New York, USA

A. Bhatti, R. Ciesielski, L. Demortier, K. Goulios, G. Lungu, S. Malik, C. Mesropian

Rutgers, The State University of New Jersey, Piscataway, USA

S. Arora, A. Barker, J.P. Chou, C. Contreras-Campana, E. Contreras-Campana, D. Duggan, D. Ferencek, Y. Gershtein, R. Gray, E. Halkiadakis, D. Hidas, A. Lath, S. Panwalkar, M. Park, R. Patel, V. Rekovic, J. Robles, S. Salur, S. Schnetzer, C. Seitz, S. Somalwar, R. Stone, S. Thomas, P. Thomassen, M. Walker

University of Tennessee, Knoxville, USA

K. Rose, S. Spanier, Z.C. Yang, A. York

Texas A&M University, College Station, USA

O. Bouhali⁶⁰, R. Eusebi, W. Flanagan, J. Gilmore, T. Kamon⁶¹, V. Khotilovich, V. Krutelyov, R. Montalvo, I. Osipenkov, Y. Pakhotin, A. Perloff, J. Roe, A. Safonov, T. Sakuma, I. Suarez, A. Tatarinov, D. Toback

Texas Tech University, Lubbock, USA

N. Akchurin, C. Cowden, J. Damgov, C. Dragoiu, P.R. Duder, J. Faulkner, K. Kovitangoon, S. Kunori, S.W. Lee, T. Libeiro, I. Volobouev

Vanderbilt University, Nashville, USA

E. Appelt, A.G. Delannoy, S. Greene, A. Gurrola, W. Johns, C. Maguire, Y. Mao, A. Melo, M. Sharma, P. Sheldon, B. Snook, S. Tuo, J. Velkovska

University of Virginia, Charlottesville, USA

M.W. Arenton, S. Boutle, B. Cox, B. Francis, J. Goodell, R. Hirosky, A. Ledovskoy, C. Lin, C. Neu, J. Wood

Wayne State University, Detroit, USA

S. Gollapinni, R. Harr, P.E. Karchin, C. Kottachchi Kankanamge Don, P. Lamichhane

University of Wisconsin, Madison, USA

D.A. Belknap, L. Borrello, D. Carlsmith, M. Cepeda, S. Cooperstein, S. Dasu, S. Duric, E. Friis, M. Grothe, R. Hall-Wilton, M. Herndon, A. Hervé, P. Klabbbers, J. Klukas, A. Lanaro, A. Levine, R. Loveless, A. Mohapatra, I. Ojalvo, T. Perry, G.A. Pierro, G. Polese, I. Ross, T. Sarangi, A. Savin, W.H. Smith, N. Woods

- †: Deceased
- 1: Also at Vienna University of Technology, Vienna, Austria
 - 2: Also at CERN, European Organization for Nuclear Research, Geneva, Switzerland
 - 3: Also at Institut Pluridisciplinaire Hubert Curien, Université de Strasbourg, Université de Haute Alsace Mulhouse, CNRS/IN2P3, Strasbourg, France
 - 4: Also at National Institute of Chemical Physics and Biophysics, Tallinn, Estonia
 - 5: Also at Skobeltsyn Institute of Nuclear Physics, Lomonosov Moscow State University, Moscow, Russia
 - 6: Also at Universidade Estadual de Campinas, Campinas, Brazil
 - 7: Also at California Institute of Technology, Pasadena, USA
 - 8: Also at Laboratoire Leprince-Ringuet, Ecole Polytechnique, IN2P3-CNRS, Palaiseau, France
 - 9: Also at Suez Canal University, Suez, Egypt
 - 10: Also at Zewail City of Science and Technology, Zewail, Egypt
 - 11: Also at Cairo University, Cairo, Egypt
 - 12: Also at Fayoum University, El-Fayoum, Egypt
 - 13: Also at Helwan University, Cairo, Egypt
 - 14: Also at British University in Egypt, Cairo, Egypt
 - 15: Now at Ain Shams University, Cairo, Egypt
 - 16: Also at Université de Haute Alsace, Mulhouse, France
 - 17: Also at Joint Institute for Nuclear Research, Dubna, Russia
 - 18: Also at Brandenburg University of Technology, Cottbus, Germany
 - 19: Also at The University of Kansas, Lawrence, USA
 - 20: Also at Institute of Nuclear Research ATOMKI, Debrecen, Hungary
 - 21: Also at Eötvös Loránd University, Budapest, Hungary
 - 22: Also at Tata Institute of Fundamental Research - HECR, Mumbai, India
 - 23: Now at King Abdulaziz University, Jeddah, Saudi Arabia
 - 24: Also at University of Visva-Bharati, Santiniketan, India
 - 25: Also at University of Ruhuna, Matara, Sri Lanka
 - 26: Also at Isfahan University of Technology, Isfahan, Iran
 - 27: Also at Sharif University of Technology, Tehran, Iran
 - 28: Also at Plasma Physics Research Center, Science and Research Branch, Islamic Azad University, Tehran, Iran
 - 29: Also at Università degli Studi di Siena, Siena, Italy
 - 30: Also at Centre National de la Recherche Scientifique (CNRS) - IN2P3, Paris, France
 - 31: Also at Purdue University, West Lafayette, USA
 - 32: Also at Universidad Michoacana de San Nicolas de Hidalgo, Morelia, Mexico
 - 33: Also at National Centre for Nuclear Research, Swierk, Poland
 - 34: Also at Institute for Nuclear Research, Moscow, Russia
 - 35: Also at Faculty of Physics, University of Belgrade, Belgrade, Serbia
 - 36: Also at Facoltà Ingegneria, Università di Roma, Roma, Italy
 - 37: Also at Scuola Normale e Sezione dell'INFN, Pisa, Italy
 - 38: Also at University of Athens, Athens, Greece
 - 39: Also at Paul Scherrer Institut, Villigen, Switzerland
 - 40: Also at Institute for Theoretical and Experimental Physics, Moscow, Russia
 - 41: Also at Albert Einstein Center for Fundamental Physics, Bern, Switzerland
 - 42: Also at Gaziosmanpasa University, Tokat, Turkey
 - 43: Also at Adiyaman University, Adiyaman, Turkey
 - 44: Also at Cag University, Mersin, Turkey

- 45: Also at Mersin University, Mersin, Turkey
- 46: Also at Izmir Institute of Technology, Izmir, Turkey
- 47: Also at Ozyegin University, Istanbul, Turkey
- 48: Also at Kafkas University, Kars, Turkey
- 49: Also at Istanbul University, Faculty of Science, Istanbul, Turkey
- 50: Also at Mimar Sinan University, Istanbul, Istanbul, Turkey
- 51: Also at Kahramanmaras Sütcü Imam University, Kahramanmaras, Turkey
- 52: Also at Rutherford Appleton Laboratory, Didcot, United Kingdom
- 53: Also at School of Physics and Astronomy, University of Southampton, Southampton, United Kingdom
- 54: Also at INFN Sezione di Perugia; Università di Perugia, Perugia, Italy
- 55: Also at Utah Valley University, Orem, USA
- 56: Also at University of Belgrade, Faculty of Physics and Vinca Institute of Nuclear Sciences, Belgrade, Serbia
- 57: Also at Argonne National Laboratory, Argonne, USA
- 58: Also at Erzincan University, Erzincan, Turkey
- 59: Also at Yildiz Technical University, Istanbul, Turkey
- 60: Also at Texas A&M University at Qatar, Doha, Qatar
- 61: Also at Kyungpook National University, Daegu, Korea